12-2010

Analysis and Comparison of Effects of an Airfoil or a Rod on Supersonic Cavity Flow.

William Leland Fowler
University of Tennessee Space Institute, wfowler@utsi.edu

To the Graduate Council:

I am submitting herewith a thesis written by William Leland Fowler entitled "Analysis and Comparison of Effects of an Airfoil or a Rod on Supersonic Cavity Flow.." I have examined the final electronic copy of this thesis for form and content and recommend that it be accepted in partial fulfillment of the requirements for the degree of Master of Science, with a major in Aerospace Engineering.

Ahmad D. Vakili, Major Professor

We have read this thesis and recommend its acceptance:

U. Peter Solies, Basil N. Antar

Accepted for the Council:
Carolyn R. Hodges

Vice Provost and Dean of the Graduate School

(Original signatures are on file with official student records.)

To the Graduate Council:

I am submitting herewith a thesis written by William Leland Fowler entitled "Analysis and Comparison of Effects of an Airfoil or a Rod on Supersonic Cavity Flow." I have examined the final electronic copy of this thesis for form and content and recommend that it be accepted in partial fulfillment of the requirements for the degree of Master of Science with a major in Aerospace Engineering.

Ahmad Vakili, Major Professor

We have read this thesis
and recommend its acceptance:

Basil Antar

U. Peter Solies

Accepted for the Council:

Carolyn R. Hodges
Vice Provost and Dean of the Graduate School

(Original signatures are on file with official student records.)

ANALYSIS AND COMPARISON OF EFFECTS OF AN AIRFOIL OR A ROD ON SUPERSONIC CAVITY FLOW

A THESIS
PRESENTED FOR THE
MASTER OF SCIENCE
DEGREE
THE UNIVERSITY OF TENNESSEE, KNOXVILLE

WILLIAM LELAND FOWLER
DECEMBER 2010

Acknowledgements

I wish to thank the many authors for whom I have referenced within this study. It was through their wealth of previous research that provided me the background and motivation required for my own pursuit of cavity flow research.

I thank my advisor, Dr. Ahmad Vakili for his guidance and understanding. Dr. Vakili through his vast experience within the subject of cavity flow helped me to appreciate and understand the research milestones of previous cavity flow literature. I must also thank him for all of the assistance he provided me with the selection of the experimental setup and with the interpretation of the results.

I thank Dr Basil Antar and Dr U. Peter Solies for taking time out of their busy schedules to be a part of my thesis committee. I also appreciate the guidance and advice they provided for improving my thesis.

Thanks are given to the personnel of the UTSI Research Labs led by Mr. Joel Davenport for the fabrication and operation of my test setup. I must emphasize particular appreciation to Mr. Keith Walker for the countless hours he allocated to configuration changes and for the patience and assistance he provided me for the operation of the particle image velocimetry system.

I wish to thank my friends for the assistance and company they provided me during my time in Tennessee. Greg Givogue and Erin Douglas provided a considerable amount of help with the formatting of this document.

I thank my parents Bill and Yvette Fowler and my sister Janet Fowler for all the encouragement they provided me throughout this endeavour. I also appreciate that you have visited me during my time in Tennessee especially since I have seldom visited home within the last two years.

Abstract

The effects of an airfoil at different angles of attack and a circular cylindrical rod within the edge of the boundary layer flow at the leading edge of a cavity as a device for controlling the large pressure fluctuations (resonance tones) in the cavity were investigated. The airfoil results were compared with the rod in crossflow method positioned at the same leading edge location. The cavity used for testing corresponded to a length to depth ratio, L/D of 11.0/2.25 with a length to width ratio, L/W of 11.0/3.00 at a freestream Mach 1.84 flow. The study included measurements of dynamic pressure transducer output at 40 kHz and Frequency Spectra calculations, using Schlieren techniques for shock wave structures with velocity and vorticity fields obtained from PIV measurements. All airfoil configurations experienced flow separation to varying degrees. The negative 10 degree angle of attack configuration experienced the greatest amount of flow separation. All airfoil configurations provided varying degrees of cavity (resonant) tone suppression. Of the airfoil configurations, the negative 10 degree airfoil provided the best noise suppression with a 5 dB SPL reduction in broadband noise and a 9 dB reduction in peak amplitude for the 3rd resonant mode. Although all the airfoil configurations provided various levels of noise suppression, none of the configurations performed to the level of the rod in crossflow technique which provided an 8 dB SPL reduction in broadband noise and a 22 dB reduction in peak amplitude for the 2nd resonant mode. Indications of shear flow lofting effects could not be studied within any of the configurations tested. Lofting effect testing would have required flow field visualization of the cavity trailing edge region. Dynamic pressure measurements at a location near the cavity trailing edge did not detect the rod vortex shedding frequency, clearly. Because PIV results showed strong indication of vortex shedding, the lack of vortex shedding frequency data was attributed to the dynamic pressure transducer being located a far distance of 44 rod diameters downstream of the rod location. All airfoil test configurations showed evidence of deflections to the cavity leading edge oblique shock wave. The mechanisms of the deflection were the airfoil trailing edge shocks interacting with the cavity leading edge shock.

Table of Contents

List of Figures

Page

List of Tables

Page

Nomenclature

D = Cavity depth

K_v = Ratio of convective velocity of vortices to freestream velocity

L = Cavity length

L / D = Cavity length to depth ratio

M = Mach number

PIV = Particle Image Velocimetry

Re = Reynolds number

S = Strouhal number

SPL = Sound Pressure Level

U = Velocity, x-component

V = Velocity, y-component

W = Cavity width

W / D = Cavity width to depth ratio

c = Speed of sound

f = Frequency

m = Mode number for cavity oscillations

n = Phase delay between acoustic wave and new vortex

p = Pressure

δ = Boundary layer thickness

γ = Ratio of specific heats of constant pressure to constant volume

θ = Momentum thickness

θ / L = Shear layer momentum thickness to length ratio

ω = Vorticity

Subscripts

$_{\infty}$ = Freestream

$_{c}$ = Convective

$_{o}$ = Stagnation

$_{L}$ = Length

Chapter 1

INTRODUCTION

Background

Flow passing across confined openings or cavities of otherwise continuous bodies occurs in numerous engineering applications and is typically referred to as cavity flow. Examples of aerodynamic vehicle applications of cavity flow include landing gear compartments and weapons bays. Under various conditions, cavity flow may include large pressure fluctuations, undesirable flow patterns and conditions of increased drag. The concept of cavity flow control includes the application of various techniques to alter a cavity's flow field and thus reduce the harmful or undesirable effects of cavity flow.

Previous research completed for lower speed and incompressible cavity flows has typically been applied to landing gear compartment applications. High speed and compressible cavity flow research has been and continues to be of great importance for aircraft weapons bays for the safe suspension and release of stores. If cavity flow cannot be controlled in weapons bay applications, aircraft safety of flight may easily be jeopardized with the potential to even have stores impacting the aircraft from which they are being released. Due to the significant cavity flow challenges encountered with internal weapons bays applications, cavity flow has often been avoided by using external wing or fuselage mounted suspension and release mechanisms. However, the use of external store suspension and release systems come at the cost of substantial increases in aircraft frontal area which then increase aircraft drag and radar signatures. Cavity flow control in the compressible flow regime has thus gained importance in recent years for the purposes of enabling modern aircraft to safely employ internal weapons bays and maintain aircraft stealth characteristics.

Although aircraft weapons bays may have varying degrees of geometric complexities, previous cavity flow control research has successfully been completed with generalized rectangular cavities. The understanding gained by rectangular cavity models and the associated methods of

cavity flow control have then been applied to more complex weapons bay geometries. Previous examples of this success include the use of weapons bay leading edge devices such as the perforated spoiler of the Lockheed F-117 “Nighthawk” or the saw tooth spoiler of the General Dynamics F-111 "Aardvark".

The flow over a rectangular cavity and its associated geometric nomenclature is depicted within Figure 1. Cavity flow may be categorized by three general classifications which include: open, closed and transitional cavity flows. It should be noted that transitional cavity flows refer to cavity flows which include phenomena of both open and closed cavity flows (as opposed to transition between laminar and turbulent flows). As shown by Chen [1] for subsonic and transonic flow conditions, a convenient factor for the classification of an open, closed or transitional cavity flow is length to depth ratio, L/D. Although length to depth ratio is used as a key parameter for cavity flow classification, Tam & Block [2] noted that the shear layer momentum thickness to length ratio, θ/L plays a significant factor for the classification of cavity flow in addition to L/D.

Plentovich, Stalling & Tracy [3] include a description of open, closed and transitional cavity flow conditions for a supersonic freestream which includes:

1. Open cavity flow: An open cavity flow with a supersonic freestream is depicted in Figure 2. Open flow generally occurs in cavities with values of L/D less than or equal to 10. The flow essentially bridges the cavity and a shear layer is formed over the cavity which does not attach to the bottom of the cavity. In open cavity flow, a cavity resonance can be sustained from the reinforcement between instabilities in the shear layer and upstream-traveling pressure waves generated at the aft wall by the time-varying impingement of the shear layer.

2. Closed cavity flow: A closed cavity flow with a supersonic freestream is depicted in Figure 3. Closed flow occurs for cavities with values of L/D greater than or equal to 13. The flow separates at the forward face of the cavity, reattaches at

some point along the cavity floor, and separates again before reaching the rear cavity face. This flow produces a mean static-pressure distribution with low pressure in the forward region, a plateau in the attached region, and high pressure in the aft region. Impingement and exit shocks are observed. Acoustic tones generally do not occur for closed cavity flow at supersonic speeds.

3. Transitional cavity flow: Transitional-open and transitional-closed cavity flows are depicted within Figure 4. Transitional cavity flows typically occur with values of L / D between approximately 10 and 13.
Transitional cavity flow includes variations between having a transitional open cavity flow where there are a series of compression wavelets on the cavity floor to having a transitional closed cavity flow where there is an impingement shock at the cavity floor.

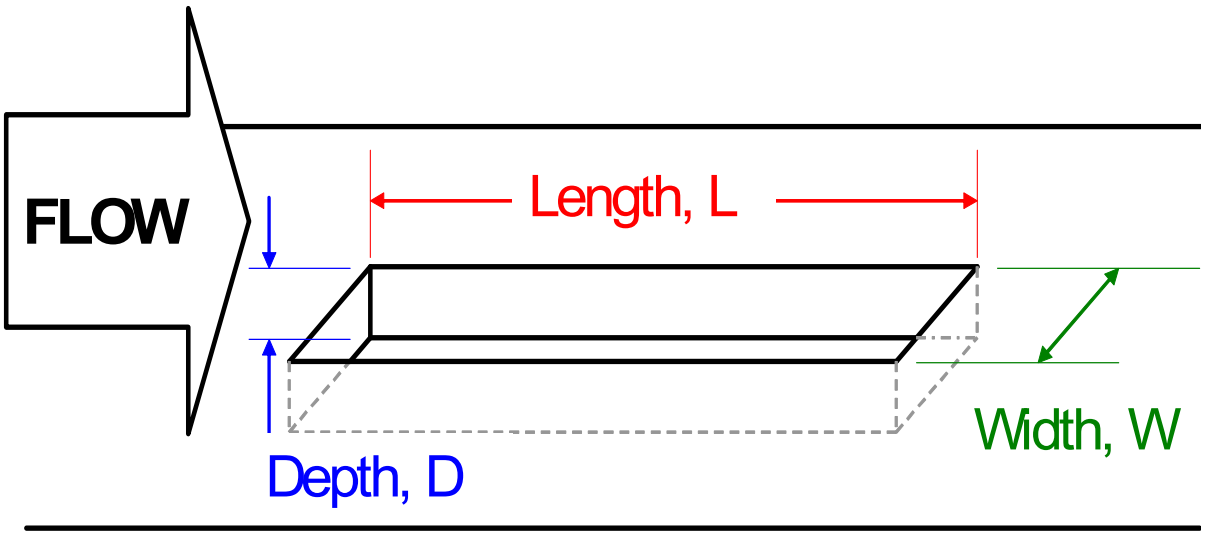

Figure 1. A Typical Rectangular Cavity with a Freestream Crossflow

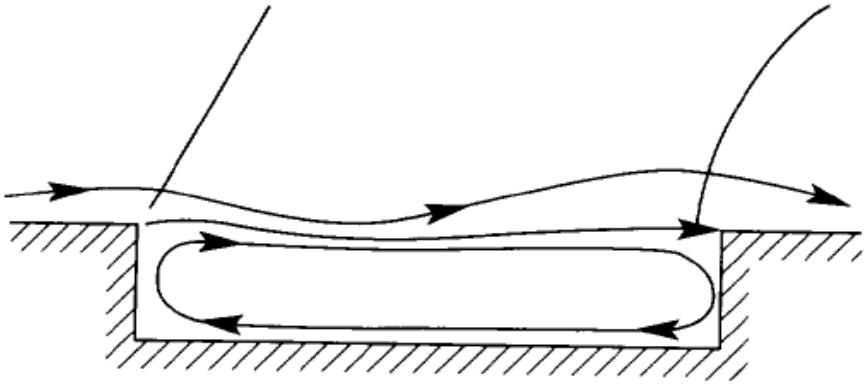

Figure 2. Open Cavity Flow (from Plentovich, Stalling & Tracy [3])

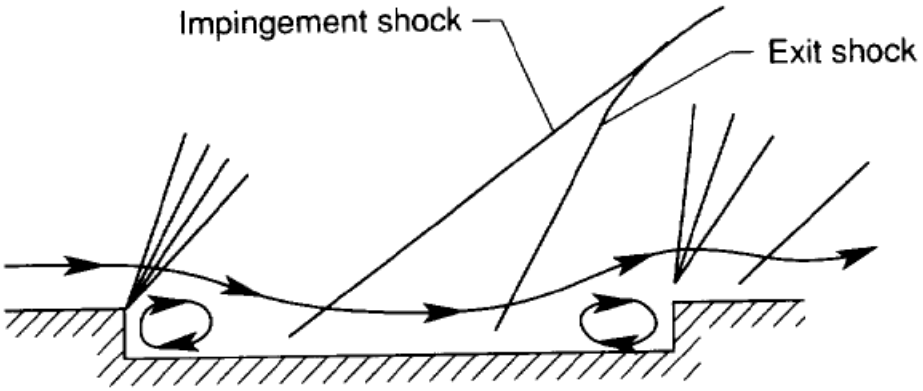

Figure 3. Closed Cavity Flow (from Plentovich, Stalling & Tracy [3])

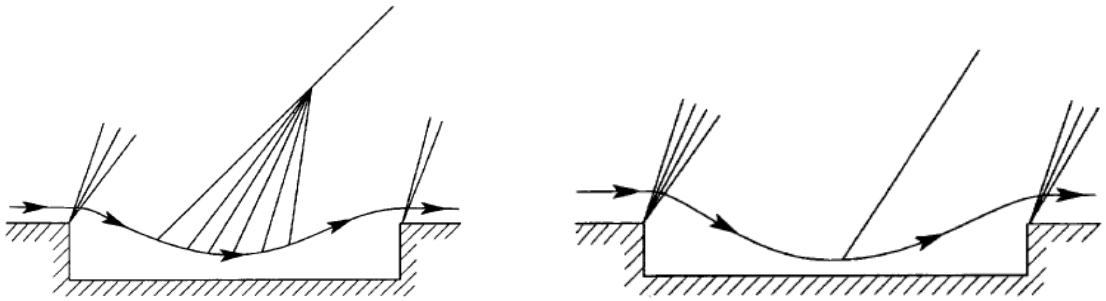

Figure 4. Transitional Cavity Flow – Open (left) and Closed (right) (from Plentovich, Stalling & Tracy [3])

For aircraft weapons bay applications, it is open cavity flow which tends to be the most common. This thesis thus focuses on open cavity flows where the shear layer spans the cavity and the shear layer instability characteristics lead to resonant tone frequencies occurring within the cavity.

Cavity flow control for the purpose of altering a cavity's flow field and thus reducing the undesirable cavity flow effects may be categorized by either "active" or "passive" flow control. Cattafesta III, Williams, Rowley and Farrukh [4] describe active flow control to include techniques which either add or remove energy to a flow while passive flow control techniques do not. Examples of active flow control could include the application of oscillating devices or pulsed upstream mass injection techniques. A simple schematic of an upstream mass injection technique is depicted in Figure 5. Early examples of passive flow control included the use of a flow blockage placed at the leading edge of a cavity such as a sawtooth spoiler or perforated spoiler as depicted in Figure 6. A more recent method of cavity flow control includes the rod in crossflow technique which is illustrated within Figure 7. A possible passive flow control technique could include using an airfoil positioned above the cavity leading edge as depicted within Figure 8. This thesis includes a comparison of passive cavity flow control techniques between using an airfoil in crossflow with a rod in a crossflow.

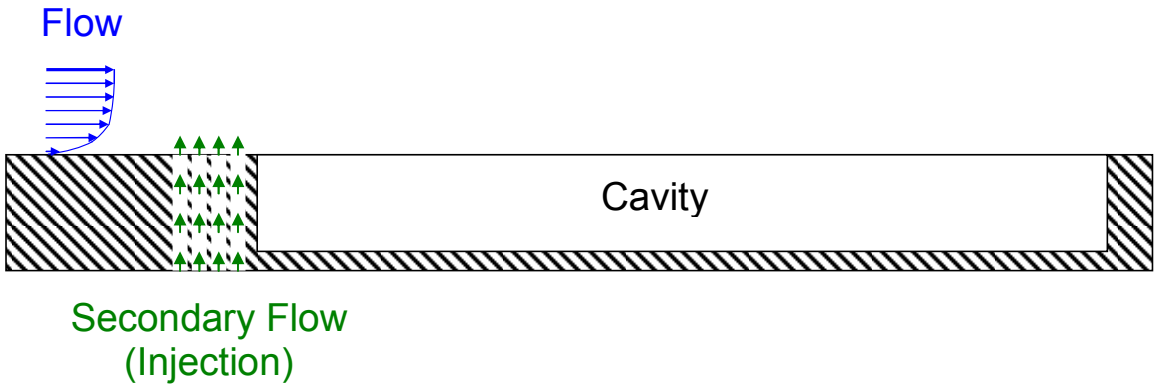

Figure 5. Upstream Mass Injection Schematic (Active Cavity Flow Control Technique)

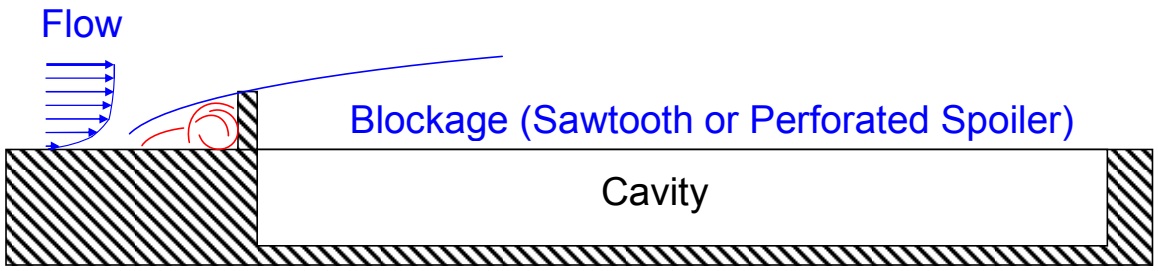

Figure 6. Blockage with Sawtooth or Perforated Spoiler Schematic (Passive Cavity Flow Control Technique)

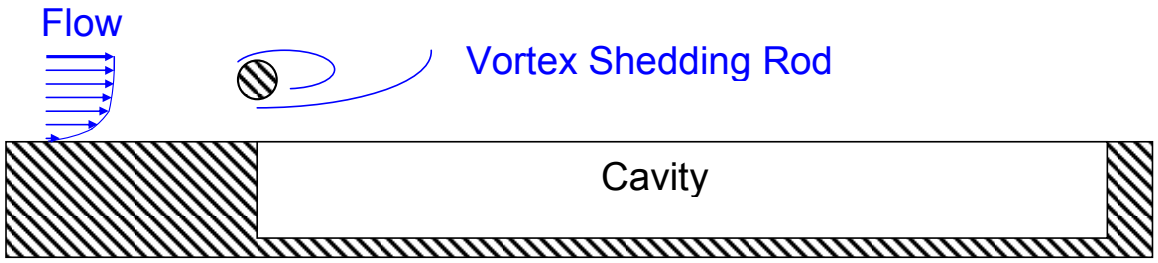

Figure 7. Rod in Crossflow Schematic (Passive Cavity Flow Control Technique)

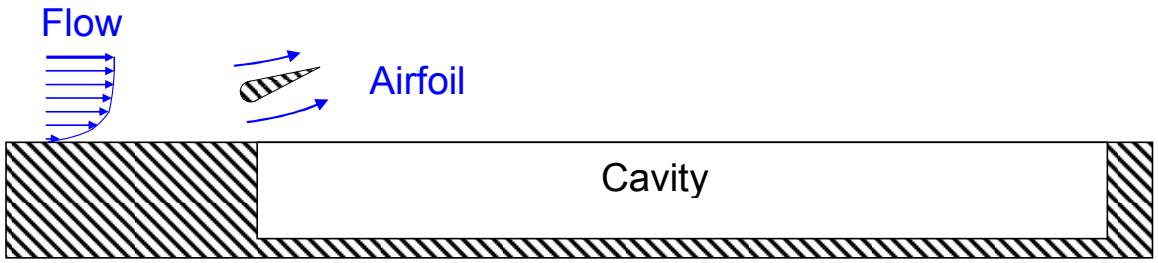

Figure 8. Airfoil in Crossflow Schematic (Possible Passive Cavity Flow Control Technique)

Objective

This study includes open cavity flow research with the use of passive control techniques following in the tradition of previous research by Loewen [5]. Loewen's cavity flow research was completed within the subsonic regime and included the rod in crossflow technique as depicted within Figure 6 and with testing of various rod diameters. The current study included cavity flow research within the supersonic regime with an airfoil in a crossflow as depicted within Figure 7 and with testing at various airfoil angles of attack. The airfoil in a crossflow test data was then compared with the rod in a crossflow technique at the same supersonic flow freestream conditions. The objectives of this thesis thus include:

1. To measure and compare the level of acoustic suppression on a supersonic cavity flow offered by devices placed above the leading edge of a cavity. This objective includes comparing a baseline open cavity acoustic levels with the suppression provided by an airfoil at three different angles of attack compared with the suppression provided by a rod. This objective applies the use of dynamic pressure transducer data with spectrum analysis techniques.

2. To examine the influence on a supersonic cavity flow field structure offered by devices placed above the leading edge of a cavity. This objective includes comparing a baseline open cavity flow field with the cavity flow field resulting from an airfoil at three different angles of attack with that of the cavity flow field resulting from a rod. This objective applies the use of Schlieren photography and Particle Image Velocimetry (PIV).

General Approach

The University of Tennessee Space Institute (UTSI) High Speed Wind Tunnel (HSWT) was used to complete four phases of testing that were identified as requirements for the supersonic cavity flow study. In conjunction with the HSWT, the four phases of testing were initially completed with the TSI LASERPULSE Particle Image Velocimetry (PIV) system for the purposes of determining velocity and vorticity fields. The four phases of testing were then repeated with

Schlieren photography for the purposes of viewing shock structures associated with the cavity flow and the leading edge devices. All phases of testing included a dynamic pressure transducer installed near the rear of the cavity floor or the rear of the solid floor plate for the test phases without a cavity present. The dynamic pressure data collected during each test were used to calculate spectrum data in the frequency domain (Hz) which included sound pressure levels in a decibel scale (dB SPL). A description of the UTSI HSWT design and setup with other test equipment is included within Chapter 3.

The HSWT is a blow-down system and is configured with a converging/diverging nozzle designed for a test section operating Mach number of 1.85 (which in practice typically operates at 1.84). The test section consists of an 8 inch by 8 inch square duct approximately 4 ft long. The HSWT test section includes a solid floor plate which may be removed to configure a cavity within. The cavity used was 11.00" in length, L by 2.25" in depth, D and 3.00" in width, W which is depicted in Figure 9.

The cavity used for testing corresponded to a length to depth ratio, L/D of 4.88. A L/D of 4.88 fits within criteria for resonance-prone open flow which generally occurs in cavities with values of L/D less than or equal to 10. A L/D of 4.88 or slightly larger may also be considered operationally representative to possible future aircraft with relatively deep weapons bays for the inclusion of various large and small geometry stores along with their associated suspension and release mechanisms.

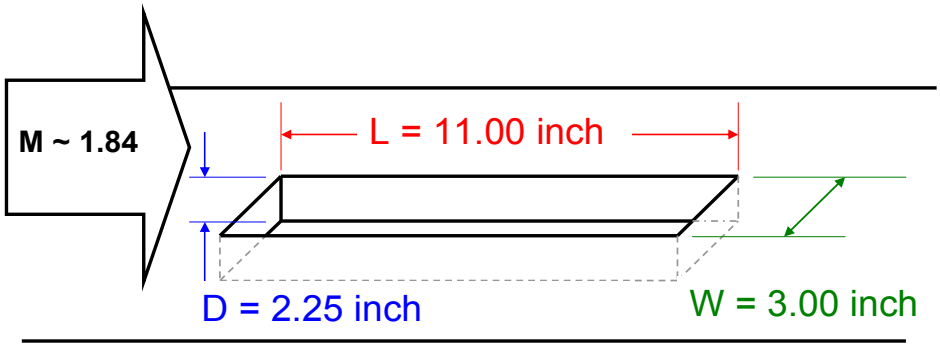

Figure 9. Schematic of Cavity Used for Testing at Supersonic Conditions

With the cavity and flow conditions established, the following test configurations were deemed essential:

1. Clean Tunnel: This configuration depicted within Figure 10 was tested to determine the broadband noise and to acquire an initial assessment of the tunnel flow field characteristics. This test configuration was also for boundary layer measurements of the tunnel floor.

2. Rod Signature and Airfoil Signatures at 0, -5, -10 Angles of Attack with the Solid Floor Plate: These configurations are depicted within Figures 11 and 12. The leading edge devices were positioned above the leading edge of the solid floor plate and within the vicinity of the tunnel floor boundary layer. This phase was required to see the flow field structures resulting from only the leading edge devices and without any cavity present.

3. Baseline Cavity: This configuration included the cavity only without any leading edge flow control devices as shown in Figure 13. This test was required to determine the peak resonance frequencies and the broadband noise created by the cavity. This configuration was required to gain imagery related to the cavity's flow field structure. It also provided the opportunity for existing cavity flow theory to be compared with actual empirical data.

4. Rod with Cavity and Airfoil at 0, -5, -10 Angles of Attack with Cavity: These configurations depicted within Figures 14 and 15 represent a cavity with flow control being applied. The flow control devices were positioned above the leading edge of the cavity and within the vicinity of the tunnel floor boundary layer. These configurations were required to determine the amount of acoustic suppression being provided by each leading edge device. They were also for the purposes of acquiring the flow field structure of the cavity as a result of the leading edge devices.

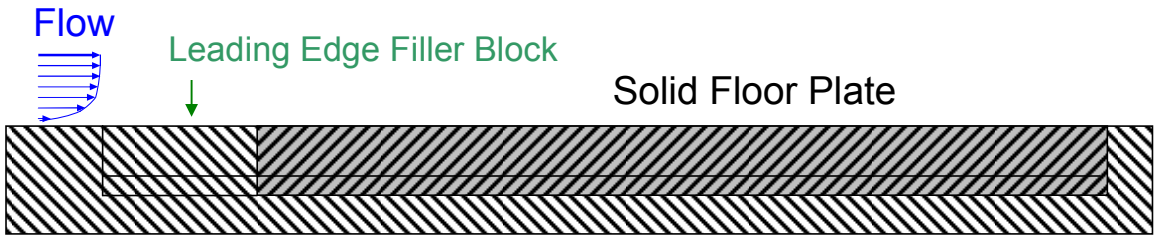

Figure 10. Test Configuration 1: Clean Tunnel - Side View Sketch

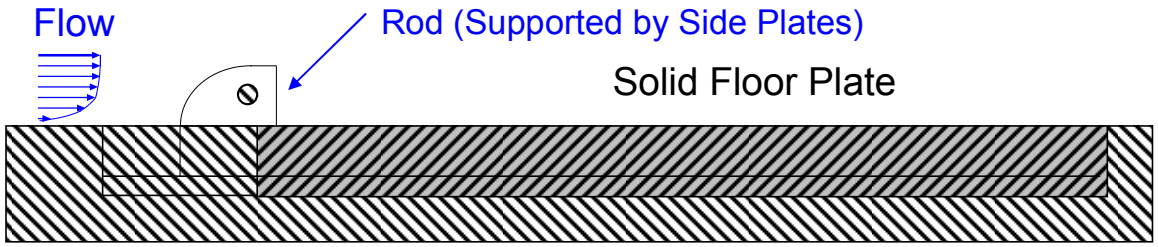

Figure 11. Test Configuration 2a: Rod Signature (Solid Floor Plate) - Side View Sketch

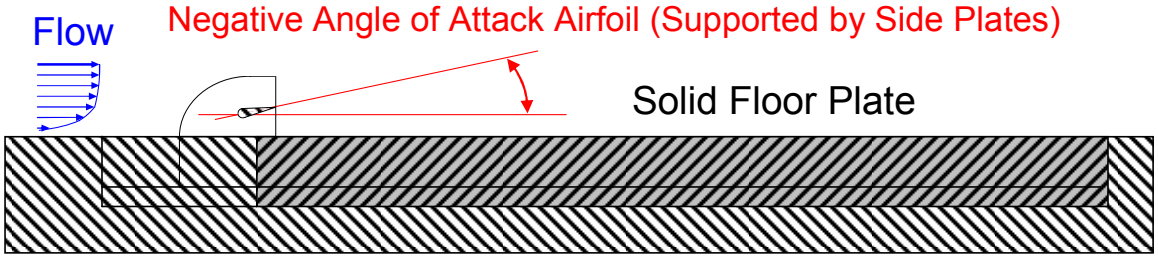

Figure 12. Test Configurations 2b, 2c and 2d: Airfoil Signatures at 0, -5, -10 Angles of Attack (Solid Floor Plate) - Side View Sketch

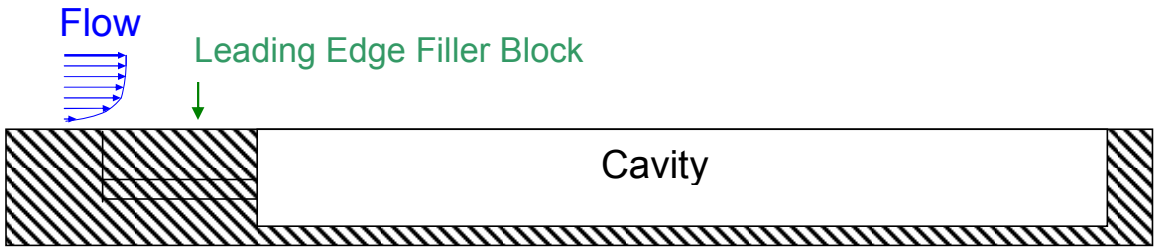

Figure 13. Test Configuration 3: Baseline Cavity - Side View Sketch

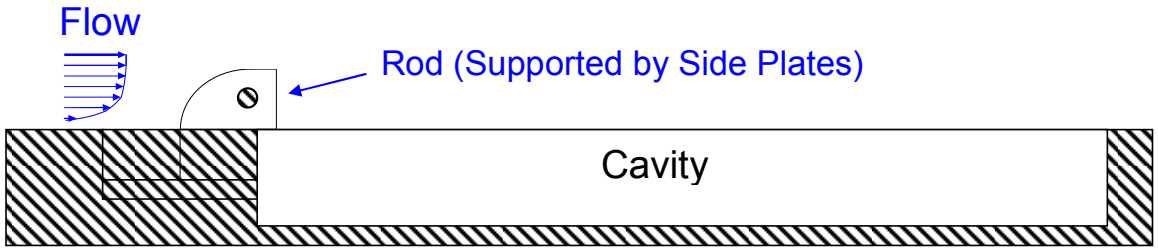

Figure 14. Test Configuration 4a: Rod with Cavity - Side View Sketch

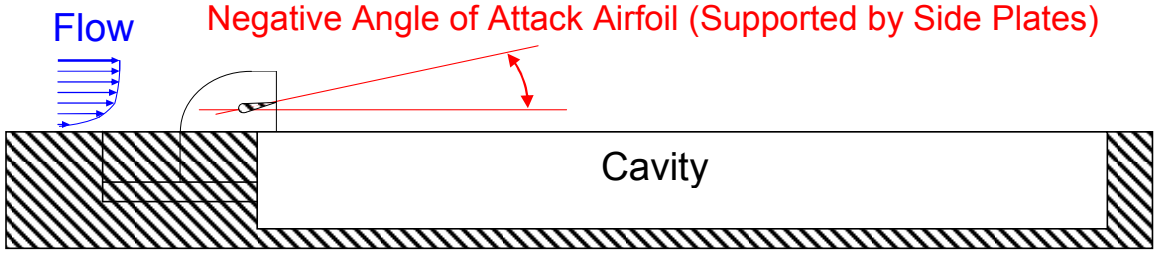

Figure 15. Test Configurations 4b, 4c and 4d: Airfoil at 0, -5, -10 Angles of Attack with Cavity - Side View Sketch

Chapter 2

TECHNICAL REVIEW

Cavity Flow Terminology

Cavity flow research often includes specific terminology related to geometry and flow conditions for the region preceding the cavity and for the region which spans the cavity itself. Figure 16 provides a sketch of some key parameters required for explaining cavity flow behaviour. The properties shown are deemed important for describing cavity flow regardless of it occurring in the incompressible or compressible regimes. The parameters are also pertinent for both turbulent and laminar flow conditions.

Terminology used for the upstream flow conditions preceding a cavity are typically identical to terminology used for describing flat plate flow fields.

1. Velocity of freestream (U): Freestream velocity is of importance relating to the Reynolds number and Mach number of the incoming flow.

2. Reynolds number (Re): The Reynolds number is a non-dimensional quantity which is a function of fluid density, viscosity, velocity and a reference length ($\mathrm{Re} = \frac{\rho U L}{\mu}$). Reynolds number is a ratio of inertial to viscous forces. It is a key parameter relevant to the boundary layer properties of the oncoming flow.

3. Mach number (M): Mach number is a non-dimensional number of the velocity divided by the speed of sound ($M = \frac{U}{a}$). The Mach number is of importance to determination of whether a flow is within the compressible or incompressible regimes. If a flow is within the compressible regime, it is used to further categorize between subsonic, transonic and supersonic flow.

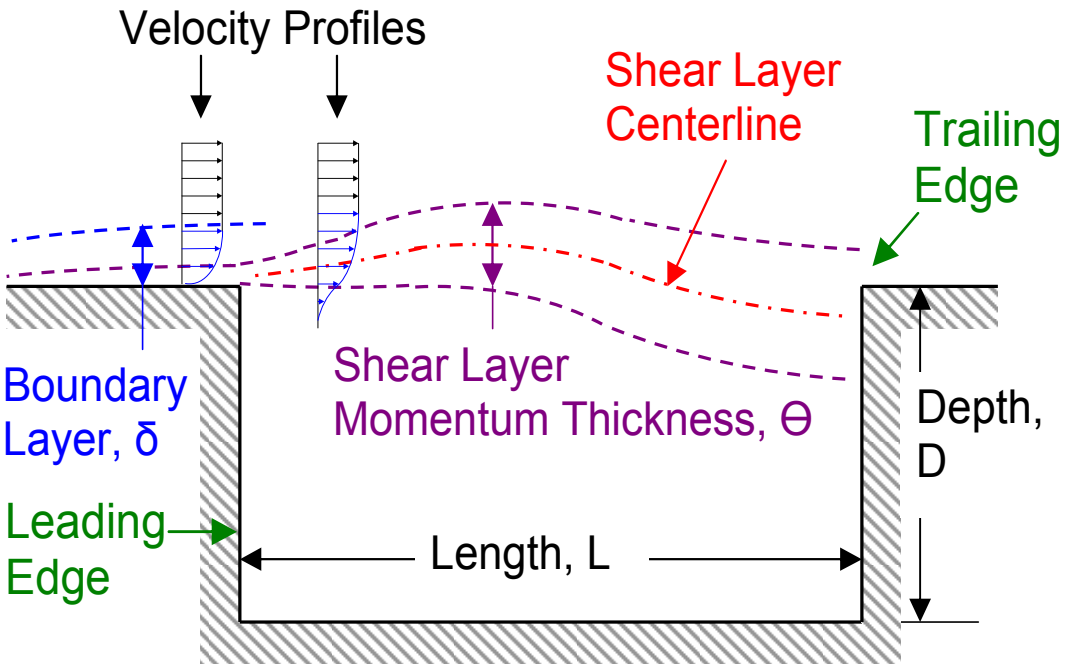

Figure 16. Flow and Geometry Parameters Typically Applied for Describing Cavity Flow

4. Boundary layer thickness (δ): A boundary layer is a direct result of the no slip boundary condition being imposed on a viscous flow. The boundary layer thickness represents the amount of perpendicular distance required for a velocity profile to go from zero at a solid surface to 99% the velocity of a freestream flow. Boundary layer thickness is typically used as a key parameter for the research and development of cavity flow control techniques.

5. Momentum thickness (θ): For typical plane flow cases, momentum thickness may be applied for the purposes of determining drag force on a flat plate. However, momentum thickness is of particular importance within cavity flow as it is used to quantify the shear layer prior to encountering the leading edge of the cavity.

6. Vorticity (ω): Vorticity is a parameter that represents the curl of a velocity vector field ($\omega = \vec{\nabla}$ x $\overrightarrow{V}$) and is a measure of circulation within a flow field. Vorticity is a quantity typically calculated through particle image velocimetry (PIV) post processing and may be used for visual identification of the wall bounded shear layer that forms prior to encountering the leading edge of a cavity.

Flow conditions spanning the cavity are typically time dependent in nature since the velocity profiles are functions of both position and time along the length of the cavity. Some of the key geometry and flow parameters include:

1. Length (L) and Depth (D): Both length and depth are used to determine the cavity's length to depth ratio (L/D). L/D is often used to categorize between open, closed and transitional cavities as described by Chen [1] for subsonic and transonic flow conditions or by Plentovich, Stalling & Tracy [3] for supersonic flow conditions.

2. Width (W): Cavity width is a parameter researched to a lesser extent than both cavity length and depth. However according to Tracy and Plentovich [6], there are examples where increasing cavity width will cause an increase in resonance.

3. Vorticity (ω): Vorticity created within the wall bounded shear layer prior to encountering the cavity leading edge may continue within the detached shear layer that spans across a cavity. As described by Radhakrishnan [7], shear layers spanning cavities are inherently unstable and typically include vorticity fluctuations within.

4. Momentum thickness (θ): Momentum thickness is a key parameter by which the detached shear layer spanning the cavity is quantified. As the detached shear layer travels from the leading edge to the trailing edge of the cavity, the shear layer instabilities are amplified. This amplification is quantified by variations in

the shear layer momentum thickness. The behaviour of the shear layer is further complicated when it comes into contact with the cavity trailing edge structure to create upstream travelling influences which further modify the detached shear layer.

5. Dynamic pressure: Dynamic pressure refers to measurements which are typically taken from the rear floor of a cavity as depicted within Figure 17. Upstream travelling influences related to a cavity detached shear layer coming into contact with the trailing edge structure of a cavity typically result in cavity pressure fluctuations. Dynamic pressure data collected over time are used for calculation of spectrum data in the frequency domain for identification of cavity broadband noise levels and resonance tones.

6. Sound pressure level: Sound pressure level (SPL) is a logarithmic representation for the ratio of a measured pressure compared with the reference pressure of barely audible sound. SPL may be calculated by Equation (1):

$$dB\,SPL = 20\log_{10}\left[\frac{p}{p_{ref}}\right] \qquad (1)$$

Where $dB\,SPL$ is sound pressure level in a decibel scale, p is pressure typically in units of Newton/meter^2 (N/m^2) or pound/inch^2 (lb$_f$/in^2), p_{ref} is the reference pressure for the minimum threshold of human hearing which is: 2.0 x 10^{-5} N/m^2 or 2.9 x 10^{-9} lb$_f$/in^2. Cavity flow suppression techniques often quantify effectiveness by SPL comparison between the suppressed cavity with the baseline (unsuppressed) cavity. Table 1 reproduced from Loewen [5] provides sample SPL with associated pressure unit comparison data. Table 1 also illustrates that an increase in 10 dB represents an over triple increase in pressure magnitude.

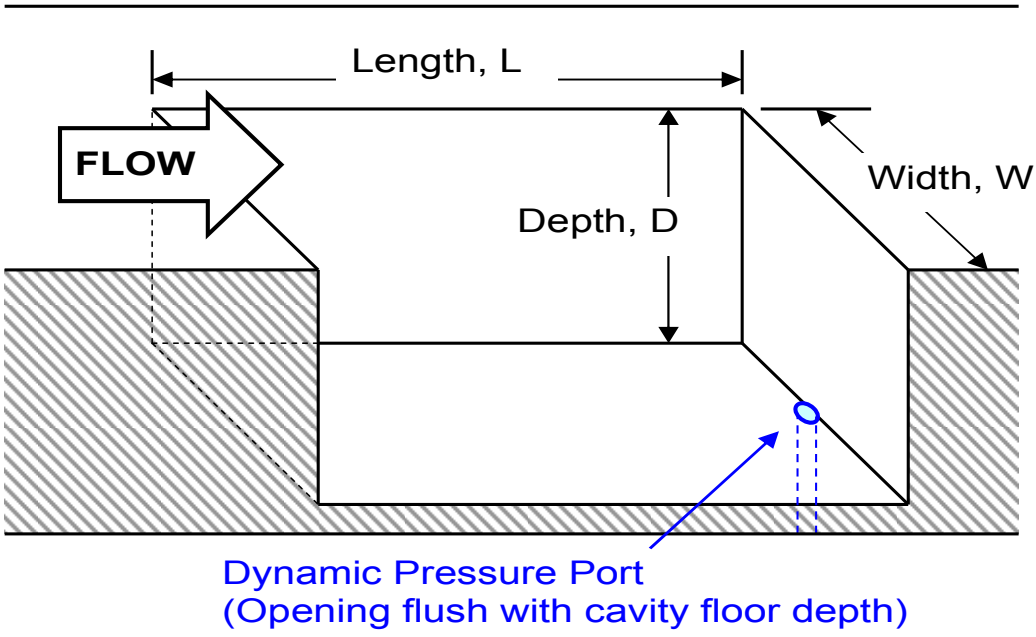

Figure 17. Typical Location of Dynamic Pressure Transducer within Cavity

Table 1: Conversion of dB SPL to Metric and English Pressure Values (from Loewen [5])

Sound Pressure Level, dB SPL	Pressure, p [N/m^2]	Pressure, p [lbf/in^2]
100	2.0	0.000290
125	35.6	0.00516
150	632	0.0917
160	2000	0.290
175	11250	1.63

Cavity Flow Review

In 1955 one of the first to research cavity flow over various L/D was Karamcheti [8] through experiments of varying lengths of shallow wall gaps with Mach numbers ranging between 0.4 and 0.8. Karamcheti examined acoustic radiation levels and used Schlieren photography for flow field visualization. His observations included that along with periodic pressure fluctuations are also strong acoustic radiation from the cavity. Karamcheti noted that pressure fluctuation frequency increases with increases in airspeed. He also noted that that pressure fluctuation frequency decreases with cavity length increases.

Virtually at the same time as Karamcheti, Roshko [9] studied cavity flow for the purposes of gaining understanding of the drag forces that cavities exhibit. He studied the pressure and velocity flow fields of low speed flows between 75 ft/sec to 210 ft/sec for shallow cavities of L/D between 10.6 and 62.5. Roshko noted that "*the formation of the vortex occurs by the deflection of part of the separated boundary layer into the cavity, this deflection occurring at the downstream edge and creating a relatively high pressure on the cavity wall in that vicinity.*"

In 1964, Rossiter [10] studied a series of rectangular cavities within the Mach number range between 0.4 and 1.2. His testing included a cavity with 8 inch length, 4 inch width and an adjustable depth from 0.8 to 8 inch for providing variable L/D. His first conclusion was that "*... unsteady pressures acting in and around a rectangular cavity may contain both random and periodic components. In general the random component predominates in shallow cavities ($L/D > 4$) and the periodic component predominates in deep cavities ($L/D < 4$).*" His second conclusion stated "*the random component is most intense near the wall of the cavity.*" Rossiter's third conclusion was that "*…periodic pressure fluctuations appear to be due to an acoustic resonance within the cavity.*" These conclusions represented a significant advance to understanding parameters required for explaining cavity flow behaviour. However, Rossiter's most cited contribution of cavity flow literature is the empirical Equation (2):

$$f = \frac{U}{L}\frac{(m-n)}{\left(\frac{1}{K_v}+M\right)} \tag{2}$$

Where f is the cavity frequency, U is the freestream velocity, L is the cavity length, m is the cavity oscillation mode number, n is the phase delay between an acoustic wave and a new vortex, K_v is the ratio of convective velocity of vortices to freestream velocity and M is the Mach number. Rossiter derived a phase delay of $n = 0.25$ and a convective to freestream ratio of $K_v = 0.57$ for a $L/D = 4$.

According to cavity flow research completed in 1971 by Heller, Holmes and Covert [11], the empirical Equation (2) developed by Rossiter showed strong agreement with experimental data collected at Mach numbers of 0.8 and 1.5 but showed poor agreement at Mach numbers of 2 and 3. They noted that Rossiter had assumed the speed of sound within the cavity, a_c to be the same as the freestream speed of sound, a_∞. Heller, Holmes and Covert conducted tests with a temperature probe placed at the bottom of their cavity to compare cavity temperature, T_c with freestream stagnation (total) temperature, T_o and freestream static temperature, T_∞. Their results showed the cavity temperature to be closer to the freestream stagnation temperature ($T_c \approx T_o$). As speed of sound is a function of temperature, this led to assuming the cavity speed of sound to be approximately equal to the freestream stagnation speed of sound ($a_c \approx a_o$) for the development of the modified Rossiter Equation (3):

$$S = \frac{fL}{U} = \frac{(m-n)}{\left\{\frac{M}{\left[1+\frac{(\gamma-1)}{2}M^2\right]^{1/2}}+\frac{1}{K_v}\right\}} \tag{3}$$

Where γ is the ratio of specific heats, S is the Strouhal number and all other variables are the same as described for Equation (2). It must be noted that although the modified Rossiter Equation (3) may show strong agreement for predicting frequencies of cavities experiencing self sustained oscillations, it does not predict if or if not these oscillations will actually occur in a cavity. Nor does the equation predict the amplitudes of properties such as sound pressure level (SPL) for cavities experiencing self sustained oscillations.

In 1975, Heller and Bliss [12] carried out an experimental and analytical research program to gain improved understanding of the physical mechanisms controlling the occurrence of pressure oscillations within cavities. Their testing included using a wind tunnel with Mach numbers from 0.8 to 2.0 and cavities with L/D ranging from 2.3 to 5.5. A water tunnel was used for smaller scale tests at lower mach numbers. Their water tunnel visualization identified the unsteady shear layer motion being responsible for mass addition and removal at the cavity trailing edge which led to a proposed six step oscillation cycle as shown in Figure 18. Their six step feedback cycle included showing how mass addition and removal at the cavity trailing edge produced forward travelling waves that would propagate from the trailing edge bulkhead and then reflect from the leading edge bulkhead to become rearward travelling waves. Heller and Bliss identified the resulting wave structure within the cavity to be the driving force of the unsteady motion of the shear layer over the entire cavity length. They referred to their process as a "pseudo-piston" model as depicted within Figure 19. Heller and Bliss used their observations to construct an analytical model for the prediction of cavity pressure mode shapes with some of the following general considerations:

1. "*The fluid motion within the cavity is governed by the wave equation in a region bounded by a rigid front bulkhead and floor, with a free shear layer on top, and a rear bulkhead that oscillates like a piston.*"

2. "*The external flow is governed by the convective wave equation. The internal and external solutions must be joined by applying the proper dynamic and kinematic conditions across the shear layer.*"

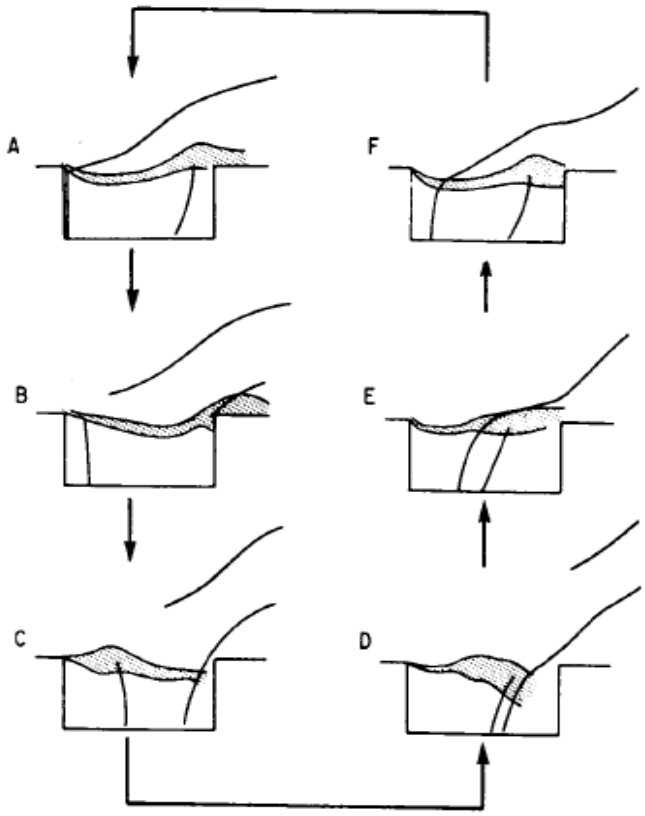

Figure 18. Proposed Cavity Oscillation Cycle (from Heller & Bliss [12])

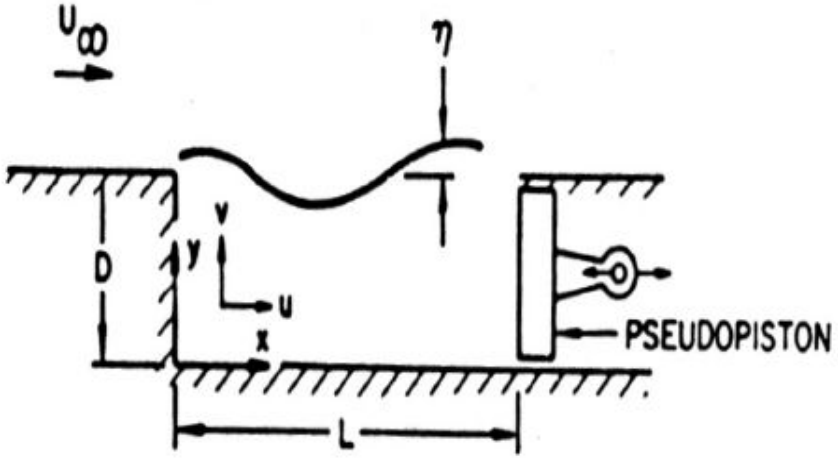

Figure 19. Proposed Simple Analytical "Pseudo-Piston" Cavity Model (from Heller & Bliss [12])

3. "*The effect of the trailing-edge mass addition and removal process is accounted for entirely by the equivalent oscillation of the rear bulkhead.*"

Unfortunately Heller and Bliss did not include an equation form or a partial differential form of their analytical model within their paper. However, they did present plots to support that their analytical model was able to predict the lowest pressure mode shapes in agreement with their cavity experimental data. A limitation of their model was that it could not predict the higher pressure mode shapes which did occur within their experimental data.

From 1977 to 1978, Tam and Block [2] investigated cavities in the low subsonic range for Mach numbers varying from 0.1 to 0.4. Along with their experimental data, they presented a mathematically rigorous cavity flow analytical model. Unlike previous cavity flow studies, their model accounted for the acoustic reflections from the bottom and leading edge walls of the cavity. Originally they modelled the shear layer spanning the cavity to have negligible thickness. After comparison with their experimental data, they improved their model to account for the finite shear layer thickness effects. Tam and Block noted that the thickness of the shear layer spanning the cavity increases in the downstream direction and that its rate of growth depends on the amplitude of cavity oscillation. Thus they applied mean momentum thickness, θ for the purpose of quantifying the shear layer into their model. As the model proposed by Tam and Block was applicable to the low subsonic range, it was not applied within this supersonic cavity flow study. However, a highly significant contribution of their research was noting that momentum thickness to length ratio, θ/L plays a significant factor for cavity flow behaviour in addition to L/D.

As a result of cavity flow not being fully understood, history has shown a strong reliance on empirical methods for explaining cavity flow behaviour. In some cases, numerical methods used for modelling cavity flows have shown strong agreement with experimental methods. A prime example of this success includes the research completed by Radhakrishnan [7] in 2002 which included cavities with L/D from 2.0 to 4.5 with Mach numbers ranging from 0.3 to 0.6.

Radhakrishnan showed that a commercial code (CFD-ACE) could be used to predict all the major features of the cavity flow field as observed by his experimental results.

It must be noted that there are a vast number of examples of cavity flow research papers that were not discussed within this review. A goal of this review was to show the great challenges involved with the provision of both a useable and a comprehensive model to explain cavity flow behaviour.

Cavity Flow Control and Acoustic Suppression Review

Cavity flow research may provide numerous benefits for aerodynamic vehicles which include: landing gear compartments, weapons bays and other potential applications. Unfortunately due to the unsteady nature of cavity flow applications, there are also numerous challenges that could potentially be hazardous to the safety of flight of aerodynamic vehicles configured with cavities. Almost as early as cavity flow research originated, cavity flow control techniques became of interest for the suppression of flow oscillations and noise reduction.

In 1964, Rossiter [10] tested three different rectangular spoiler configurations which were positioned vertically at the cavity leading edge similar to the blockage schematic shown earlier within Figure 6. Rossiter's tests were completed with a deep cavity L/D of 1 at Mach numbers of 0.7, 0.9 and 1.2. The experimental results showed the largest spoiler tested to provide the best acoustic suppression. All three spoiler configurations were also shown to provide the largest suppression influence at the lowest tested Mach number of 0.7.

In 1975, Heller and Bliss [12] developed their own suppression techniques. They stated "*Oscillation amplitudes can be reduced by the stabilization of the shear layer, by the prevention of the periodic trailing-edge mass addition process, or by a combination of both.*" One of their suppression techniques to stabilize the shear layer included using two vortex generators in front of the cavity leading edge. To prevent the trailing edge mass addition process, they used a 45 degree trailing edge slant within the cavity for a suppression technique. Figure 20 depicts

approximately a 20 dB reduction in the peak amplitude with the application of the slanted trailing edge and the leading edge vortex generators (at approximately 250 Hz).

By 1979, Clark [13] applied suppression techniques proposed by Rossiter, Heller, Bliss and others for the testing of a cavity model that included greater complexity than a typical L/D rectangular cavity. The model included a scaled-down F-111 "Aardvark" with its associated detailed geometry weapons bay. The test program included various spoilers which were positioned vertically at the cavity leading edge such as sawtooth spoilers and perforated spoilers. Rear ramp deflectors like those suggested by Heller and Bliss were also evaluated. Of all the devices tested, the sawtooth spoiler was deemed to provide the best cavity flow suppression. Since the time of the Clark's testing, other aircraft have also had their weapons bays configured with typically vertical spoilers such as the retractable porous spoiler of the F-117 "Nighthawk".

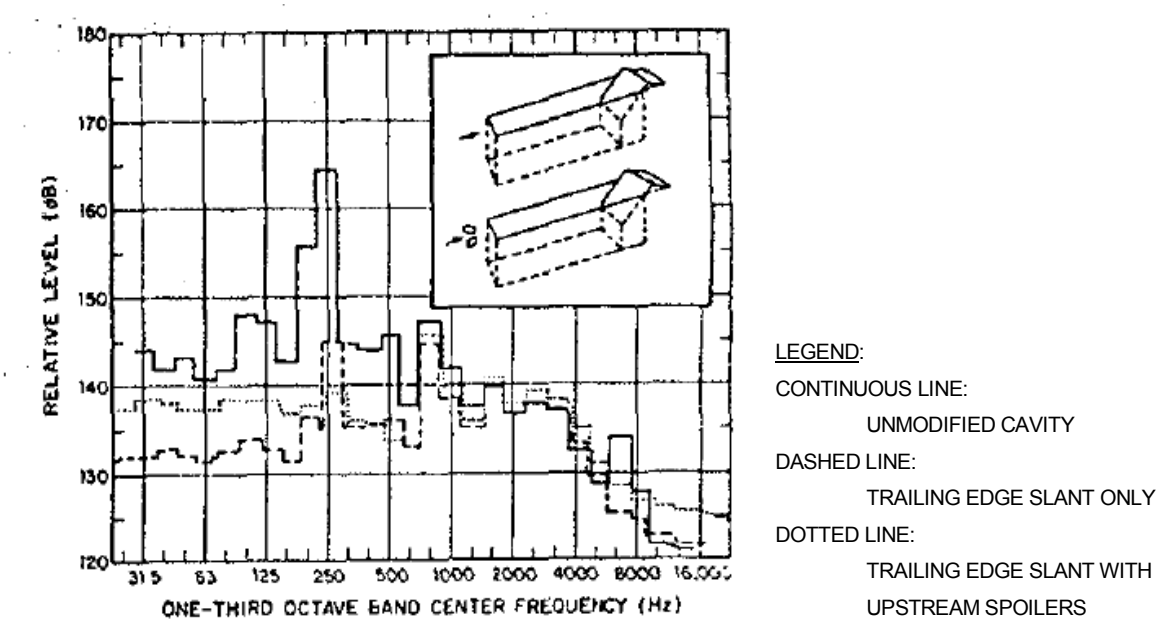

Figure 20. Effect of Trailing Edge Slant with & without Upstream Spoilers on Cavity with L/D of 2.4 and Flow Mach number of 0.8 (from Heller & Bliss [12])

Although vertical spoilers have demonstrated an ability to reduce cavity oscillations at various design conditions, vertical spoilers typically represent a flow blockage. In many cases these flow blockages protrude approximately one boundary layer thickness into the crossflow upstream of the cavity. As illustrated by Figure 21 of the NASA Glenn Research Center [14], a vertical flat plate within a crossflow may have a much larger drag contribution than other geometry objects with equivalent frontal areas. This observation has motivated further research and development for more efficient and sophisticated methods of cavity flow control. Another criticism of vertical spoilers is that although they may be moderately effective in the subsonic regime, vertical spoilers tend to lose most of their effectiveness in the supersonic regime. However, this particular criticism is still debated among cavity flow researchers.

Another method of cavity flow control may be achieved by upstream mass injection as depicted earlier within Figure 5. The method includes mass injected from a porous surface into a crossflow for the purpose of reducing or eliminating cavity oscillations. Vakili and Gauthier [15] applied mass injection upstream of a cavity leading edge as depicted within Figure 22.

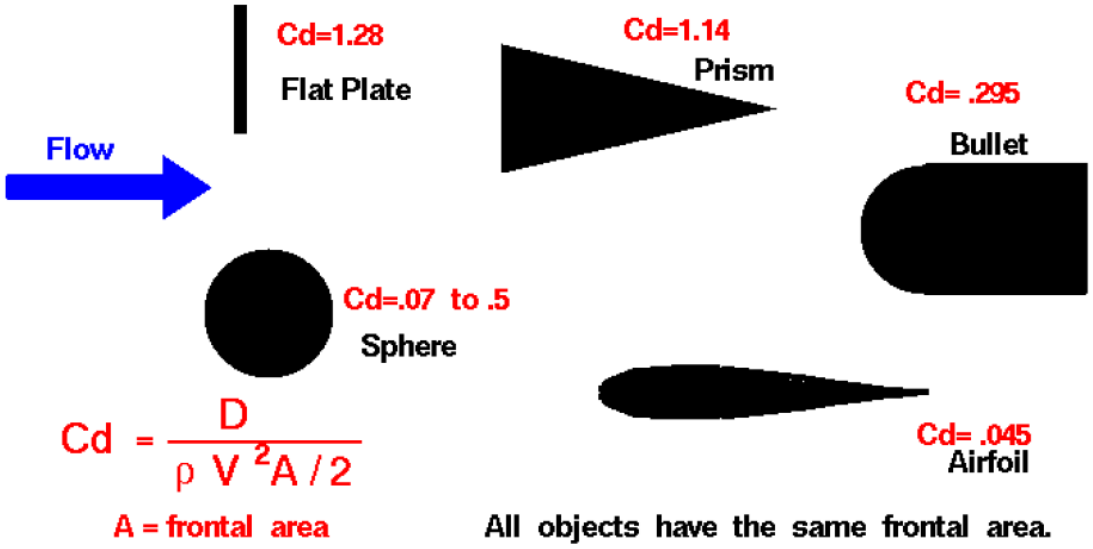

Figure 21. Typical Values of the Drag Coefficient for a Variety of Shapes (NASA Glenn Research Center [14])

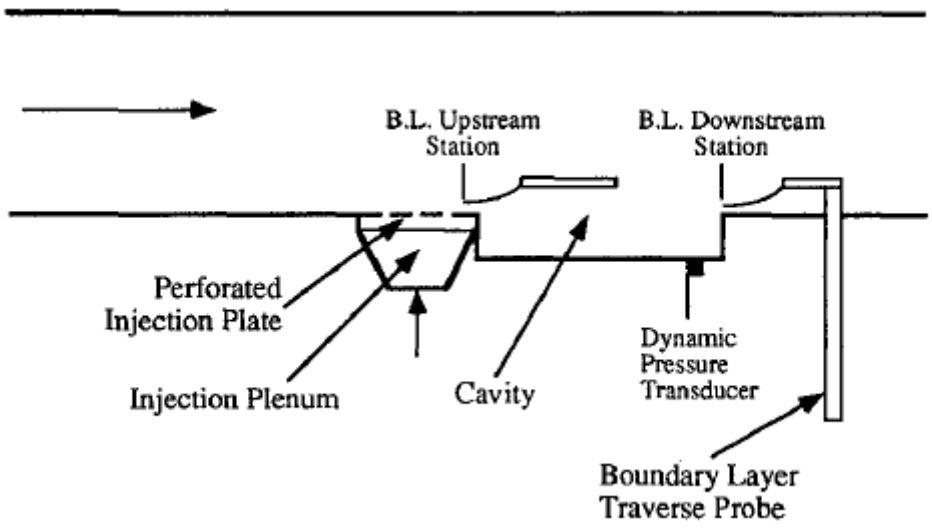

Figure 22. Control of Cavity Flow by Upstream Mass-Injection Schematic (Vakili & Gauthier [15])

They reported that upstream mass injection could provide as much as a 27 dB reduction in cavity oscillation amplitude for tests performed at a Mach number of 1.8 and a cavity L / D of 2.54. Vakili and Gauthier attributed the method to cause thickening of the shear layer spanning the cavity. The thicker shear layer would then have different instability characteristics including a different vortex frequency from the natural frequency of the cavity.

A contemporary method of cavity flow control that has received a great deal of attention within recent years is "high frequency forcing" also known as "high frequency suppression". In 1998, Wiltse and Glezer [16] conducted tests by studying a turbulent jet emanating from a square duct. They developed the term high frequency forcing to represent the action of forcing the flow at roughly an order of magnitude lower than the passage frequency for the smallest measurable eddies. They postulated that small scale excitation could result in an enhanced energy transfer from small scales to larger scales for further dissipation of turbulent kinetic energy.

In 2002, Stanek, et al [17] having access to the high frequency forcing data collected by Wiltse and Glezer [16] presented a new model for the high frequency suppression of shear layers. Stanek, et al argued that the high frequency forcing model presented by Wiltse and Glezer did

not obey established turbulence "laws" based on the argument that forcing at high frequencies of smaller scales cannot draw energy away from larger scales. It is likely that their argument was based on the Kolmorgorov Hypothesis for turbulent flow for which the first assumption is: "*The smallest eddy is statistically independent of the largest eddy*" and the second assumption is "*the rate of energy dissipation of the smallest eddy is equal to the rate of supply of energy from largest eddy*". Stanek, et al [17] stated that high frequency forcing "… *suppressed the growth of large scale structures, which resulted in a reduced level of turbulent kinetic energy in the large scales.*" Stanek, et al based the success of high frequency forcing due to reducing turbulent energy in the larger scales which would result in less of a need for energy dissipation within the smaller scales.

The concept of high frequency forcing has been popularized as a method of cavity flow control by the rod in crossflow technique depicted earlier within Figure 7. The use of placing a cylindrical rod above the leading edge of a cavity is argued to be a high frequency forcing device through the production of vortex shedding. However to the present day, there are still those that believe the rod in crossflow technique primarily acts like a spoiler or that the main contribution of the technique is lofting or thickening of the shear layer spanning a cavity.

In 2003, Stanek, Ross, Odera and Peto [18] presented research with the aim of understanding the relationship between high frequency forcing and the rod in crossflow technique. Their tests included a cavity with 20 inch length, 4 inch depth, and 4 inch width for an open cavity L/D of 5. Their subsonic tests at a Mach number of 0.85 showed as much as a 10 dB reduction in Rossiter tones compared from the unsuppressed baseline cavity. Their supersonic tests at a Mach number of 1.19 showed as much as a 16 dB reduction in Rossiter tones compared from the unsuppressed baseline cavity. The test program included different diameter rods and different height locations for the rod placement within the boundary layer upstream of the cavity leading edge. Stanek, Ross, Odera and Peto included a guideline for establishing a "maximum suppression rod" denoted within Equation (4):

$$D_{optimum} = H_{optimum} = \frac{2}{3}\delta \qquad (4)$$

Where $D_{optimum}$ is optimum rod diameter, $H_{optimum}$ is optimum rod height above the cavity leading edge and δ is the boundary layer thickness upstream of the cavity leading edge. They also introduced the concept of using semi-circular side plates (rod end-caps) to determine if they influenced rod shedding. They observed that rod shedding in a supersonic flow could be significantly improved with rod end-caps. In contrast, their sub-sonic tests showed very little vortex shedding influence provided by rod end-caps. Stanek, Ross, Odera and Peto summarized their results to state "*This is the first work to unequivocally link high frequency rod shedding to enhance acoustic suppression performance.*" They also included "*The ONLY device which has been proven to date to achieve substantial acoustic suppression DUE TO HIGH FREQUENCY PULSING, is the rod in crossflow.*"

In 2008, Loewen [5] applied the rod in crossflow technique for a cavity flow study using the High Speed Wind Tunnel (HSWT) in the UTSI Gas Dynamic Laboratory. His testing was completed within the subsonic regime with a Mach number of 0.52 and a cavity L/D of 3.5. Loewen's tests included three different rod diameters of: 1/8 inch, 3/16 inch and 1/4 inch. His best results were achieved with the 1/4 inch rod which provided 15.1 dB of acoustic suppression. One of Loewen's conclusions was "… *the suppression of cavity tones was apparently the blockage and lofting effect from the rod, as opposed to a high frequency effect.*"

The conclusion of Stanek, Ross, Odera and Peto [18] in contrast to the conclusion of Loewen [5] exemplifies the disagreement that exists to this day as to whether the rod in crossflow technique primarily acts as a high frequency forcing mechanism through vortex shedding or alternatively works through effects such as lofting or thickening of the shear layer spanning a cavity. One of the motives regarding this current thesis is to compare the rod in crossflow technique with another technique where very minimal vortex generation is expected.

The technique of using an airfoil in a crossflow was depicted earlier within Figure 8 and has received very little attention in comparison to techniques such as the vertical spoiler, mass injection or the rod in crossflow. In 1975, Franke and Carr [19] tried a vast number of potential

devices to determine possible candidate techniques for the suppression of flow-induced pressure oscillations within cavities. Their initial testing was completed with a water tunnel and a cavity of 7 inch length and 3.5 inch depth. Flow phenomena were observed visually through dye injection. Most of their tests focused on modifying the geometry of the cavity by altering the angles of the leading and trailing edge surfaces. However, one of their test configurations described the use of an airfoil placed above the cavity leading edge. Franke and Carr stated "*When the* [airfoil shaped] *spoiler was positioned at a small negative angle of attack (approximately 10 degrees) the shear layer did not enter the cavity*". Unfortunately Franke and Carr did not include the dimensions of their airfoil nor did they choose to test the configuration further. However, Franke and Carr's description does provide motivation to see how much suppression of cavity tones could be provided by an airfoil in crossflow. It would be beneficial to see if the airfoil creates a lofting or thickening effect on the cavity spanning shear layer. From Figure 20, another potential benefit of an airfoil within a crossflow may be a smaller drag contribution than for a rod in crossflow with an equivalent frontal area.

Chapter 3

EXPERIMENTAL APPROACH

Introduction

This chapter includes a full description of the High Speed Wind Tunnel (HSWT) of the University of Tennessee Space Institute (UTSI) Gas Dynamics Laboratory. It includes a prediction of flow conditions within the test section based on isentropic compressible flow calculations. Instrumentation used for testing is organized into multiple sections. The setup of the static pressure ports and dynamic pressure transducers are described with respect to their test section locations. The basis of the Schlieren photography technique is described along with the particular setup used for this study. An explanation of the Particle Image Velocimetry (PIV) flow visualization technique is followed with the selection criteria applied for the determination of the PIV user setting parameters. The PIV sections are concluded with post-processing techniques which include vector validation procedures and data presentation using Tecplot. Criteria used for the "rod in crossflow" and "airfoil in crossflow" designs are followed by depictions of the various test configurations used for each phase of testing.

High Speed Wind Tunnel

The High Speed Wind Tunnel operates via a blow-down configuration. An external compressor is used to pressurize the outdoor tank farm photographed within Figure 23 which consists of 18 high pressure cylinders for a maximum capacity of 3000 pound/inch^2 (PSI). The tank farm provides a reservoir of compressed air to the tunnel which is released through the ValTek FlowServe valve depicted within Figure 24. The Valtek FlowServe valve controls the compressed air mass flow rate, $\dot{m}$ through a LabVIEW virtual instrument. The compressed air flows into the stilling chamber which includes a four section plenum. The stilling chamber as shown in Figure 25 homogenizes the flow by a series of honeycomb grids and screens. Within the stilling chamber, the stagnation (total) temperature, T_o and the stagnation pressure, p_o are measured. As depicted within Figure 26, air flows through a converging/diverging nozzle

designed for bringing the flow to a Mach number of 1.85 as it reaches the test section. The test section consists of an 8 inch by 8 inch square duct approximately 4 feet long. Glass observation windows are included on its top and side surfaces for enabling Schlieren photography or PIV applications. Along the test section floor, there are various ports for measuring static pressure, p. Following the test section, air is routed and diffused to atmospheric conditions.

Although the converging/diverging nozzle is designed to provide the test section with a Mach number of 1.85, in practice it provides an extremely stable Mach number of 1.84 once the stilling chamber reaches enough pressure to bring the nozzle throat to a choked condition. For Mach 1.84 flow, the ValTek FlowServe valve is generally set to provide a mass flow rate, $\dot{m}$ of 26 pound/second (lb_m/s). It must be noted that prior to reaching a choked condition, the converging/diverging nozzle may be used to provide other Mach numbers for different mass flow rates. However, this requires careful set point selection and valve tuning to maintain a steady flow.

Figure 23. Outdoor Tank Farm of 18 High Pressure Cylinders

Figure 24. ValTek FlowServe valve

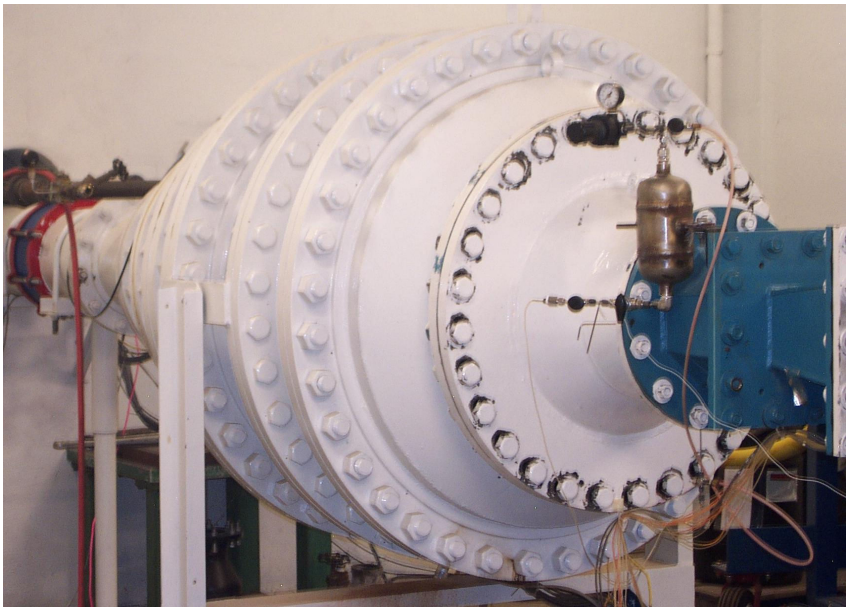

Figure 25. Stilling Chamber

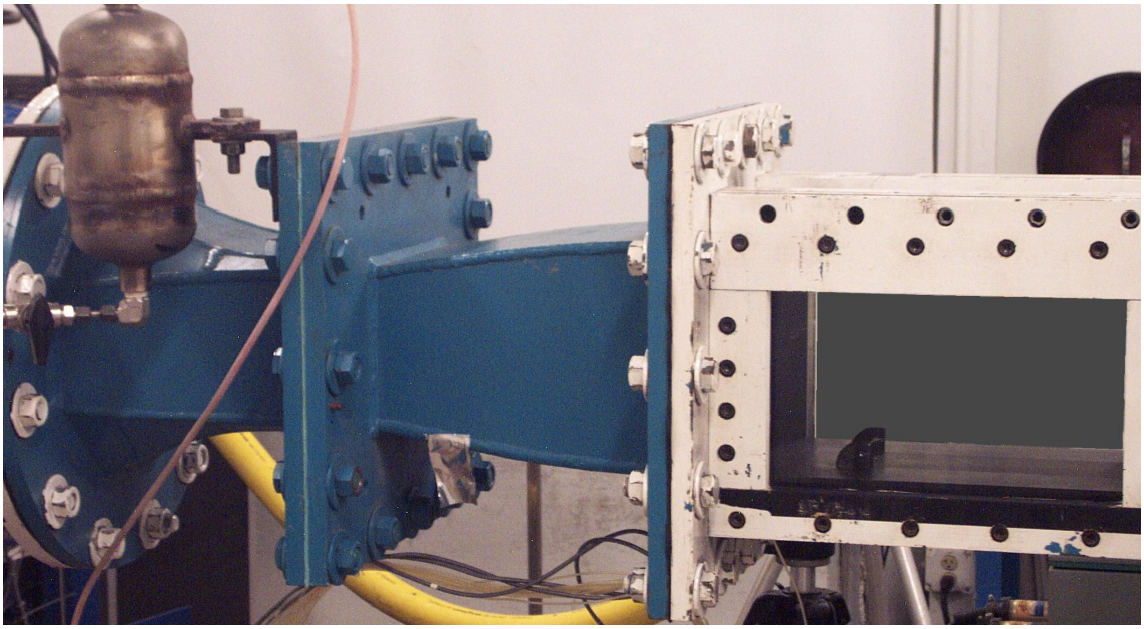

Figure 26. Converging/Diverging Nozzle Followed by Test Section

High Speed Wind Tunnel Test Conditions

In addition to data collection and valve control, the LabVIEW virtual instrument calculates Mach numbers at each test section static pressure port via the isentropic pressure ratio formula shown by Equation (5):

$$M = \sqrt{\left(\frac{2}{\gamma - 1}\right)\left[\left(\frac{p_o}{p}\right)^{\frac{\gamma-1}{\gamma}} - 1\right]} \qquad (5)$$

Where M is Mach number, γ is the ratio of specific heats (typically 1.4 for dry air), p_o is stagnation pressure measured within the stilling chamber and p is static pressure measured within the test section.

Isentropic flow equations may be applied further to provide an approximation of the static temperature within the test section as shown by Equation (6):

$$T = \frac{T_o}{1 + \frac{\gamma - 1}{2} M^2} \tag{6}$$

Where T is static temperature calculated for the test section, T_o is stagnation temperature measured within the stilling chamber and all other variables are the same as described for Equation (5).

The local speed of sound within the test section may be calculated with Equation (7):

$$a = \sqrt{\gamma R T} \tag{7}$$

Where a is the speed of sound, γ is the ratio of specific heats (typically 1.4 for dry air), R is the perfect gas constant (typically $1716.59 \frac{ft^2}{s^2 \cdot °K}$ or $287.058 \frac{m^2}{s^2 \cdot °K}$ for dry air) and T is the static temperature within the test section.

The measured quantities within the stilling chamber and test section along with application of isentropic equations may be further be used to estimate the freestream velocity within the test section via Equation (8)

$$U = Ma \tag{8}$$

Where U is the predicted freestream velocity within the test section, a is the local speed of sound within the test section and M is the Mach number.

Table 2 applies some sample measured data from a preliminary HSWT test run. In general, the HSWT operates at a very stable Mach number of 1.84 once its converging diverging nozzle

Table 2: Sample Predicted Freestream Velocity within Test Section

Stagnation Temperature		Stagnation Pressure		Static Pressure		Mach Number	Freestream Velocity	
T_o *Stilling Chamber Measured*		p_o *Stilling Chamber Measured*		p *Test Section Measured*		M *Equation (5) Calculated*	U *Equations (6), (7) & (8) Calculated*	
$^\circ R$	$^\circ K$	*PSI*	*Pa*	*PSI*	*Pa*	-	ft/s	m/s
530	294	29.6	2.04E+5	4.91	3.39E+4	1.831	1598	487.1
533	296	30.6	2.11E+5	5.01	3.45E+4	1.840	1609	490.3
532	295	30.6	2.11E+5	4.96	3.45E+4	1.846	1609	490.5

reaches a choked condition. With the application of isentropic flow equations, the freestream velocity within the test section is estimated to be roughly 1600 feet/second (ft/s) or 490 meter/second (m/s)

Pressure Measurement

Figure 27 shows the placement of the static pressure port and the dynamic pressure transducer for both the solid floor plate and cavity configurations. The static pressure port is placed upstream of the model for the calculation of freestream flow properties including Mach number. All test configurations include a dynamic pressure transducer placed near the trailing edge of the cavity floor or the trailing edge of the solid floor plate (for non-cavity configurations). The pressure measurement output is sent to the Tunnel control computer and processed through LabVIEW. The dynamic pressure data is collected in Pascal (Pa) units at a 40,000 Hertz (Hz) sampling frequency. The LabVIEW virtual instrument generates a "raw data" file of the dynamic pressure data in Pascal (Pa) units within the time domain and a "spectral data" file of sound pressure levels in a decibel scale (dB SPL) within the frequency domain to a maximum of 20,000 Hz. The "raw data" file may also be imported into Matlab for the purposes of validating the "spectral data" file or for the computation of power spectral density (PSD) in energy units of Pascal^2/Hertz (Pa^2/Hz). The associated Matlab code for spectrum calculations is included within Appendix 1. The spectrum data is used for identification of cavity broadband noise levels and resonant tones.

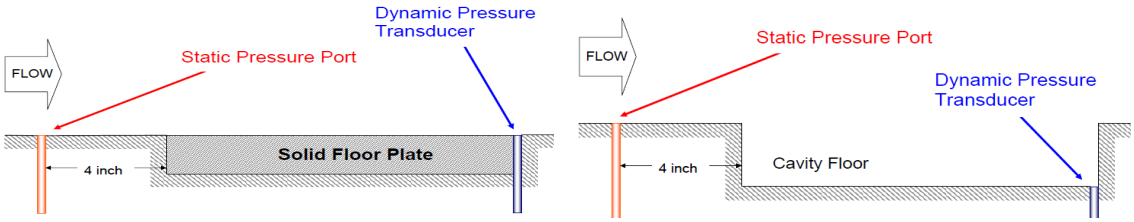

Figure 27. Pressure Transducer Locations for Solid Floor Plate (left) and Cavity (right) Configurations

Schlieren Photography Technique

Schlieren photography was developed as a relatively simple method for analysis of supersonic flow. Supersonic flow interactions experience significant density changes which cause index of refraction changes. Uniform light passing through the flow field experiences distortion due to the index of refraction changes. The projection of the distorted light provides flow visualization.

The HSWT Schlieren setup is sketched within Figure 28. It comprises of a light source transmitted through a convex lens as depicted within Figure 29. The projected light is reflected from a spherical concave mirror as shown by Figure 30. The reflected light passes through the test section to be reflected again by an identical spherical concave mirror. Figure 31 depicts the plane mirror with the razor blade configured for the reflection of light onto the white screen. The razor blade is positioned to partially block some light from reaching the viewing screen to minimize off-axis aberrations. A video camera is used to record images from the white screen..

The Schlieren setup for use with the HSWT does not depict the entire flow field across the test cavity (or the solid floor plate when applicable). The field of view is limited by the test section window size and by the reflection of the spherical concave mirrors. Figure 32 depicts the field of view provided by Schlieren setup. The 8.85 inch horizontal field of view (HFOV) is positioned to show roughly 2.73 inch of tunnel floor upstream of the cavity and 6.12 inch of length along the cavity. This results in the flow structure above the cavity trailing edge not being visible. With this limitation considered, the Schlieren setup still provides visualization for a region greater than half of the total cavity length.

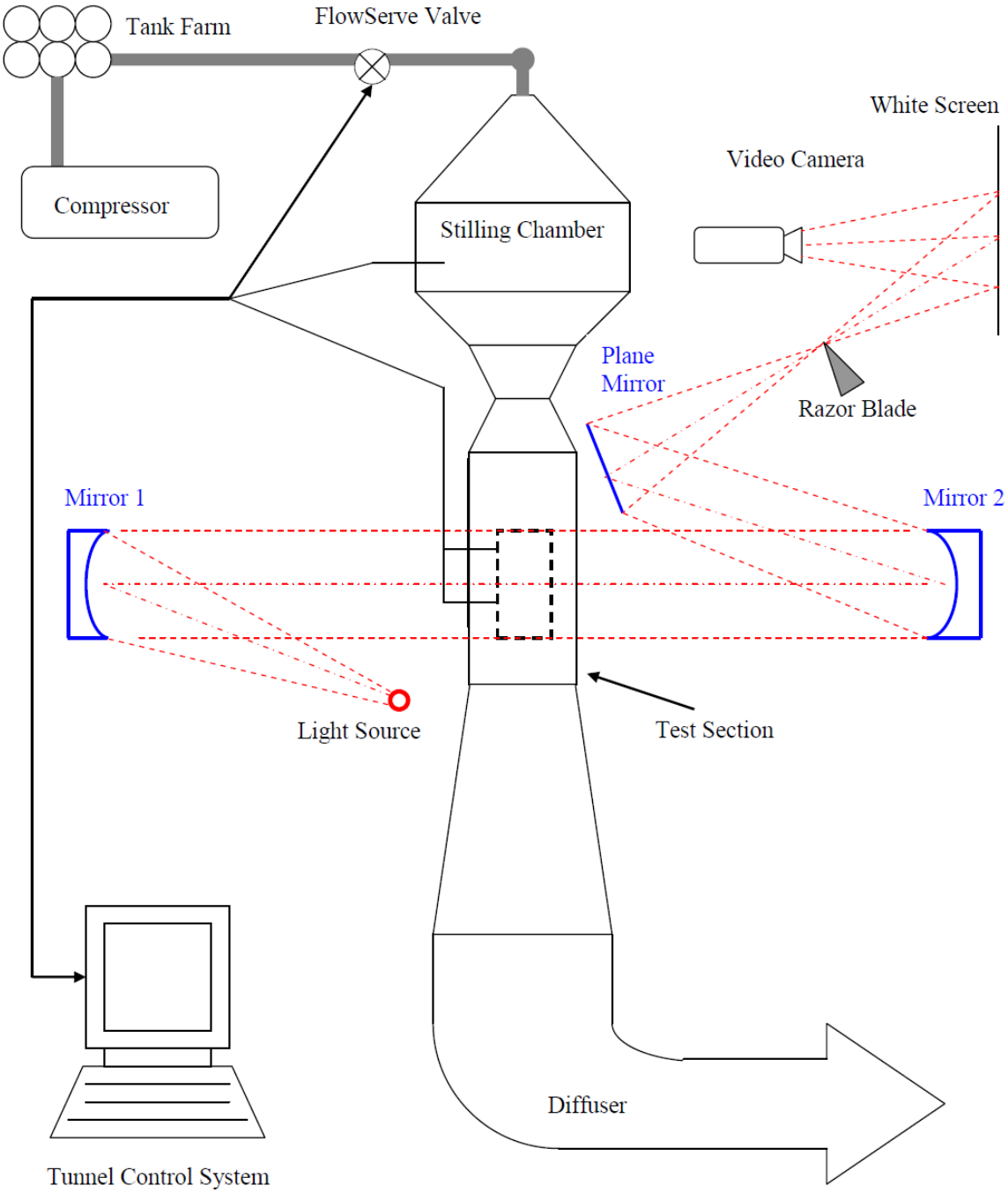

Figure 28. Sketch of HSWT with Schlieren Setup

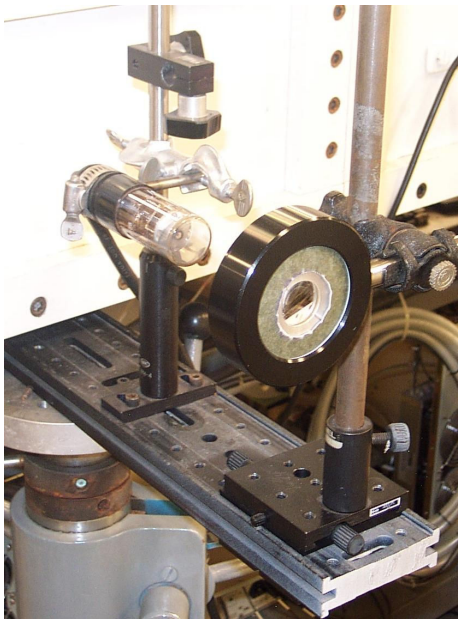

Figure 29. Schlieren Light Source with Lens

Figure 30. Schlieren Spherical Concave Mirror

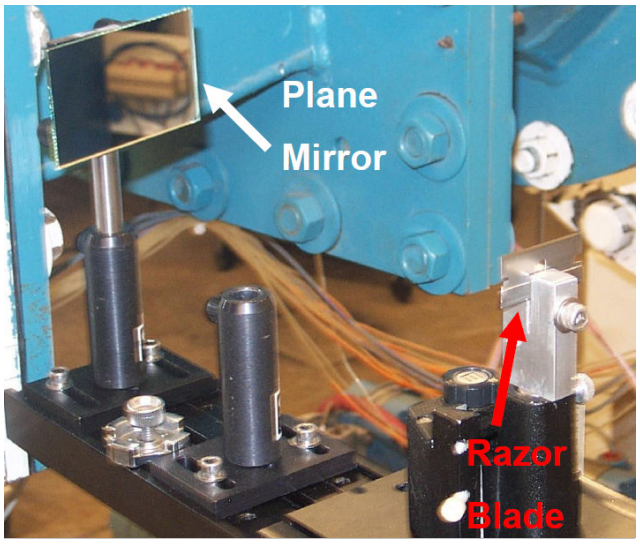

Figure 31. Schlieren Plane Mirror with Razor Blade

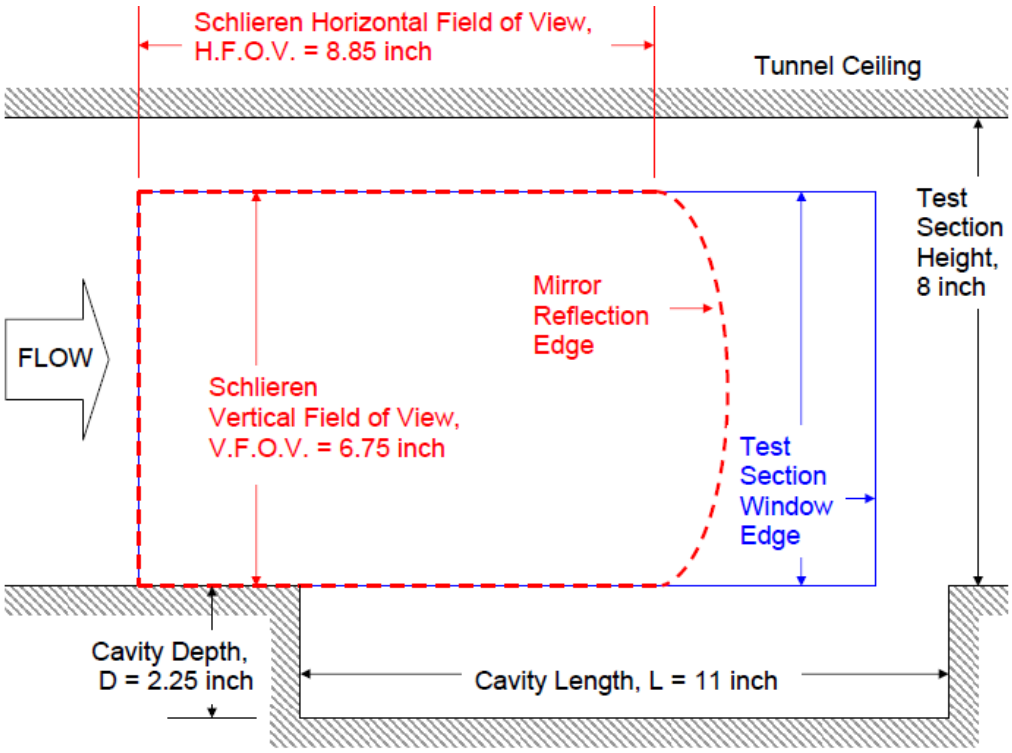

Figure 32. Sketch of Schlieren Setup Field of View

Particle Image Velocimetry Technique

Particle Image Velocimetry (PIV) is a relatively non-intrusive method of flow field visualization. PIV is used to obtain instantaneous velocity measurements for calculation of flow quantities such as vorticity and strain rates. The technique involves the upstream "seeding" of a flow field with micron-sized particles to be atomized prior to reaching the region of interest. The seeded flow field is illuminated by a planer laser sheet at the region of interest. Two lasers are sequenced with a camera for the purpose of recording two images separated by a short time delay. The two recorded images are cross correlated to enable calculation of local velocity vectors over the region of interest. Although the concept of PIV is relatively straightforward, it is set-up intensive because of its many available user selectable options.

The HSWT is configured with the TSI LASERPULSE PIV system for which a sketch of the general setup is depicted within Figure 33. Table 3 provides a detailed summary of its related components.

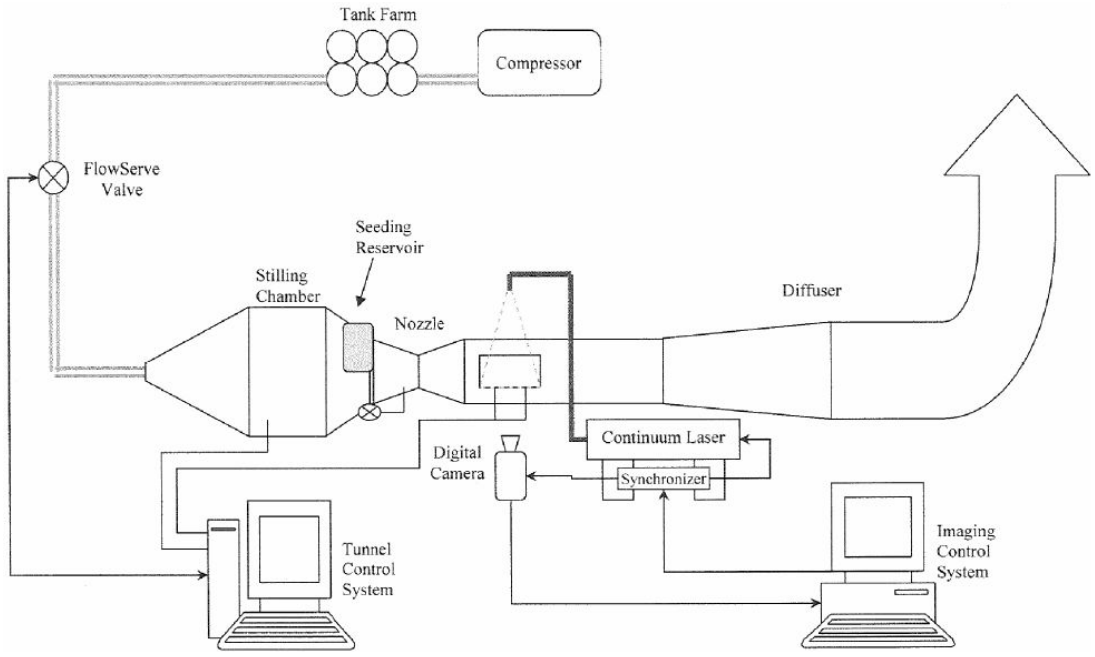

Figure 33. Sketch of HSWT with PIV System (from Loewen [5])

Table 3: TSI LASERPULSE Imaging System Summary of Components (from Loewen [5])

Component	Model #	Description
Continuum SureLite Nd:YAG Laser [*neodymium-doped yttrium aluminum garnet*]	Y200-C	Double Pulse, 532 nm Wavelength (Green Light), 200 mJ/Pulse
Articulating Laser Light Arm	6100015	Delivers beam and laser light sheet to test section.
Synchronizer	610032	Master Timing Control Device
PIVCAM 10-30 [*Digital Camera*]	630046	CCD Camera with 28mm F/2.8 Nikkor Lens, capable of 30 frames/sec
INSIGHT PIV Software	Version 3.2	PIV System setup, Image capture and analysis software [*configured on imaging control system computer*]

The upstream seeding of particles includes a yellow dye composed of fluorescent disodium salt mixed with isopropyl alcohol and water (70% isopropyl alcohol and 30% water). The exterior of the converging/diverging nozzle is configured with a tank which provides a reservoir for the yellow dye seeding mixture. Tubing connects the external tank to a 1/8 inch spray-bar located at the bottom of the converging/diverging nozzle for the injection of seed within the HSWT. A low pressure air hose is attached to the reservoir tank and includes a manual valve for the purpose of pressurizing and controlling the rate of seed added to the HSWT.

The PIV system includes two Continuum Nd:YAG lasers for the generation of beams directed into the articulated laser arm. The laser arm includes a series of mirrors for the purpose of orienting the beams into the HSWT test section. The beams are directed through spherical and cylindrical lenses to form a 1 mm (0.04 inch) thick planer light sheet which has a width set to roughly 100 mm (4 inch). The laser light sheet is used to excite the seeded flow for the emission of light at the region of interest. The emitted light is captured as an image by the PIVCAM 10-30 digital camera.

The Synchronizer provides the timing and sequencing for the Continuum Nd:YAG lasers and the PIVCAM 10-30 digital camera to enable the generation of PIV frame images. Figure 34 depicts

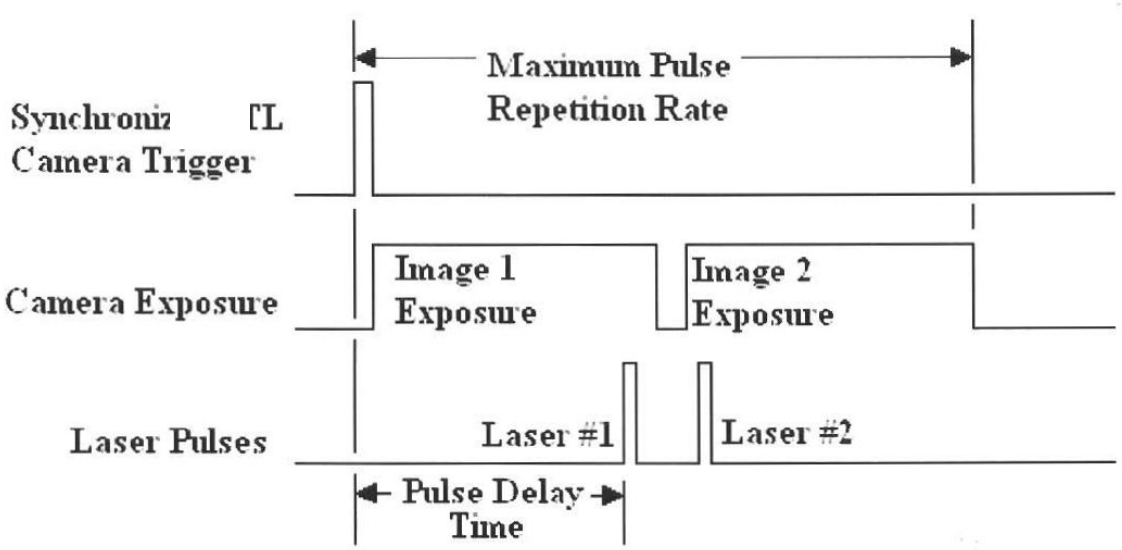

Figure 34. Frame Straddling Technique

the "frame straddling" technique used to capture two consecutive images via two separate laser pulses. The technique requires for the first laser pulse to occur within the first camera exposure time slot and for the second laser pulse to occur within the second camera exposure time slot. The time between the two laser pulses is known as the pulse separation time, Δt. The Δt value may be varied by the user to as low as 0.5 microsecond (μs). The two images collected are often referred to as an "image pair" collected over the separation time, Δt.

The INSIGHT PIV Software includes an interface for user options related to the laser and camera. INSIGHT performs cross correlation for each "image pair" to determine the x and y distances, Δx and Δy the particles travel over the separation time, Δt. Cross correlation requires the division of each region into smaller interrogation regions through the user selected "spot size". The "spot size" represents the number of horizontal and vertical pixels in an interrogation region with a one to one aspect ratio. The INSIGHT software includes three spots sizes which include 32, 64 and 128 pixels. To acquire strong cross correlation between two paired images, the "spot size" is typically selected to be at least four times larger than the anticipated displacement the seeded particles will travel within the separation time, Δt. The

selection of "spot size" and the separation time require establishing the field of view for the PIV data and a prediction of average flow speed within the region of interest.

The PIV setup did not include the entire flow field across the test cavity (or the solid floor plate when applicable). In addition, the PIV setup was constrained by the width of the planer laser sheet and the test section window size. Figure 35 depicts the field of view provided by PIV setup. The 4.0 inch horizontal field of view (HFOV) was positioned to show roughly 0.5 inch of tunnel floor upstream of the cavity and 3.5 inch of length along the cavity. This resulted in the flow structure above the cavity trailing edge not being visible. With the limitations of the field of view considered, the PIV was set up primarily to view shear layer properties at the cavity leading edge and to view the influence of each leading edge device.

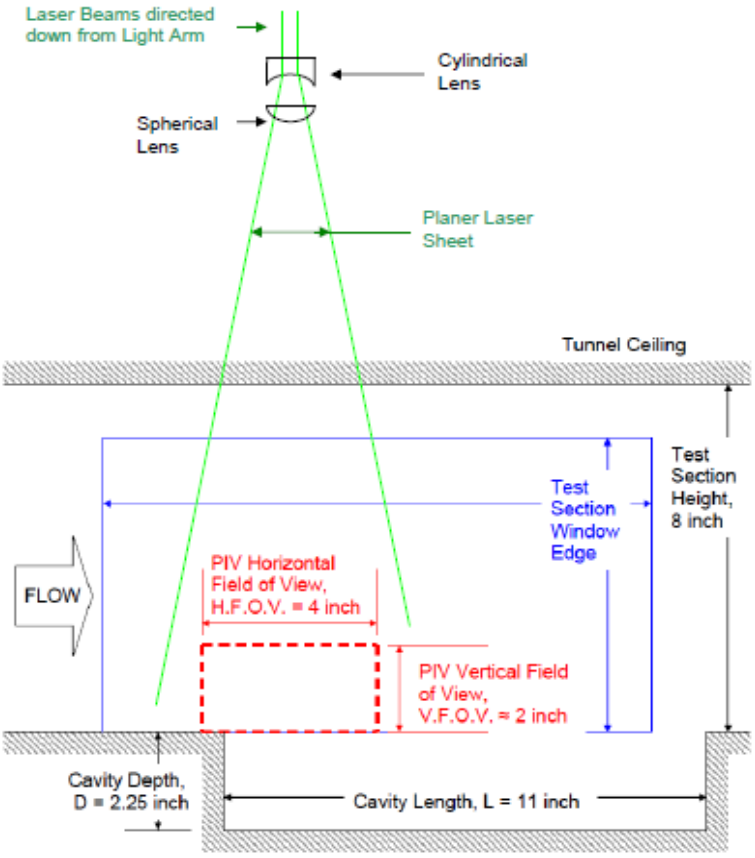

Figure 35. Sketch of PIV Setup Field of View

After selecting the field of view, the PIV was calibrated in terms of μm/pixel by using the INSIGHT velocity calibration setup window which included:

1. Placing a ruler within the test section as shown by Figure 36,

2. Manually entering a known distance shown on the ruler in terms of mm (101.6 mm for the 4 inches shown by the ruler),

3. Clicking the "Measure" button, and then

4. Placing the cursor on one side of the ruler and moving it across the known distance (101.6 mm for the 4 inches shown by the ruler). As a result of the calibration, INSIGHT calculated the resolution to be 107μm/pixel.

With application of the isentropic flow equation predicted test section velocity of 490 m/s and the PIV resolution of 107μm/pixel, the selection of "spot size" and the separation time, Δt were selected as shown within Table 4.

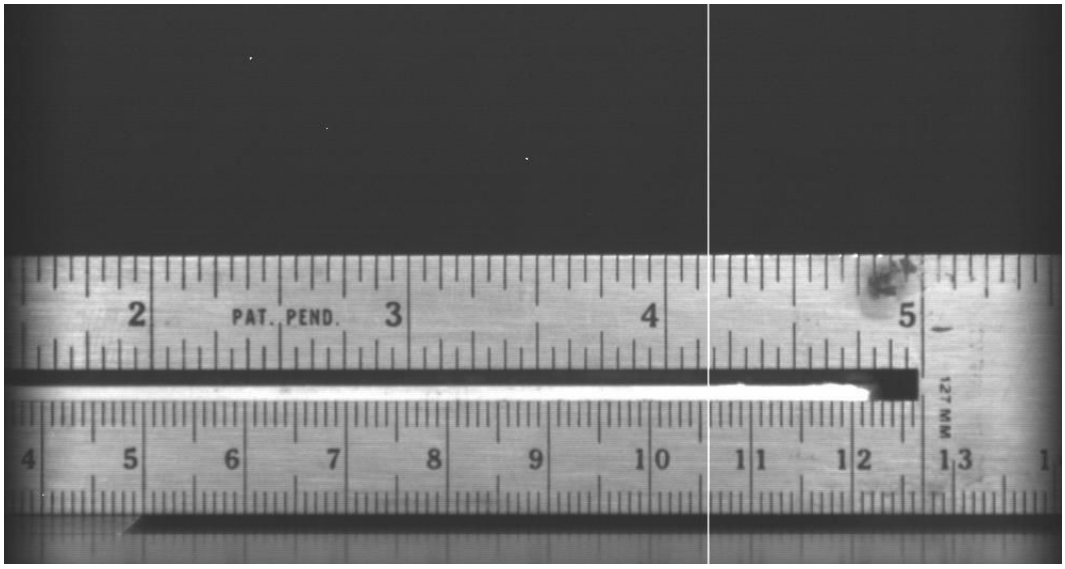

Figure 36. PIV Calibration Using Ruler within Field of View

Table 4: PIV Selection of Separation Time and Spot Size

Calibration Resolution	Freestream Velocity	Separation Time		Calculated Displacement			Desired Spot Size	Select Spot Size
Calculated through INSIGHT Procedure	U *Predicted from Isentropic Flow*	Δt *Selected within INSIGHT*		Δx *Calculated* $\Delta x = U * \Delta t$			*Minimum Spot Size Should be* $\geq \Delta x \times 4$	*Available Selection within INSIGHT*
mm / pixel	m/s	μs	s	m	mm	pixel	pixel	pixel
107	490	5	5E-6	2.45E-3	2.45E+3	22.9	91.6	128
107	490	2	2E-6	9.80E-4	9.80E+2	9.16	36.7	64
107	490	1	1E-6	4.90E-4	4.90E+2	4.59	18.3	32

The preliminary PIV testing included the testing three combinations of "spot size" and separation time, Δt which included:

1. $\Delta t = 5\mu s$ with spot size = 128 pixel: This setup included strong cross correlation. Unfortunately due to the large spot size, it could not provide adequate variation between velocity vectors.

2. $\Delta t = 2\mu s$ with spot size = 64 pixel: This setup generally provided the best trade off between strong correlation and relatively reasonable variation between velocity vectors.

3. $\Delta t = 1\mu s$ with spot size = 32 pixel: This setup often led to high quantities of spurious vectors (unexpected velocity vectors likely computed from weak cross correlation).

The majority of tests were carried out with $\Delta t = 2\mu s$ and spot size = 64 pixel. Other PIV settings determined through preliminary testing included the selection of a camera aperture setting of F8.0 and the variation of the laser intensities for the purpose of avoiding image over

exposure. Each test typically included collecting 50 "image pairs" at a frequency of 10 Hz for the purpose of achieving flow averages.

PIV Post Processing

Once INSIGHT is used to perform cross-correlation between image pairs for velocity vector calculations, INSIGHT is applied further for post-processing. The process known as "vector validation" refers to the removal of outlier data using global range, local mean, and data smoothing filters. Outlier data typically includes spurious vectors resulting from isolated examples of poor cross-correlation and inoperative camera pixels. Another feature of "vector validation" is the ability to post process multiple velocity vector files for the purpose of acquiring averaged velocity vector files. This is a powerful feature for enabling the study of both time averaged and transient flow field properties.

Finalized velocity vector files are exported from INSIGHT for the purposes of being imported into Tecplot software. Tecplot may be used to display a vector field in terms of arrows or it may used for further applications such as vorticity calculations and the generation of contour plots. Tecplot contour plots are of particular value for the study of cavity flow because they aid in the visual identification of both wall bounded and cavity spanning shear layers.

The Tecplot macro file calculates vorticity as shown by Equation (9):

$$\omega = \frac{\left(\frac{\partial v}{\partial x}\right) - \left(\frac{\partial u}{\partial y}\right)}{2} \qquad (9)$$

Where ω is vorticity, $\frac{\partial v}{\partial x}$ is the partial derivative of the local y-component velocity with respect to x and $\frac{\partial u}{\partial y}$ is the partial derivative of the local x-component velocity with respect to y. The factor of 2 within the denominator is included to account for the spatial geometry of the vector file grid setup. Loewen [5], Radhakrishnan [7] and Meganathan [20] all completed cavity flow

analysis with Tecplot through the application of non-dimensional vorticity. Non-dimensional vorticity is represented by Equation (10):

$$\widetilde{\omega} = \frac{\omega D}{U} \tag{10}$$

Where $\widetilde{\omega}$ is non-dimensional vorticity, ω is vorticity as calculated with Tecplot via Equation (9), D is cavity depth, and U is the freestream velocity within the test section. Non-dimensional vorticity is of value for providing ease of comparison between different configuration results.

Loewen [5], Radhakrishnan [7] and Meganathan [20] also applied normalized velocity for their cavity flow studies. Normalized velocity may be calculated by Equation (11):

$$\widetilde{u} = \frac{u}{U} \tag{11}$$

Where $\widetilde{u}$ is normalized local velocity, u is local velocity and U is the freestream velocity within the test section. Both non-dimensional quantities for vorticity and velocity were applied within the contour plots of this cavity flow study.

Cavity Model

The model used for the study was selected for the purpose to provide open cavity flow resonant tones which are typical for cavities of a length to depth ratio, L/D of less than or equal to 10 as described by Plentovich, Stallings, and Tracy [3]. The selected L/D of 4.88 (or slightly larger) may also be used to represent future aircraft with relatively deep weapons bays for the inclusion of various large and small geometry stores.

After the cavity flow research completed by Loewen [5] in 2008, the HSWT test section floor was modified to enable the inclusion of larger size cavities. Previous cavity flow studies

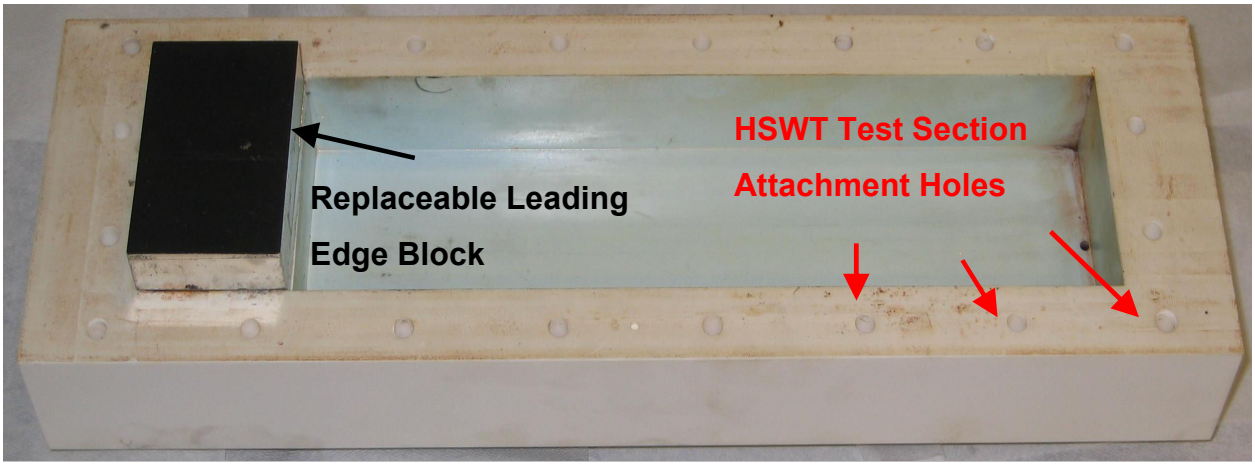

Figure 37. Cavity Model with Replaceable Leading Edge Block

completed at UTSI were typically limited to models of less than 2 inch width and 5 inch length. The current cavity model depicted within Figure 37 was designed to make full use of the HSWT modifications and is 11.00 inch length, 2.25 inch depth and 3.00 inch width. The model was constructed from plastic to fit under the sill of the HSWT test section. It also includes a removable leading edge block for the purposes of enabling easy reconfiguration of various flow control leading edge devices. It must be noted that the 2.25 inch cavity depth includes the summation of the 0.75 inch test section floor sill combined with the 1.50 inch plastic model depth. The black leading edge block is designed to be flush with the test section floor surface.

The resonant tone frequencies of the cavity model were predicted using the modified Rossiter Equation (3). This included using the isentropic flow predicted freestream velocity of 490 m/s for the HSWT operating at a Mach number of 1.84 with a ratio of specific heats, $\gamma = 1.4$ for dry air. In addition, the Rossiter derived phase delay of $n = 0.25$ and the convective to freestream ratio of $K_v = 0.57$ for a $L/D = 4$ cavity were applied. The calculation was calculated in metric units with the 11.00 inch cavity length set to 0.279 meter. The resonant tone frequencies presented within Table 5 represent the baseline cavity only configuration (without any leading edge devices).

Table 5: Predicted Resonant Tone Frequencies with Modified Rossiter Equation

Rossiter Mode, m	Cavity Strouhal number, $S=(m-n)\left\{M\left[1+\frac{(\gamma-1)}{2}M^2\right]^{-1/2}+\frac{1}{K_v}\right\}^{-1}$	Cavity Resonant Tone Frequencies, $f=S\frac{U}{L}$
-	-	Hz
1	0.236	414
2	0.551	967
3	0.866	1519
4	1.181	2071

Determination of Rod Dimensions and Location

In the last decade, the "rod in crossflow" technique as illustrated earlier within Figure 7 has likely received the most dedicated research of all methods of cavity flow control. Several papers to provide guidelines regarding the optimum cylinder dimensions and position for use with the "rod in crossflow" technique include:

1. Stanek, Ross, Odera and Peto [18] recommended sizing the rod diameter, d and positioning the rod centerline to have height, h both equal to two thirds of the boundary layer thickness, δ upstream of the cavity leading edge. They also recommend using semi-circular side plates for supersonic flow applications and using a modified cylinder Strouhal number, St = 0.165 for estimating the vortex shedding frequency as a result of having the rod positioned within a boundary layer.

2. Smith et al [21] recommended sizing the rod diameter, d to be somewhere between 30 to 40% the boundary layer thickness, δ upstream of the cavity

leading edge. They also recommended for the rod to be positioned near the outer edge of the upstream boundary layer at the cavity leading edge.

The cavity flow research completed by Loewen [5] at UTSI with the HSWT included applying the rod in crossflow technique where the lower half of the rod was positioned within the boundary layer and the upper half was positioned within the freestream flow. This was equivalent to having the rod centerline positioned at the boundary layer thickness, δ upstream of the cavity leading edge. In the case of Loewen's testing, the measured boundary layer thickness was between 11 to 12 mm for a test section Mach number of M = 0.55. As a result, Loewen selected a rod height of h = 11.9 mm (15/32 inch). Of the three rod diameters tested by Loewen, it was the 1/4 inch rod that produced the best suppression of tones.

Contracted flow research completed within the UTSI HSWT has shown through Schlieren Photography that the boundary layer within the test section may be somewhere between 8 to 11 mm for a test section Mach number of M = 1.84. As the boundary layer thickness was not anticipated to drastically change between the Mach numbers of 0.55 and 1.84, the current study "rod in crossflow" model thus included the dimensions selected by Loewen. Therefore the rod diameter, d was set to 1/4 inch (6.35 mm) and the a rod height, h was set to 15/32 inch (11.9 mm). This selection was also made in case there would have been an opportunity to test the present cavity model at a subsonic flow condition.

Based on the recommendations of Stanek, Ross, Odera and Peto [18], the rod was supported between two semi-circular side plates for the provision of improved vortex shedding within a supersonic flow. Figure 38 provides a photograph of the side plates attached to the modified leading edge block for use with both the solid floor and cavity configurations. The side plates were made from 1/8 inch aluminium sheets which were bevelled on their exterior sides (sides not supporting the rod). The bevelled edges were included with the intent of having side plate related oblique shock waves forming outward and to avoid influence on both the rod and cavity flow fields.

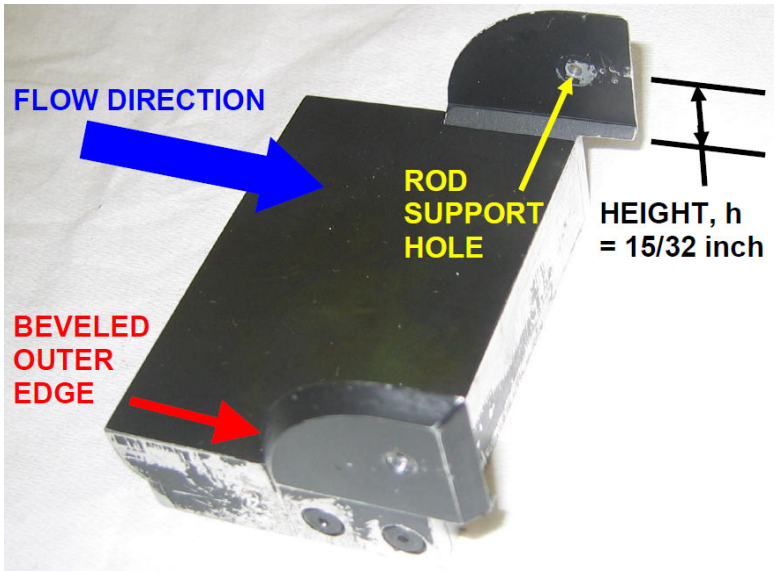

Figure 38. Side Plates Attached to Modified Leading Edge Block

The Reynolds number, $\mathrm{Re}_d = \frac{\rho U d}{\mu}$ for the rod in crossflow was approximated to be 1.5 x 10^5 by using:

1. the isentropic flow predicted freestream velocity, U = 1600 ft/s (490 m/s),

2. the rod diameter of 1/4 inch (6.35 mm),

3. the equation of state calculated density, $\rho = 1.23*10^{-3}$ lb*s^2/ft^4 (0.653 kg/m^3), and

4. the power law approximated dynamic viscosity ($\mu = C\sqrt{T}$) result of

$$\mu = 3.58\times10^{-7}\frac{lb\cdot s}{ft^2} = 1.71\times10^{-5}\frac{N\cdot s}{m^2}.$$

Figure 39 from White [22] shows the relationship between vortex shedding cylinder Strouhal number with Reynolds number. For Reynolds numbers from 100 to 10^5, the Strouhal number is approximately 0.2.

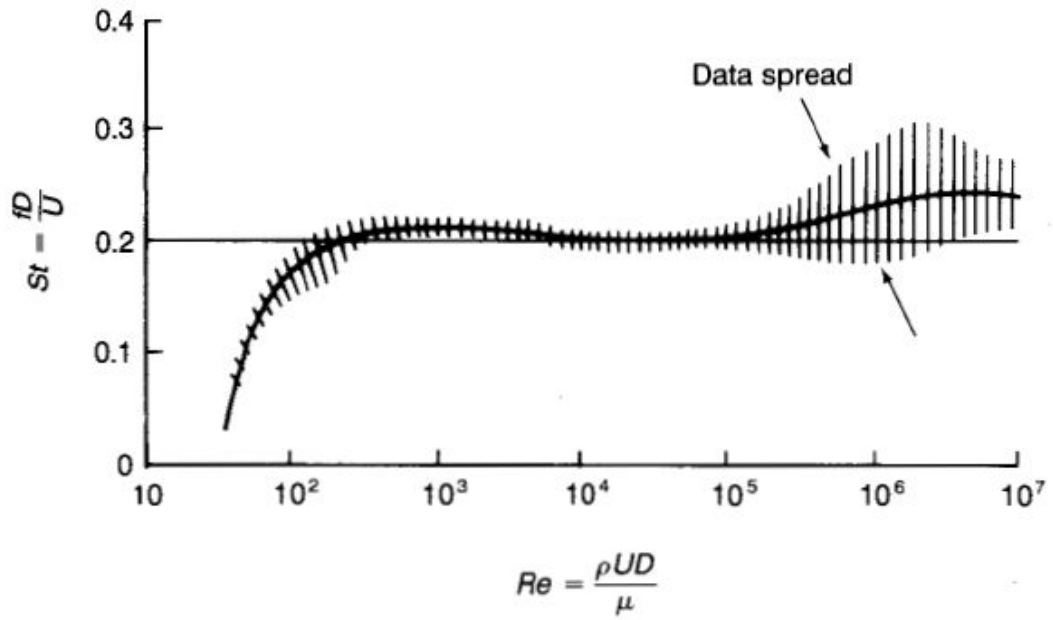

Figure 39. Measured Strouhal number versus Reynolds number for Vortex Shedding Behind a Circular Cylinder (from White [22])

From the Figure 37 plot, it was anticipated that the Strouhal number could vary from 0.2 since the estimated Reynolds number of 1.5×10^5 was within the domain of possible data spread. Stanek, Ross, Odera and Peto [18] also recommend using a modified cylinder Strouhal number, St = 0.165 for estimating the vortex shedding frequency as a result of having the rod positioned within a boundary layer. Based on these considerations, Table 6 was used to predict a frequency range from 12700 Hz to 15300 Hz for where to anticipate the actual vortex shedding frequency to actual occur for the "rod in crossflow" cavity flow control technique.

As advocated by Stanek et al [18], the "rod in crossflow" cavity flow control technique is effective because it produces a high frequency forcing through vortex shedding.
This means the rod vortex shedding frequency should be outside of the range of the cavity resonant tones. The predicted frequency range from 12700 Hz to 15300 Hz satisfies this criterion since the cavity resonant tone frequencies predicted by the modified Rossiter equation in Table 5 are much lower (414 Hz, 967 Hz, 1519 Hz and 2071 Hz).

Table 6: Predicted Rod in Crossflow Vortex Shedding Frequencies

Source	Vortex Shedding Strouhal number, St	Vortex Shedding Frequencies, $f = St\frac{U}{d}$
	-	Hz
Figure 37 (from White [22])	0.2	15300
Stanek, Ross, Odera and Peto [18]	0165	12700

Determination of Airfoil Dimensions and Location

With the exception of the water tunnel testing completed by Franke and Carr [19] in 1975, there appears to be very little available guidance for using the "airfoil in crossflow" cavity flow control technique sketched earlier within Figure 7. The "airfoil in crossflow" technique was selected to determine if it could provide a lofting or thickening effect on the cavity spanning shear layer. If the "airfoil in crossflow" could be used to provide adequate cavity flow control with strong noise suppression characteristics, it would potentially provide an alternate method to the high frequency forcing or flow blockage methods.

Airfoil Selection criteria included:

1. Both the "airfoil in crossflow" and "rod in crossflow" leading edge devices needed to be located at the same location within the boundary layer above the cavity leading edge for comparison between the cavity flow control techniques

2. Both the "airfoil in crossflow" and "rod in crossflow" leading edge devices needed to be interchangeable within the side plates to enable ease of configuration changes between tests.

3. The airfoil was to be tested at three angles of attack including 0, -5 and -10 degrees. These angles were selected to determine at what angle the airfoil may experience flow separation and to determine which angle provided the best cavity noise suppression.

4. The "airfoil in crossflow" was to include a smaller projected thickness than the "rod in crossflow" technique. This criterion was selected with the intent of avoiding interpretation of the "airfoil in crossflow" being purely deemed a variation of the vertical spoiler / flow blockage technique.

5. The airfoil needed to be built within a tolerance of 1/32 inch to ensure it could be properly mounted within the side plates.

6. The airfoil needed to have enough structural strength to experience minimal deflections within a Mach 1.84 crossflow.

7. The airfoil was selected to have a maximum chord length of 1/2 inch to ensure it would remain relatively small in size in comparison to the cavity geometry of 2.25 inch depth and 11 inch length.

The manufacturing of an airfoil to such a small scale led to many challenges. Originally, it was desired for the airfoil to be constructed from 1/16 inch steal for the purposes of avoiding flow separation at higher magnitude angles of attack. Unfortunately, the thin airfoil option was abandoned in favour of a more thick and less difficult to fabricate airfoil option which was constructed from 1/8 inch steel. With the 1/2 inch chord length, this selection included a high thickness to chord ratio, t/c of 25%. Drawings of the airfoil used are provided within Appendix 2. Figure 40 includes a sketch of the 1/4 inch rod beside the airfoil to show how their thicknesses vary with one another. Even when the airfoil is set to a -10 degree angle of attack, it still has a lesser projected thickness in comparison to the 1/4 inch rod diameter. The large hole on the airfoil is used to attach the airfoil at the same location as the rod within the side plates.

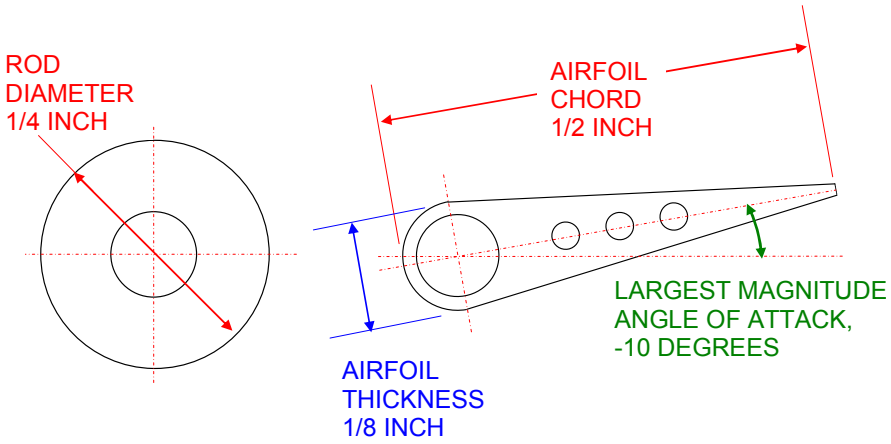

Figure 40. Cross-section Comparison Between "Rod in Crossflow" and "Airfoil in Crossflow" Leading Edge Devices

The three small holes along the airfoil trailing edge are for the placement of 1/32 inch pins for enabling various angle of attack positioning required within the side plates.

Test Configurations

This section provides photographs for each configuration previously described within Chapter 1 of this study. The test configurations include:

1. Clean Tunnel: This configuration photographed within Figure 41 was tested to determine the broadband noise and to acquire an initial assessment of the tunnel flow field characteristics. This test configuration was also for boundary layer measurements of the tunnel floor.

2. Rod Signature and Airfoil Signatures at 0, -5, -10 Angles of Attack with the Solid Floor Plate: These configurations are included within Figures 42 and 43. The leading edge devices were positioned above the leading edge of the solid floor plate and within the vicinity of the tunnel floor boundary layer. This phase was required to see the flow field structures resulting from the only the leading edge devices and without any cavity present.

3. Baseline Cavity: This configuration included the cavity only without any leading edge flow control devices as shown in Figure 44. This test was required to determine the peak resonance frequencies and the broadband noise created by the cavity. This configuration was required to gain imagery related to the cavity's flow field structure. It also provided the opportunity for the Modified Rossiter equation predicted resonant frequencies to be compared with actual empirical data.

4. Rod with Cavity and Airfoil at 0, -5, -10 Angles of Attack with Cavity: These configurations photographed within Figures 45 and 46 represent a cavity with flow control being applied. The flow control devices were positioned above the leading edge of the cavity and within the vicinity of the tunnel floor boundary layer. These configurations were required to determine the amount of acoustic suppression being provided by each leading edge device. These configurations were also for the purposes of acquiring the flow field structure of the cavity as a result of the leading edge devices.

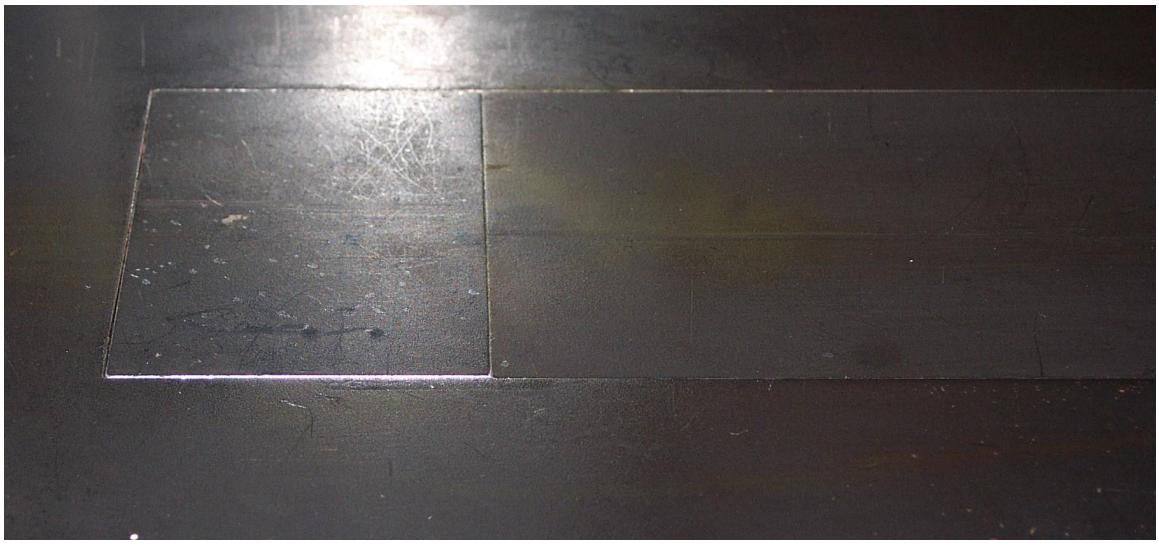

Figure 41. Test Configuration 1: Clean Tunnel - Photograph

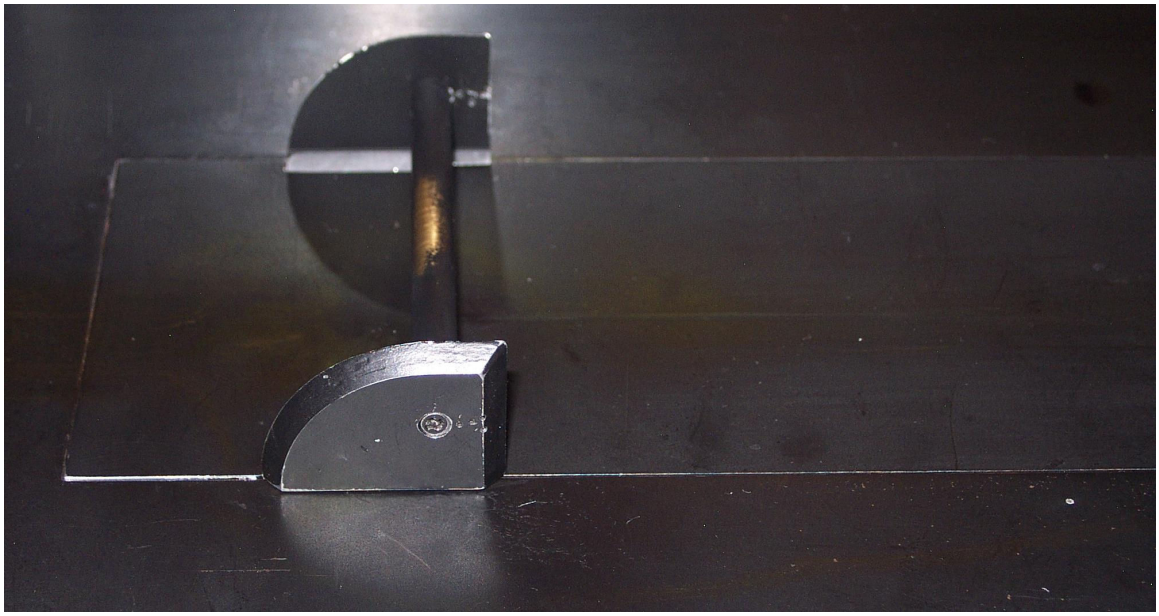

Figure 42. Test Configuration 2a: Rod Signature (Solid Floor Plate) - Photograph

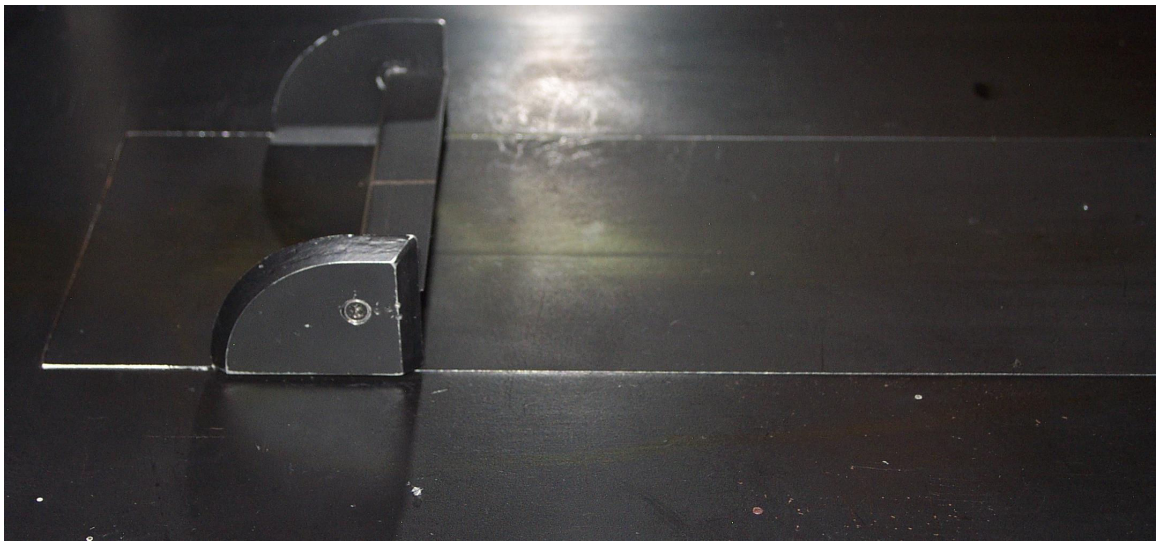

Figure 43. Test Configurations 2b, 2c and 2d: Airfoil Signatures at 0, -5, -10 Angles of Attack (Solid Floor Plate) - Photograph

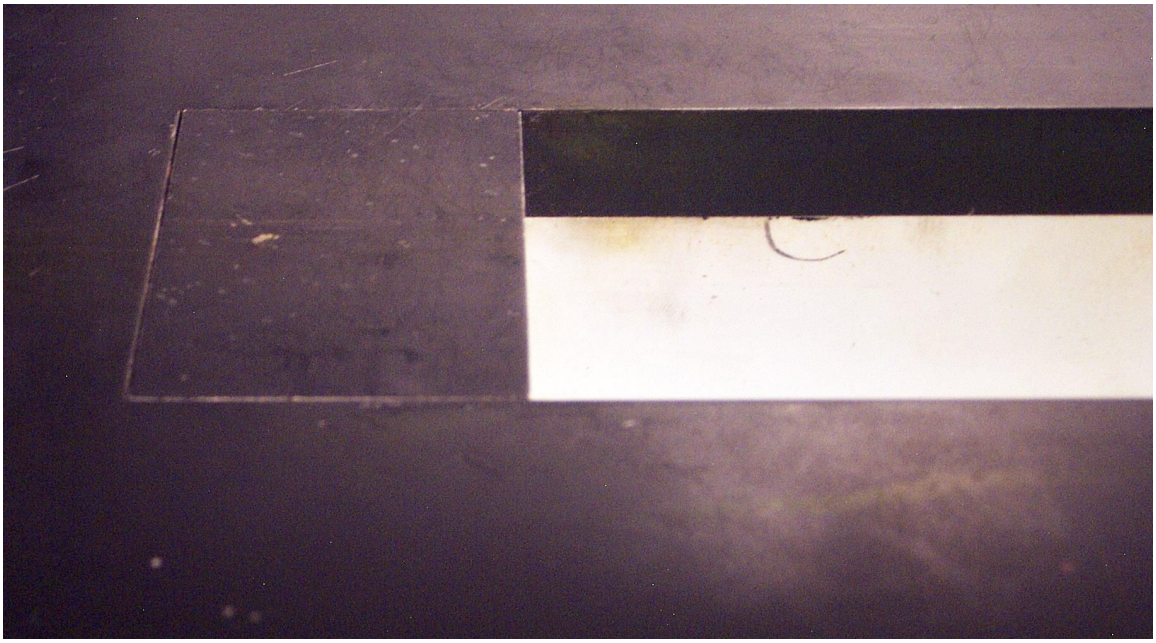

Figure 44. Test Configuration 3: Baseline Cavity - Photograph

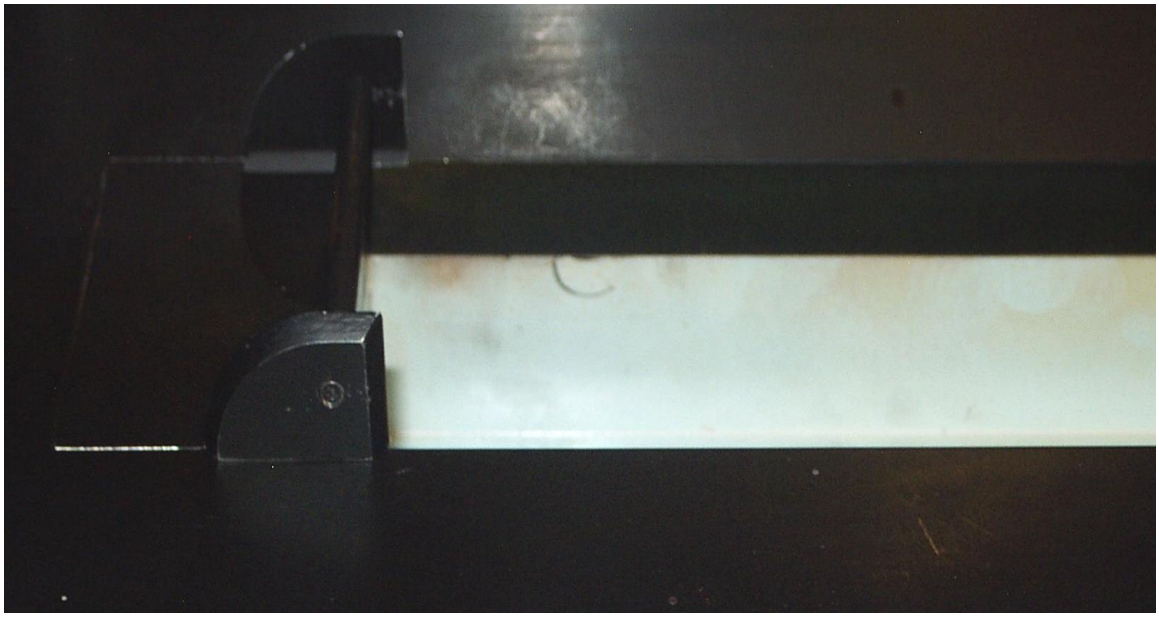

Figure 45. Test Configuration 4a: Rod with Cavity - Photograph

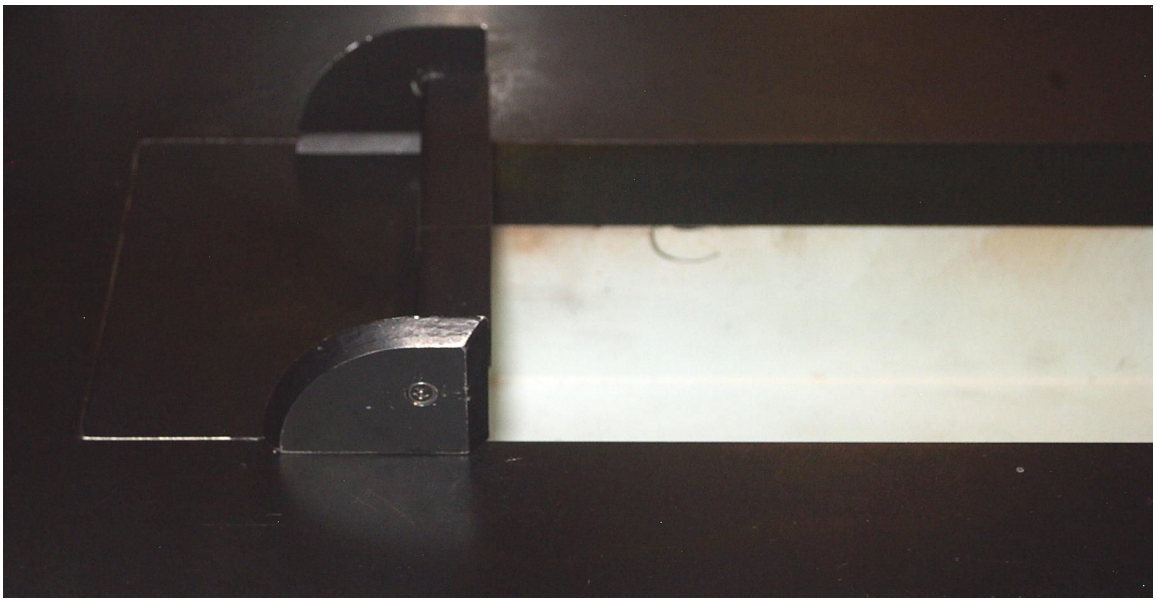

Figure 46. Test Configurations 4b, 4c and 4d: Airfoil at 0, -5, -10 Angles of Attack with Cavity – Photograph

Chapter 4

EXPERIMENTAL RESULTS AND ANALYSIS

This chapter is organized into sections for each the configurations tested. Each section generally begins with the discussion of acoustic spectrum data followed by flow visualization results from both Schlieren photography and Particle Image Velocimetry (PIV). The configurations are ordered to provide the progressive build up of test condition complexity. Therefore, all solid floor test configurations are discussed prior to the discussion of any cavity configurations. As a result of the complexity of the flow fields studied, there are several cases where supplemental test configurations were added to the test program.

Test Configuration 1: Clean Tunnel

The UTSI high speed wind tunnel with its converging diverging nozzle provided a stable flow of Mach 1.84 for all tests. Figure 47 depicts the clean tunnel acoustic spectrum which was measured to determine the broadband noise and if there were any distinguishing phenomena such as resonant tones. Over the frequency range of 0 to 5000 Hz, the broadband noise of the tunnel was measured to be 104 dB. With this relatively high broadband noise, it was anticipated that this would be an inherent feature of all other test configurations. Within the narrow frequency range of 0 to 500 Hz, the broadband noise reached approximately 120 dB. There were no resonant tones present within the clean tunnel. This was a desirable quality for the identification of tones within more complex configurations. In addition, these observations were identical for all three tests of this configuration.

Figure 48 includes an image collected from the Schlieren video footage of the clean tunnel configuration. Although the HSWT operated at the stable Mach number of 1.84, the photograph showed that the test section included a relatively complicated flow structure. The clean tunnel included numerous Mach waves that were attributed to slight imperfections within the nozzle and test section. Through measurement of the Mach wave angles, Mach numbers could be approximated as shown by Figure 49 ($M = 1/\sin\mu = 1/\sin(33°) = 1.84$). It was anticipated that

analysis of other configuration tests would be complicated by the presence of the Mach waves and that careful comparison between each different configuration Schlieren photograph would be required to determine the flow field contributions of any objects placed within the test section. As the test section window represented a 6.75 inch vertical field of view, a crude approximation for the boundary layer at the tunnel floor could be calculated from scaling the photograph as shown by Figure 49. It was noted that the observed line on the floor did not necessarily equate to the complete boundary layer thickness, δ since the line may not have represented the flow actually reaching 99% of the freestream velocity within the test section. The scaled approximation was thus interpreted as a lower limit for the boundary layer thickness. The result of the scaled measurement yielded an approximate boundary layer thickness, $\delta \approx 3/8$ inch (9.5 mm).

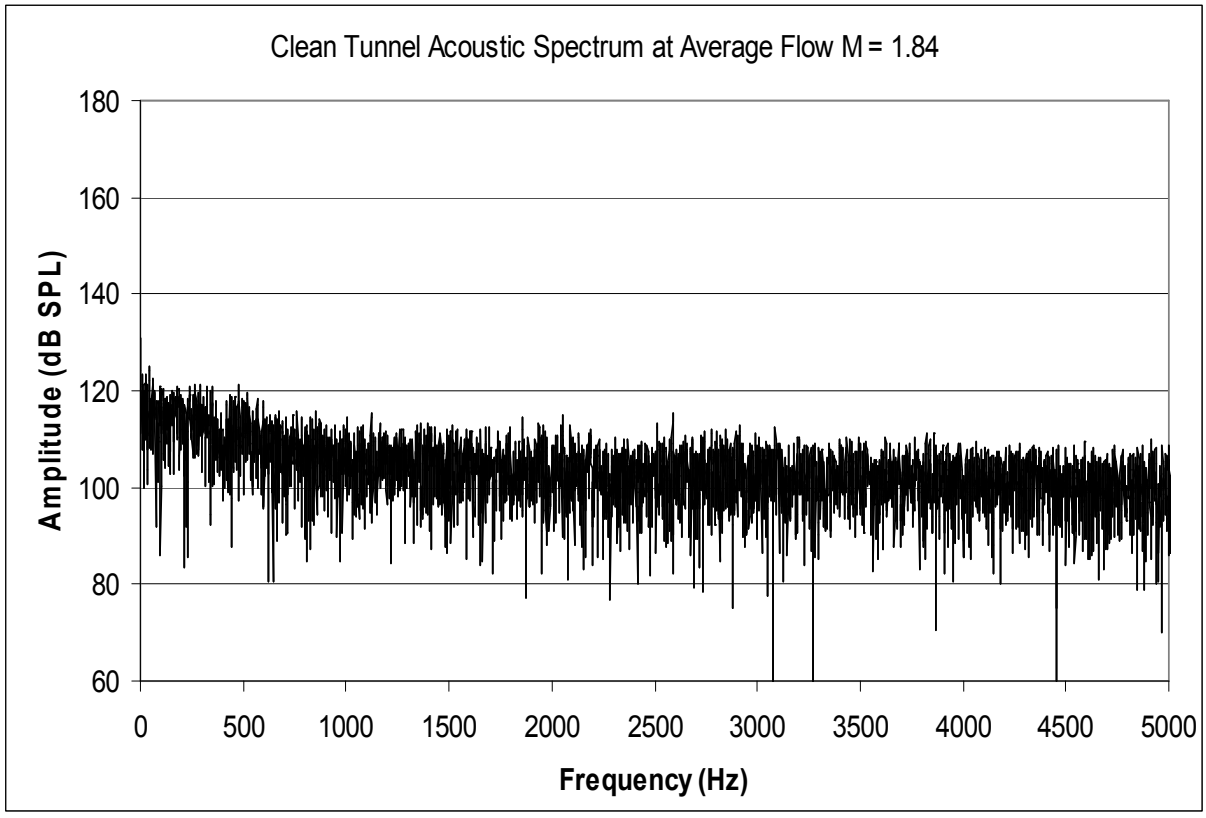

Figure 47. Test Configuration 1: Clean Tunnel – Acoustic Spectrum

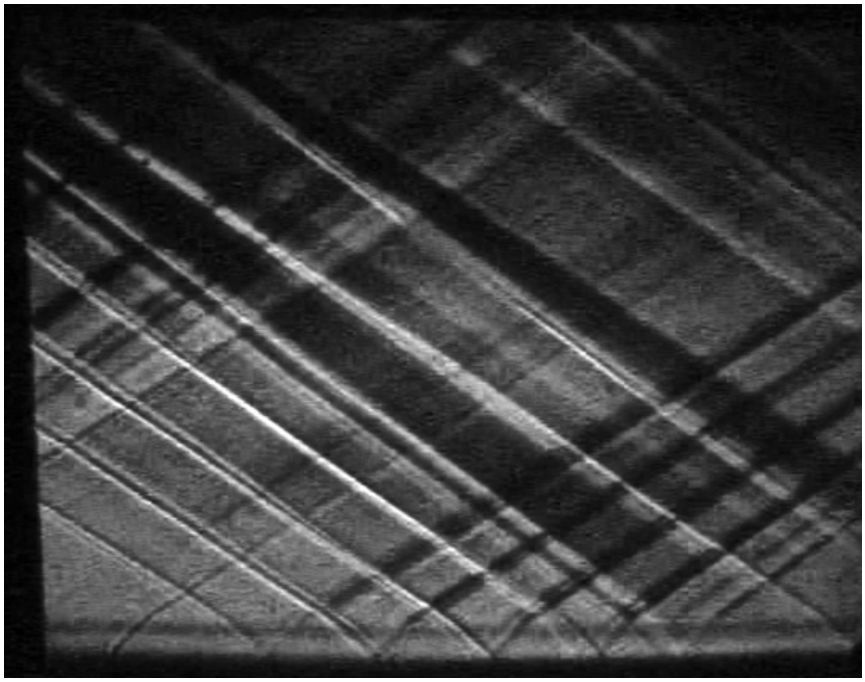

Figure 48. Test Configuration 1: Clean Tunnel – Schlieren Photograph

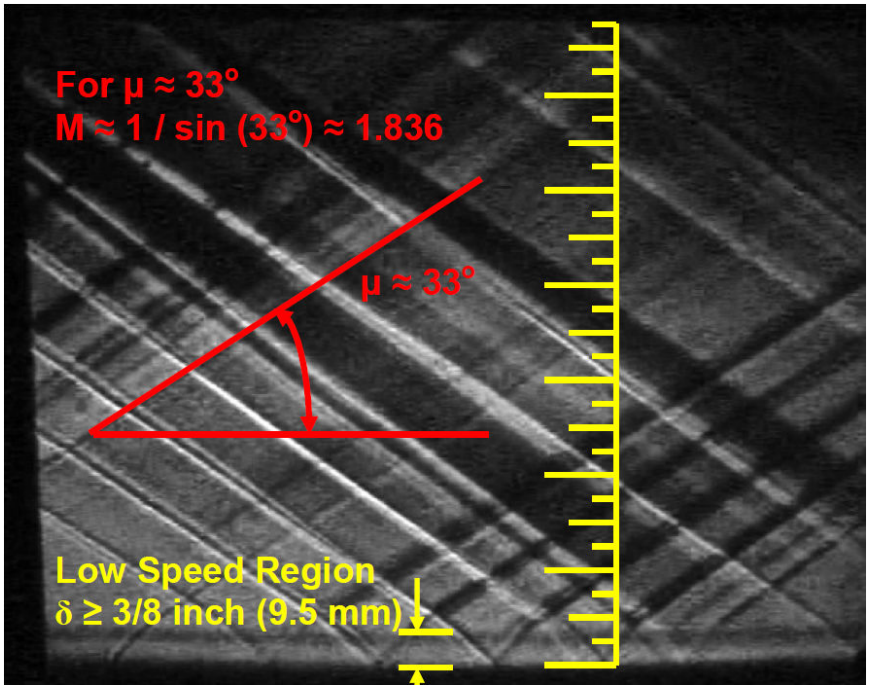

Figure 49. Test Configuration 1: Clean Tunnel – Schlieren Analysis

PIV was applied to the clean tunnel configuration for the purposes of providing an alternate measurement of the boundary layer. As the PIV was calibrated for flow moving at 1600 ft/s (490 m/s), spurious (poorly correlated) vectors occurred in some low velocity regions. Figure 50 depicts a zoomed view of vectors located within 2 mm of the tunnel solid floor surface computed by the INSIGHT PIV software. Figure 51 shows the vectors that were removed through the use of PIV range filters and Figure 52 depicts the vectors which replaced the removed vectors as a result of the INSIGHT smoothing process. It was noted from Figure 52 that the smoothing process could generate vectors which possibly violate the solid surface no-slip boundary condition. This observation caused little impact with respect to computing the boundary layer thickness because these measurements require estimating the region where the flow reaches 99% of its freestream velocity. Although the majority of velocity vectors appeared to be nearly uniform within Figure 52, all velocity vectors showed increases in velocity with respect to increases in y-displacement above the floor. Therefore, all of the vectors shown represent the boundary layer region above the test section floor.

Through PIV post processing with Tecplot software, the clean tunnel boundary layer thickness was calculated to be 11 mm as shown in Figure 53. This provided reasonable agreement with the Schlieren scaled approximate of $\delta \approx 3/8$ inch (9.5 mm). It was therefore predicted that the cavity flow control devices (rod and airfoil) would be at least partially submerged in the boundary layer as each device was to be positioned a height, h of 15/32 inch (11.9 mm) above the tunnel floor.

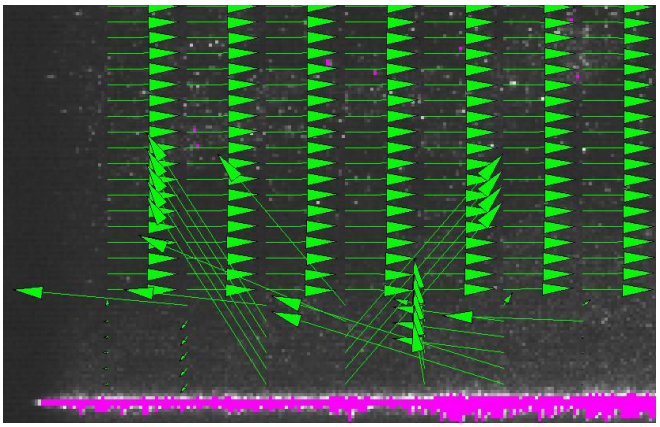

Figure 50. Test Configuration 1: Clean Tunnel – Spurious PIV Vectors at Solid Floor Surface

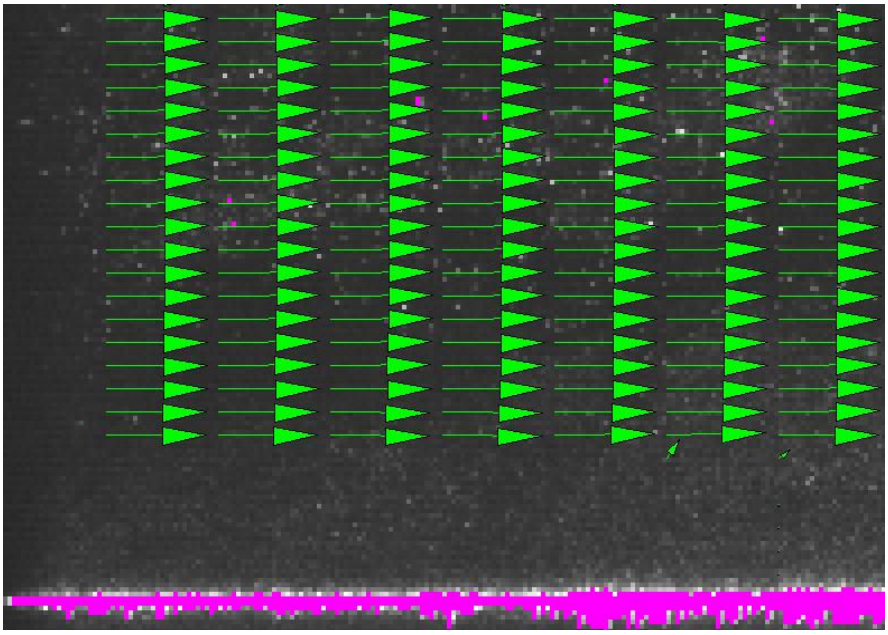

Figure 51. Test Configuration 1: Clean Tunnel – Removed Spurious PIV Vectors from Solid Floor Surface through Range Filters

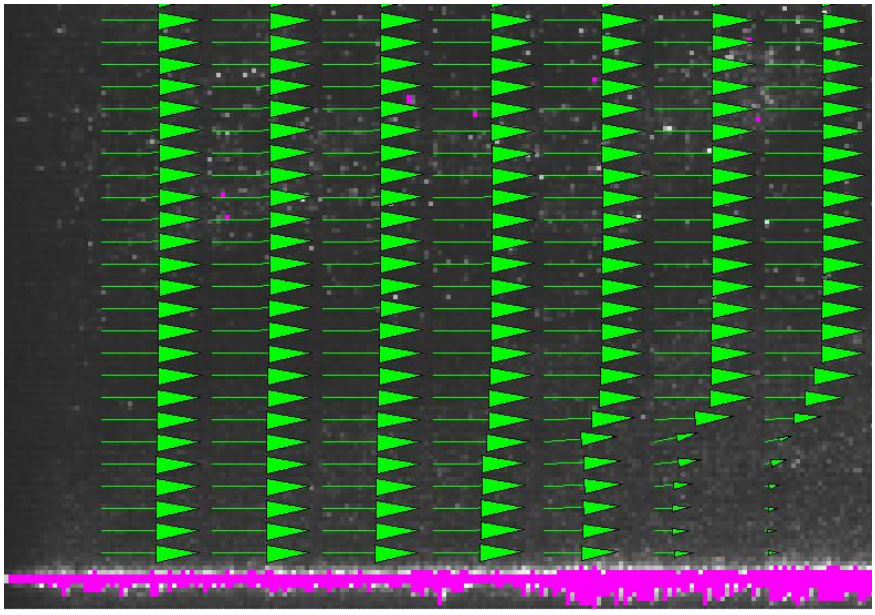

Figure 52. Test Configuration 1: Clean Tunnel – Replaced Vectors at Solid Floor through Smoothing Process

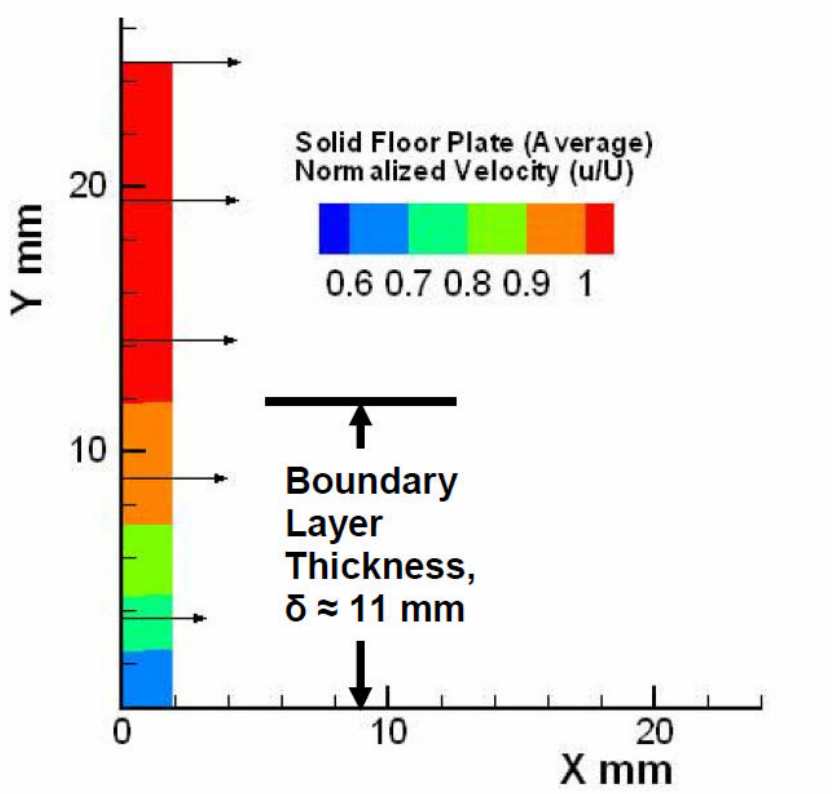

Figure 53. Test Configuration 1: Clean Tunnel – Normalized Velocity Profile for Boundary Layer from Tecplot Post Processing

Supplemental Test Configuration 1a: Side Plates Only Signature (Solid Floor Plate)

As a result of the numerous Mach waves observed within the clean tunnel through Schlieren photography, it was decided that an individual test related to the side plate only configuration would be required. As described earlier, semi-circular side plates were incorporated into the design because of the recommendation provided by Stanek, Ross, Odera and Peto [18] for the provision of improved rod vortex shedding within a supersonic flow.

From the acoustic spectrum data presented within Figure 54, the side plate only configuration was virtually identical to the clean tunnel configuration. Over the frequency range of 0 to 5000 Hz, the broadband noise of the tunnel was measured to be 103 dB which was similar to the clean tunnel was measurement of 104 dB. Within the narrow frequency range of 0 to 500 Hz, the broadband noise was roughly 120 dB which was identical to the clean tunnel configuration. The

side plates produced no significant acoustic phenomena such as resonant tones. From these observations it was deemed that the side plates produced little impact on the acoustic phenomena measured within range of the dynamic pressure transducer.

Figure 55 includes a Schlieren photograph of the side plate only solid floor configuration. The photo showed the presence of compression shock waves, Prandtl–Meyer expansions and separation regions. Figure 56 includes a flow field contribution labelled version of the Schlieren photograph. A detached compression shock was formed upstream of the lower side plate leading edge. The compression showed a bow wave shape along the side plate. The compression shock also included a three dimensional component as exhibited by the shock wave impinging the glass window surface. The side plate trailing edge included an expansion region with some evidence of flow separation. At the side plate trailing edge, a very faint horizontal line could be observed which was attributed to a tip vortex.

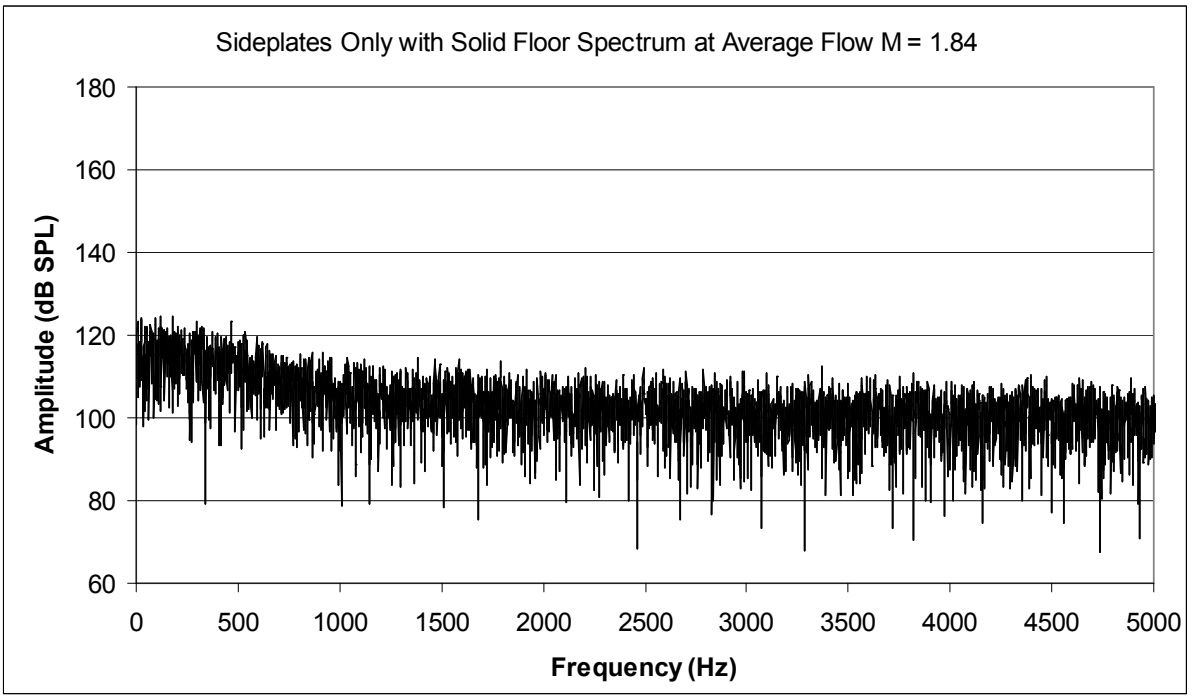

Figure 54. Supplemental Test Configuration 1a: Side Plates Only Signature (Solid Floor Plate)

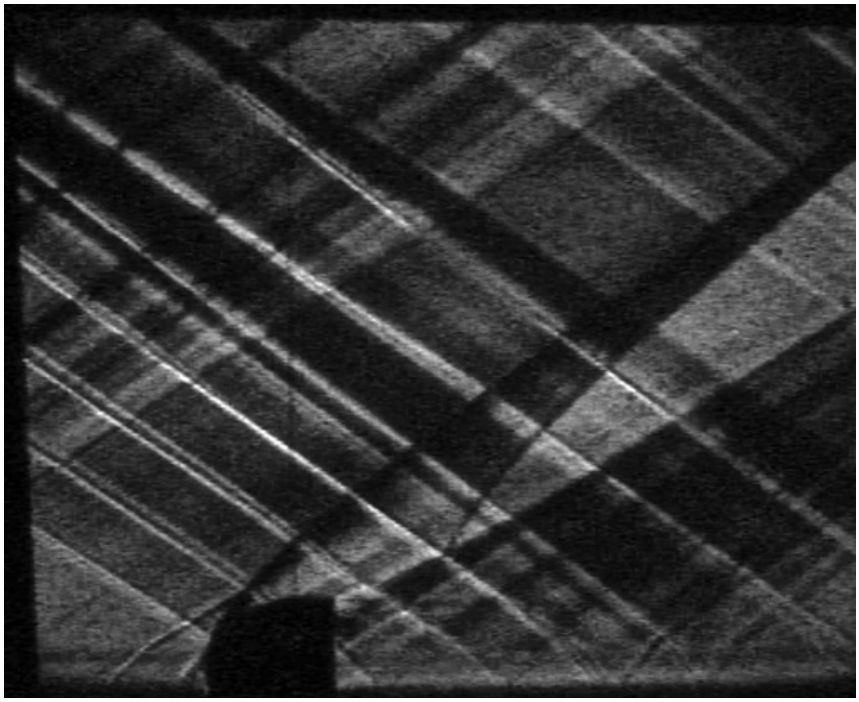

Figure 55. Test Configuration 1a: Side Plates Only with Solid Floor – Schlieren Photograph

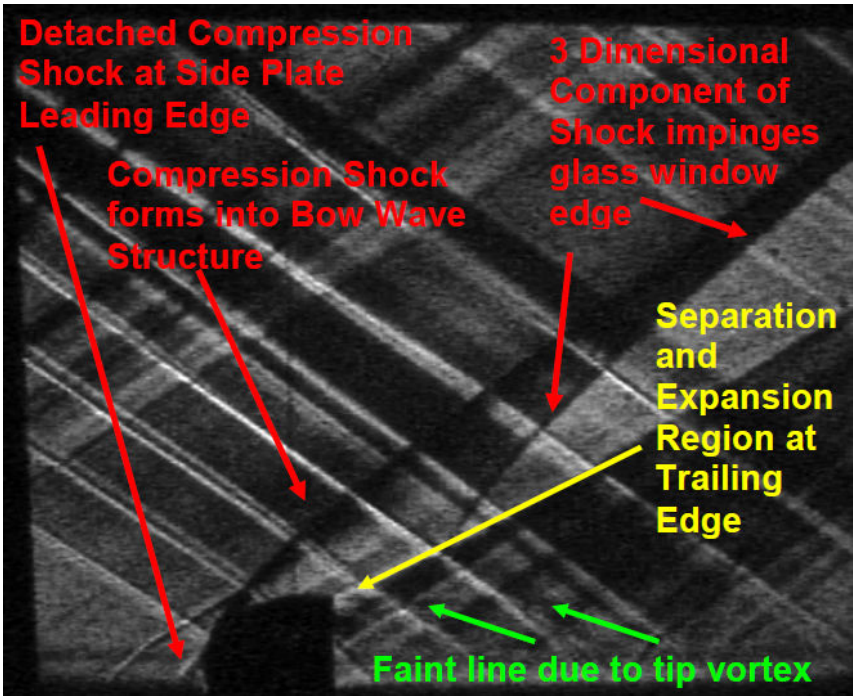

Figure 56. Test Configuration 1a: Side Plates Only with Solid Floor – Schlieren Analysis

Test Configuration 2a: Rod Signature (Solid Floor Plate)

The acoustic spectrum of the rod signature with solid floor plate configuration was measured to determine if any there were any indications of amplitude changes over the predicted frequency range of vortex shedding between 12700 Hz and 15300 Hz. Figure 57 did not show indications of amplitude changes over the frequency range between 12700 Hz and 15300 Hz. There is the possibility that the intensity of pressure fluctuations due to vortex shedding became relatively weaker downstream the test section within the Mach 1.84 flow. It is therefore possible that the dynamic pressure transducer may have been unable to measure the pressure fluctuations due to the vortex shedding only because it was located 11 inch downstream of the rod which was the equivalent of 44 rod diameters. The overall broadband noise measured within the range from 0 to 5000 Hz was 110 dB. This was higher than the 104 dB measured for the clean tunnel configuration within this frequency range.

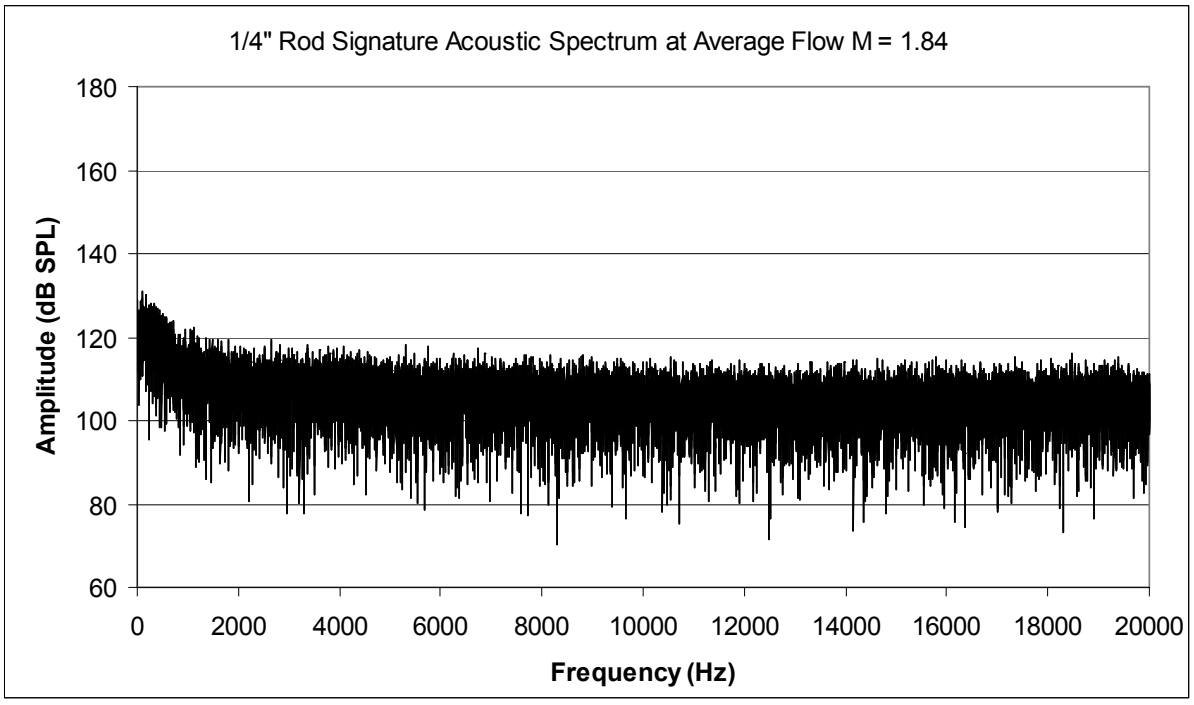

Figure 57. Test Configuration 2a: Rod Signature (Solid Floor Plate) – Acoustic Spectrum from 0 to 20000 Hz

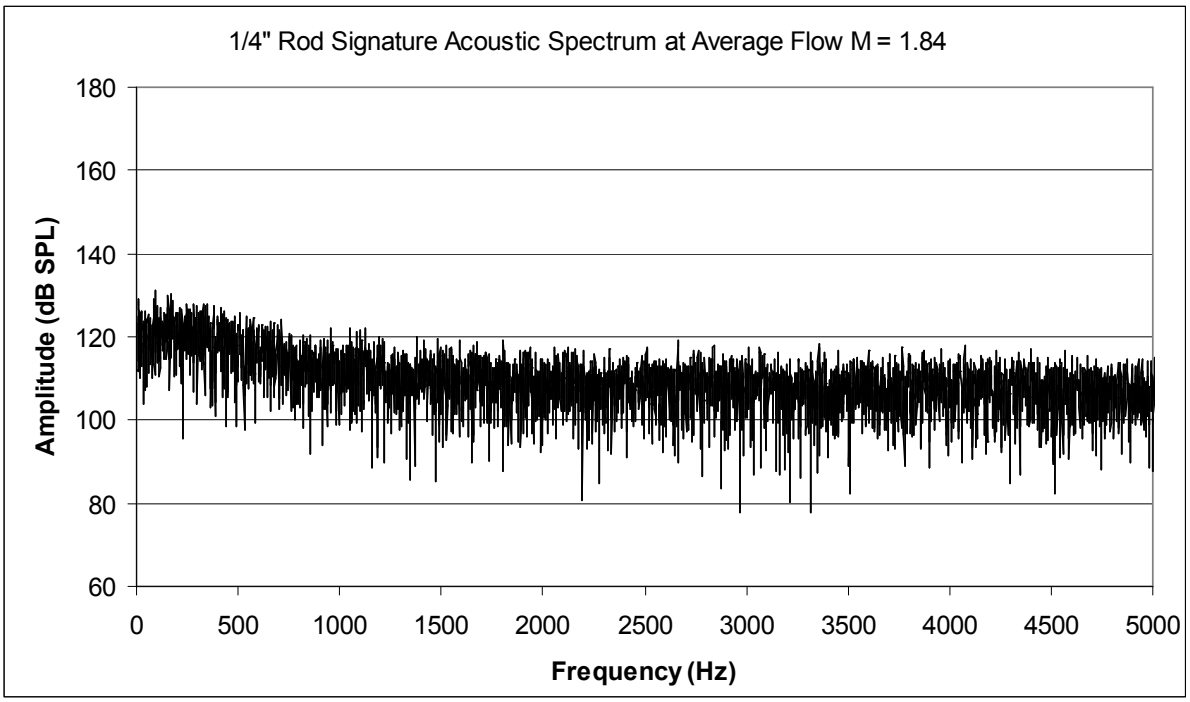

Figure 58. Test Configuration 2a: Rod Signature (Solid Floor Plate) – Acoustic Spectrum from 0 to 5000 Hz

Figure 59 includes a Schlieren photograph of the rod signature solid floor configuration. This photo includes the accumulation of the flow field complexity discussed in both the clean tunnel and side plate flow configurations. The analysis of the shock structure around the rod was further complicated by the side plates obstructing the rod field of view.

To better understand the shock structure for a rod within supersonic flow, the photographs of Van Dyke [23] were studied. Van Dyke described the flow field structure of a circular object at a flow of Mach 1.53 with the use of the shadowgraph image shown in Figure 60. The shadowgraph depicts the typical detached bow wave resulting from rounded surfaces within supersonic flows. Behind the bow wave is a region where a boundary layer separates from the circular surface to cause the formation of an oblique shock. Further downstream is a turbulent flow with a fluctuating wake. The fluctuating wake produces weak disturbances which merge to form another shock wave which is often designated as a wake shock.

The terminology used by Van Dyke was applied to the Schlieren image analysis as shown by Figure 61. The bow wave upstream of the rod leading edge was difficult to see due to its shock structure being obscured by the side plate shock structure. The faint lines angled above and below the rod in the downstream direction indicated an oblique shock followed by the well defined region of the wake shock. Of interest, Figure 61 did not include the labelling of any flow structures associated with the side plates only for the purposes of removing clutter.

PIV was applied to the rod signature solid floor configuration for the purposes of gaining understanding related to the rod wake structure. This included the generation of contour plots from the averaging of multiple vector files and from single vector file instantaneous measurements. Of interest, the INSIGHT PIV software was unable to correlate vectors immediately downstream of the rod as shown by Figure 62. This region without vector correlation may have resulted from poor seeding uniformity within the direct wake of the rod. For the purposes of better flow visualization, each Tecplot post-processed contour plot included a schematic of the rod position.

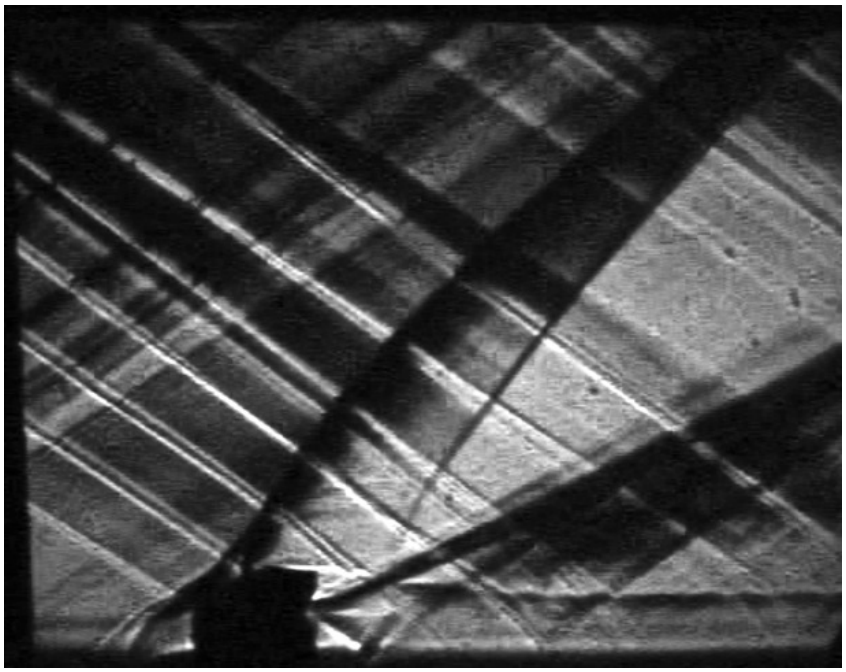

Figure 59. Test Configuration 2a: Rod Signature with Solid Floor – Schlieren Photograph

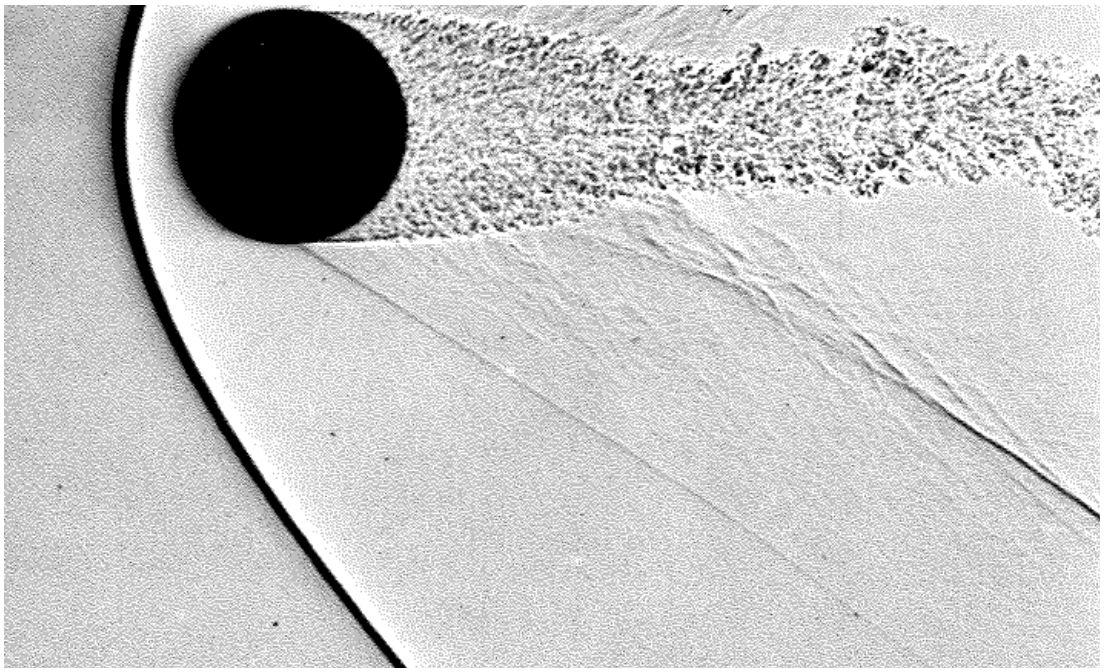

Figure 60. Example Shadowgraph Image of Wake Shock Structure (Van Dyke [23])

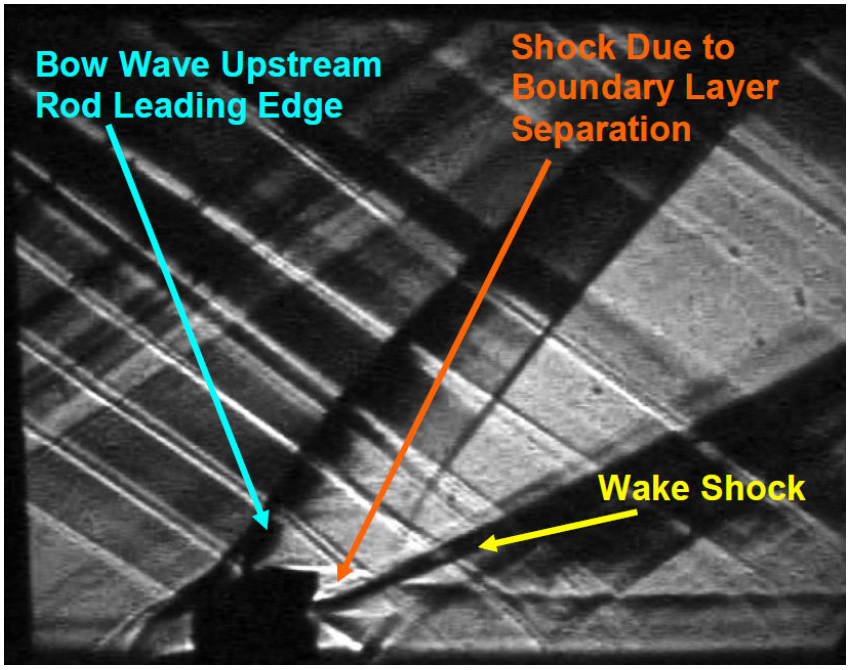

Figure 61. Test Configuration 2a: Rod Signature with Solid Floor – Schlieren Analysis

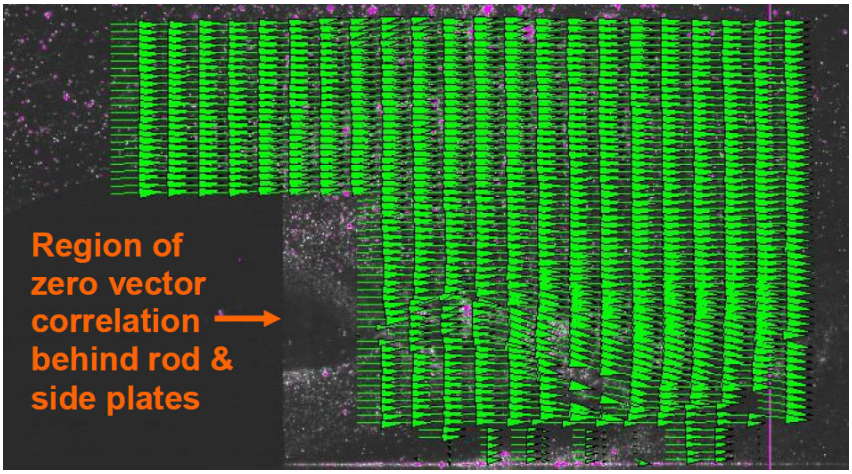

Figure 62. Test Configuration 2a: Rod Signature Region of PIV Zero Vector Correlation

The averaged velocity contour plot for the rod with the solid floor is presented within Figure 63. This plot shows a region of velocity decrease above and possibly below the rod as a result of the shock structure described earlier within Figure 61. The plot shows that the flow velocity recovered to the freestream velocity roughly 20 mm downstream of the rod. The wake structure of the rod was shown to mix with the low speed velocity region of the tunnel floor.

Figure 64 depicts the averaged vorticity contour plot for the rod which showed a tendency for vorticity to form below the centerline of the rod. However, this measurement may have been a result of bias created from the sampling rate of the single PIV images collected. The wake thickness appeared to grow further down the tunnel floor to an approximate thickness of 13 mm. Due to the limited field of view, the overall maximum wake thickness could not be determined.

Figure 65 includes instantaneous snapshots of velocity and vorticity contour plots. The images were not selected in any particular sequence but were chosen to illustrate that vortex shedding did actually occur. The figures showed vortex shedding interactions coming into contact with the low speed region along the tunnel floor. It may be possible that these interactions eventually led to a damping effect on the any vortex shedding pressure fluctuations further downstream. This would account for why there were no observed acoustic phenomena within the predicted vortex shedding frequency range.

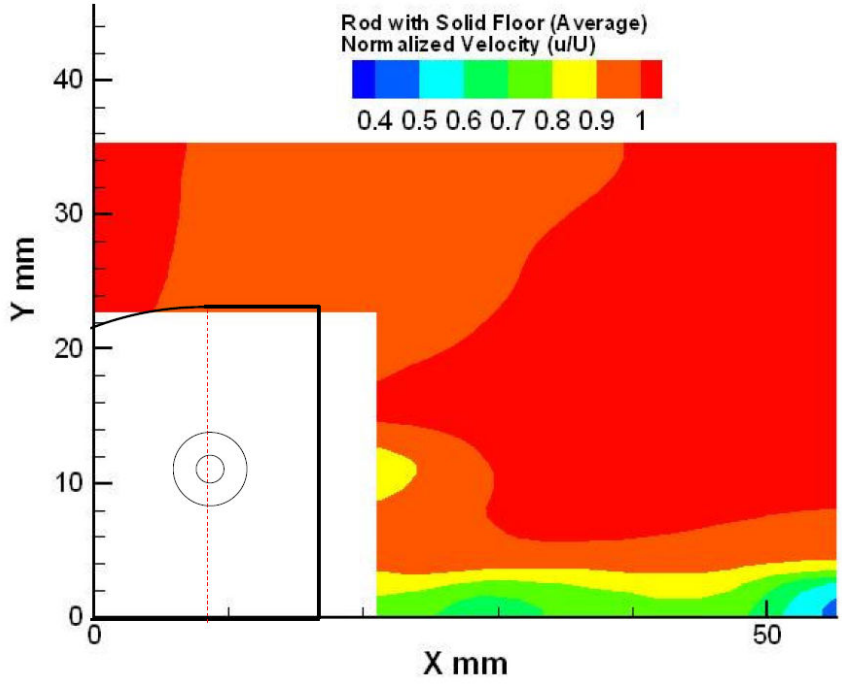

Figure 63. Test Configuration 2a: Rod Solid Floor Average Velocity Contour Plot

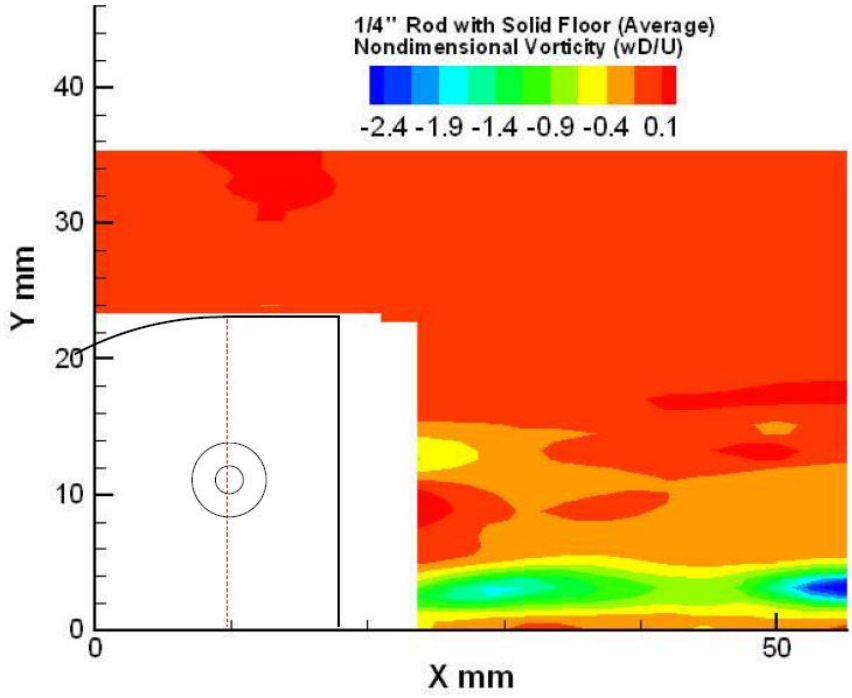

Figure 64. Test Configuration 2a: Rod Solid Floor Average Vorticity Contour Plot

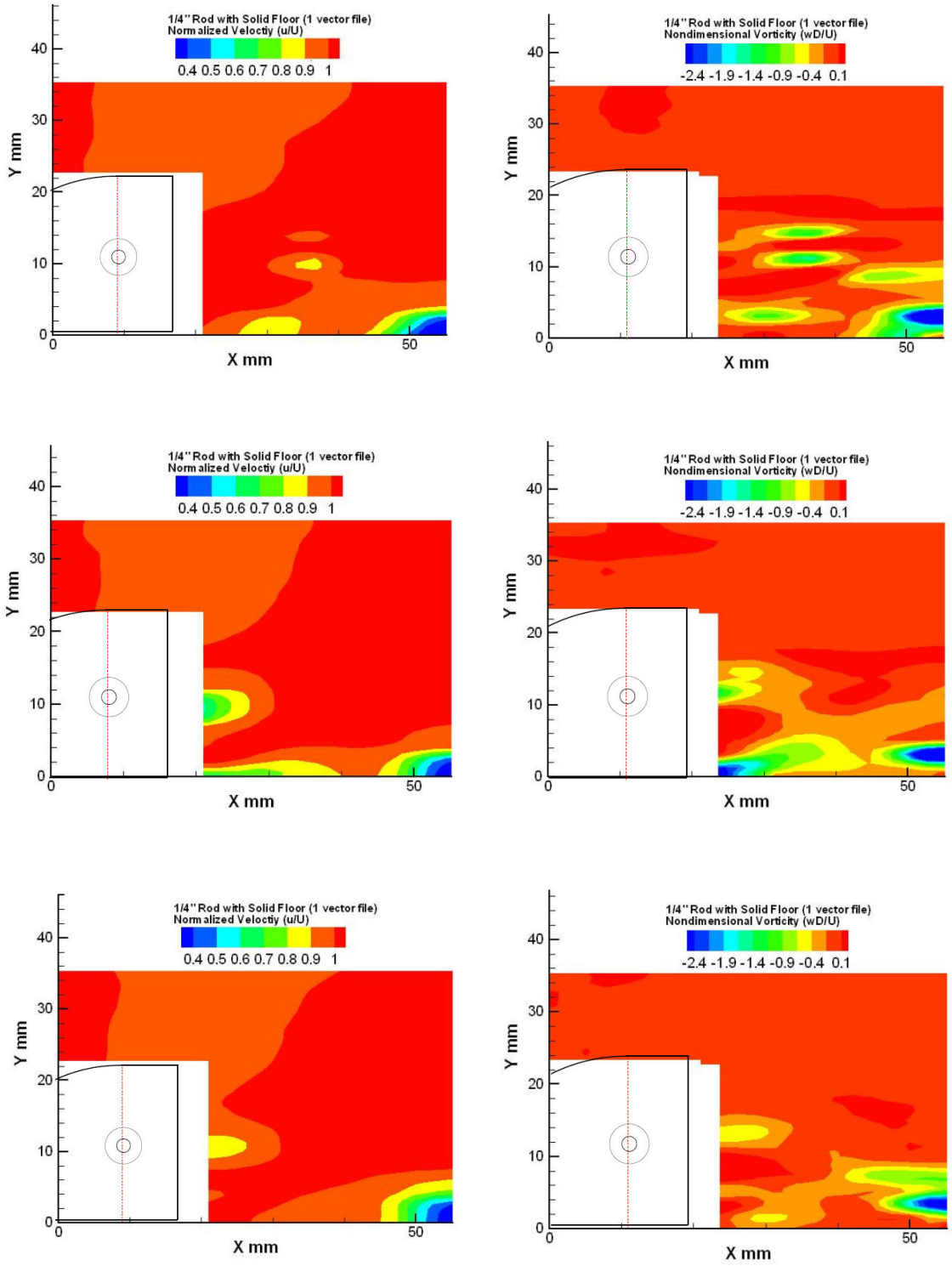

Figure 65. Test Configuration 2a: Rod Solid Floor Instantaneous Contour Plots of Velocity (left) and Vorticity (right)

Test Configurations 2b: Airfoil Signature 0^o Angle of Attack (Solid Floor Plate)

The acoustic spectrum data associated with the zero angle of attack airfoil with solid floor configuration is included within Figure 66. Over the frequency range of 0 to 5000 Hz, the broadband noise was measured to be 106 dB. This includes a 2 dB increase from the clean tunnel acoustic spectrum. Within the narrow frequency range of 0 to 500 Hz, the broadband noise reached approximately 126 dB. As was predicted, no particular acoustic phenomena such as resonant tones were measured for this configuration. It must be noted that if acoustic tones were a result of this configuration, the tones may have not been measurable as was the case with the rod signature solid floor configuration.

Figure 67 includes a Schlieren photograph of the 0 degree angle of attack airfoil signature with solid floor configuration while Figure 68 depicts the Schlieren analysis of its flow structure. Like the rod signature solid floor configuration, the airfoil also exhibited a detached bow wave upstream of its rounded leading edge. The trailing edge of the airfoil included oblique shocks on both its top and bottom surfaces.

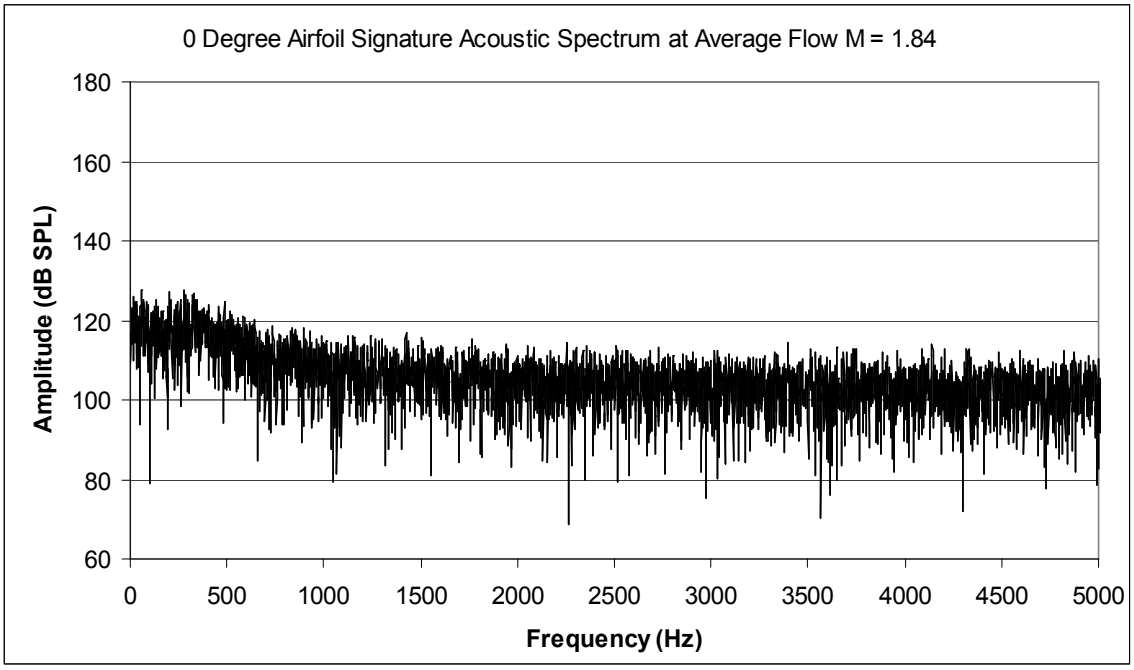

Figure 66. Configuration 2b: Airfoil 0^o Angle of Attack Solid Floor – Acoustic Spectrum

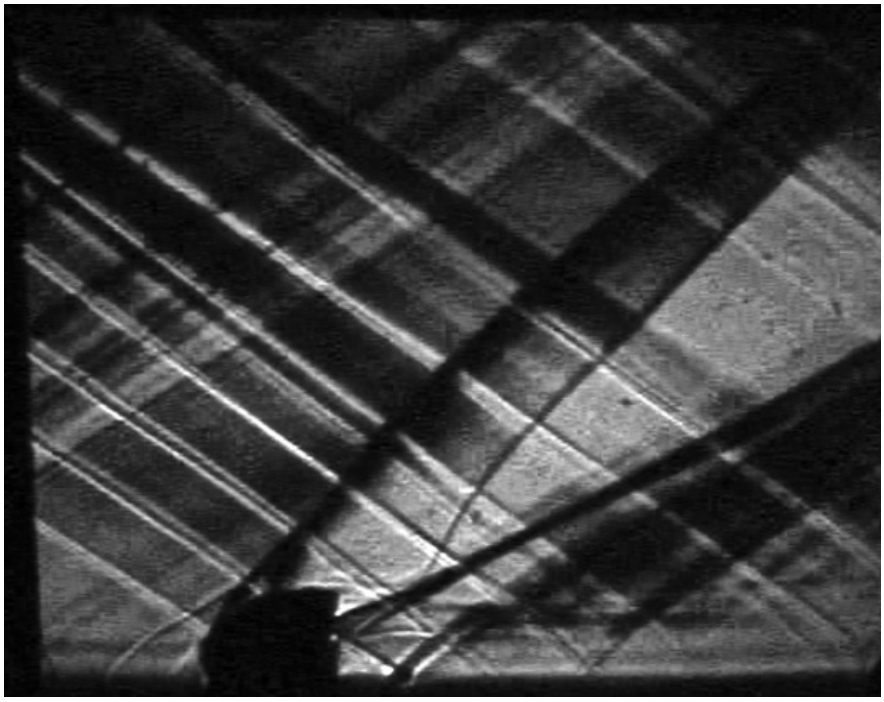

Figure 67. Test Configuration 2b: Airfoil 0^{o} Solid Floor – Schlieren Photograph

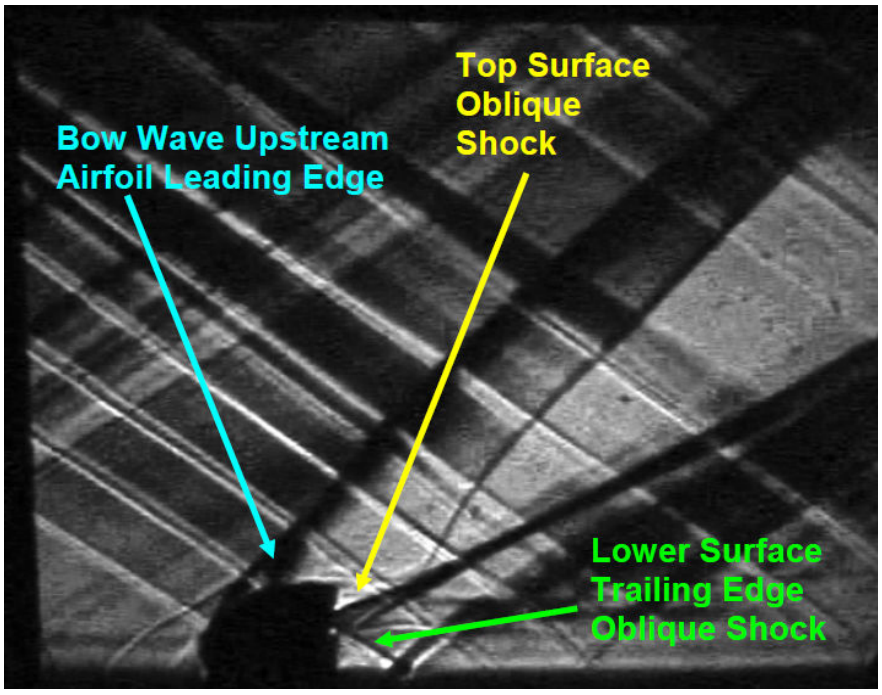

Figure 68. Test Configuration 2b: Airfoil 0^{o} Solid Floor – Schlieren Analysis

The averaged velocity contour plot for the 0 degree angle of attack airfoil with the solid floor is presented within Figure 69. The plot showed some reduction of velocity in the region above the airfoil by the slightly lighter shade of red denoting roughly 90% of the freestream flow velocity. The most significant observation pertained to the significant velocity deficit at the wake of the airfoil. Figure 69 also showed that there was a possibility that the lower surface of the airfoil may have had some interactions with the tunnel floor boundary layer region. However, it does not appear that the tunnel floor boundary layer grew as a result of these interactions.

Figure 70 includes the averaged vorticity contour plot for the 0 degree angle of attack airfoil with the solid floor. The plot indicated that the vorticity on the top and bottom surfaces were in opposite directions. It also showed that the vorticity was almost all localized on the airfoil surfaces with the vorticity fluctuations being almost insignificant downstream of the airfoil trailing edge. The vorticity of the boundary layer region for the tunnel floor appeared to be relatively constant with the exception of a discontinuity at approximately 20 mm. It is anticipated that this discontinuity was caused by the airfoil lower surface oblique shock impinging and reflecting from the tunnel floor.

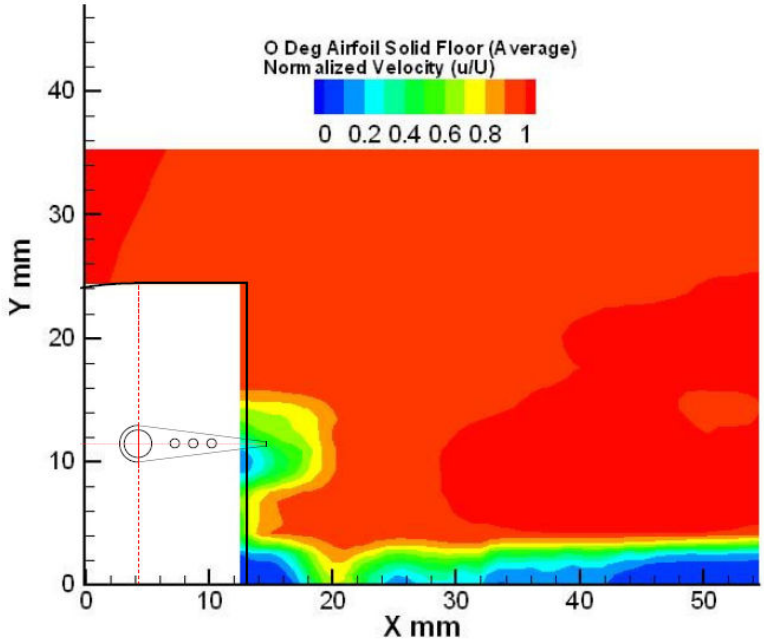

Figure 69. Test Configuration 2b: Airfoil 0^{o} Solid Floor Average Velocity Contour Plot

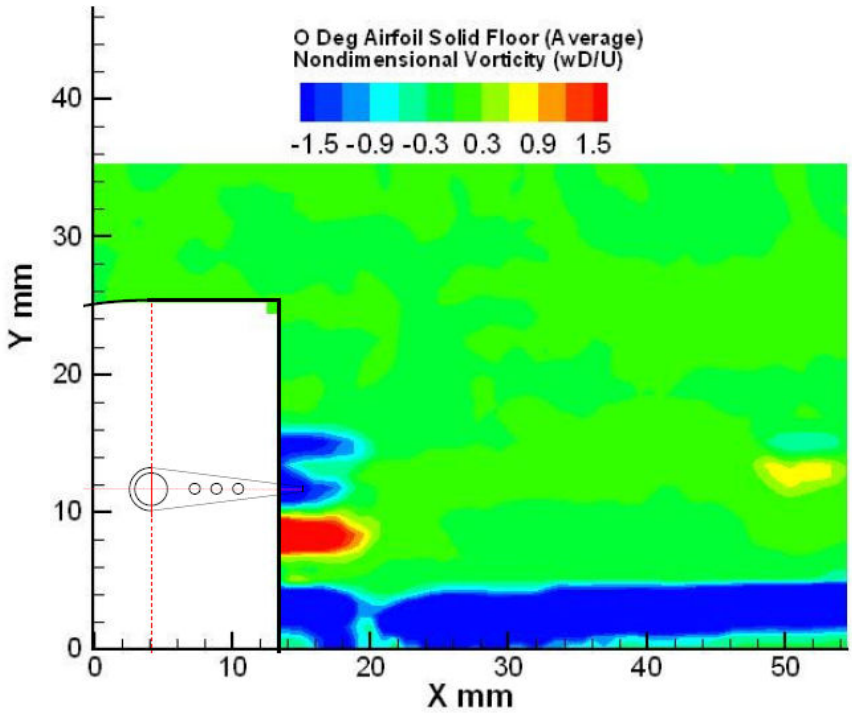

Figure 70. Test Configuration 2b: Airfoil 0^{o} Solid Floor Average Vorticity Contour Plot

Test Configurations 2c: Airfoil Signature -5^{o} Angle of Attack (Solid Floor Plate)

The acoustic spectrum data associated with the -5 degree angle of attack airfoil with solid floor configuration is included within Figure 71. Over the frequency range of 0 to 5000 Hz, the broadband noise was measured to be 106 dB. This includes a 2 dB increase from the clean tunnel acoustic spectrum. It is also the same result as for the 0 degree airfoil configuration. Within the narrow frequency range of 0 to 500 Hz, the broadband noise reached approximately 124 dB. This is the same as the 0 degree airfoil configuration. As was predicted, no particular acoustic phenomena such as resonant tones were measured for this configuration.

Figure 72 includes a Schlieren photograph of the -5 degree angle of attack airfoil signature with solid floor configuration while Figure 73 depicts the analysis of its flow structure. As was the case with the 0 degree angle of attack airfoil, -5 degree airfoil also exhibited a detached bow wave at its rounded leading edge. Within the images, two oblique shocks can be viewed from the

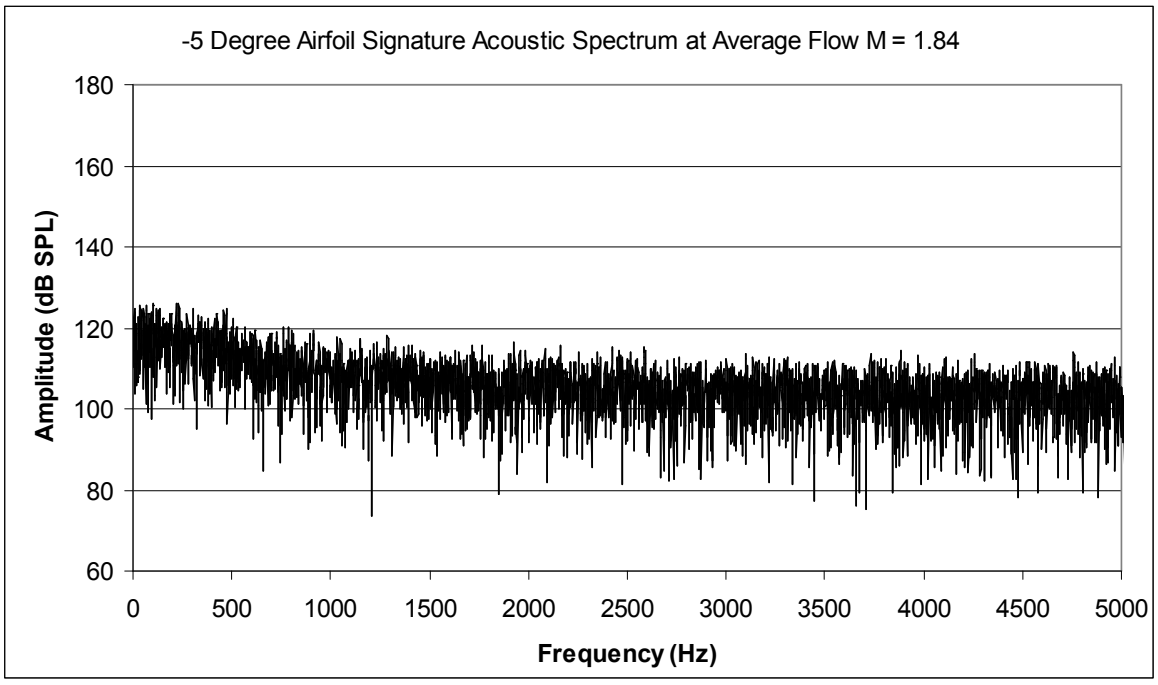

Figure 71. Configuration 2c: Airfoil -5^{o} Angle of Attack Solid Floor – Acoustic Spectrum

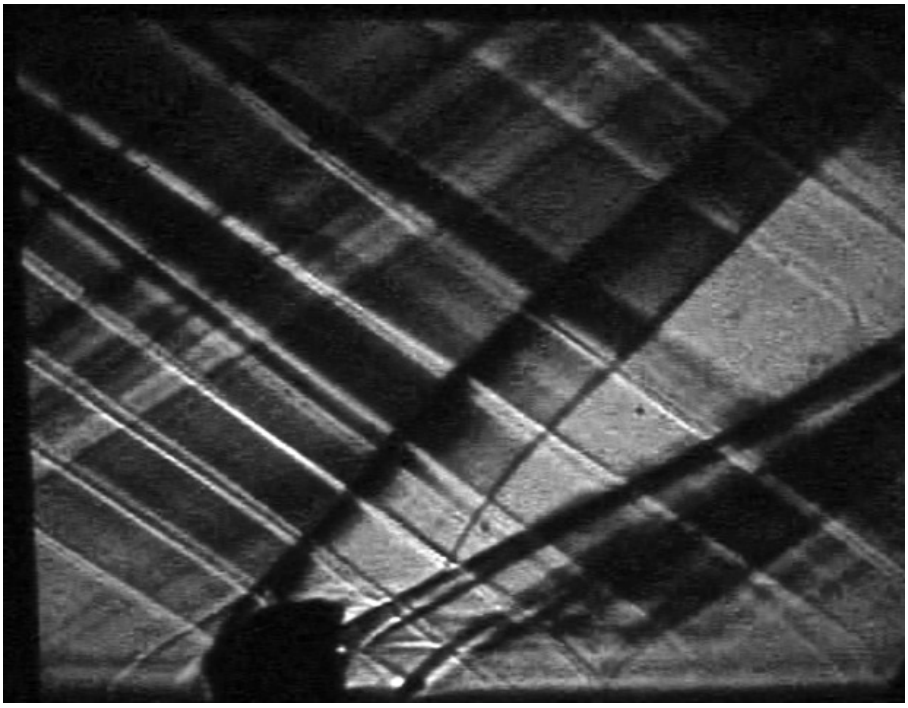

Figure 72. Configuration 2c: Airfoil -5^{o} Solid Floor – Schlieren Photograph

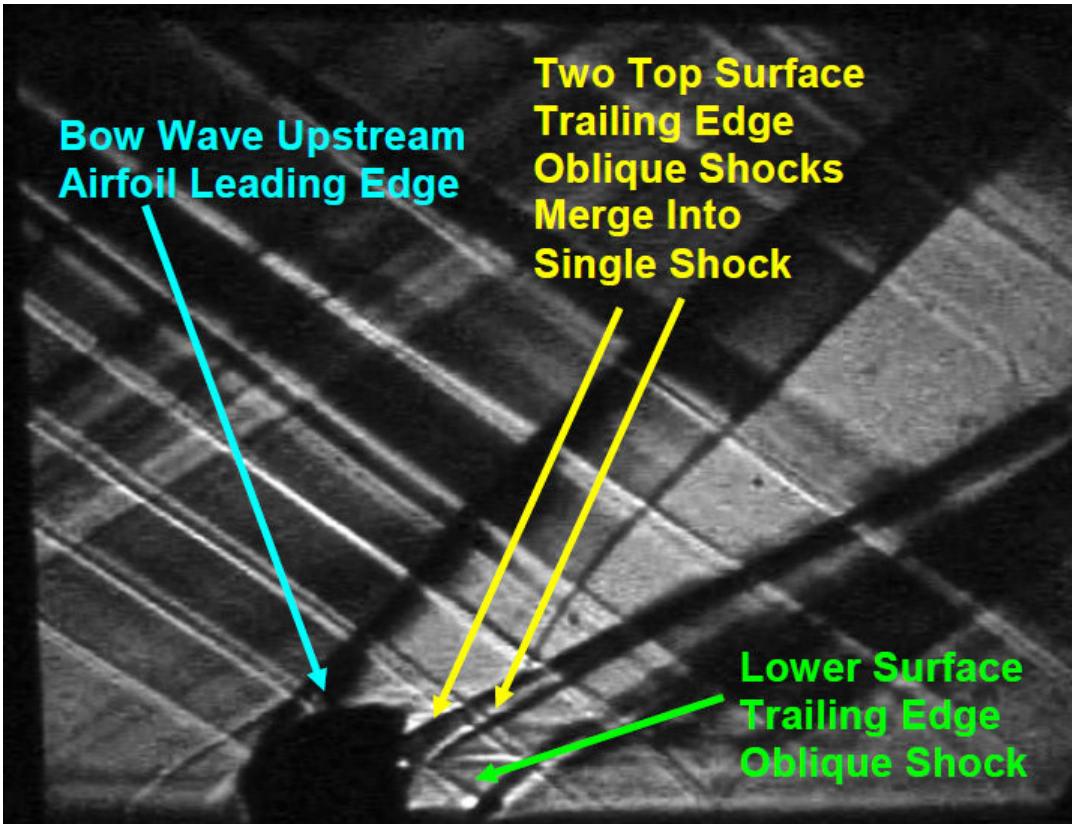

Figure 73. Configuration 2c: Airfoil -5^{o} Solid Floor – Schlieren Analysis

upper surface of the airfoil. It was interpreted that boundary layer separation was the cause of the first upper surface oblique shock (the shock upstream of the trailing edge). Downstream of the airfoil, it appeared that both of the top surface oblique shocks merged into a single shock. The lower surface trailing edge shock appeared to be very similar to the 0 degree angle of attack airfoil case which was also reflected from the bottom of the tunnel floor. Because this configuration very likely experienced a shock due to boundary layer separation, it was deemed highly probable that the airflow of the upper and bottom surfaces remained separated past the trailing edge of the airfoil.

The averaged velocity contour plot for the -5 degree angle of attack airfoil with the solid floor is presented within Figure 74. The plot showed a reduction of velocity in the region above the airfoil to approximately 80% of the freestream flow. This airfoil configuration showed a larger

region of velocity deficit at its wake when compared with the 0 degree angle of attack configuration. Figure 74 showed some interactions between airfoil lower surface with the tunnel floor which were likely caused by the airfoil lower surface oblique shock wave impinging and reflecting from the tunnel floor.

Figure 75 includes the averaged vorticity contour plot for the -5 degree angle of attack airfoil with the solid floor. The plot indicated that the vorticity on the top and bottom surfaces were in opposite directions and almost all localized on the airfoil surfaces with the vorticity fluctuations being almost insignificant downstream of the airfoil trailing edge. Overall, this configuration showed virtually no vorticity interactions between the airfoil wake and tunnel floor boundary layer. The divided top and bottom airfoil vorticity regions provided further evidence that flow airfoil flow separation had occurred with this configuration.

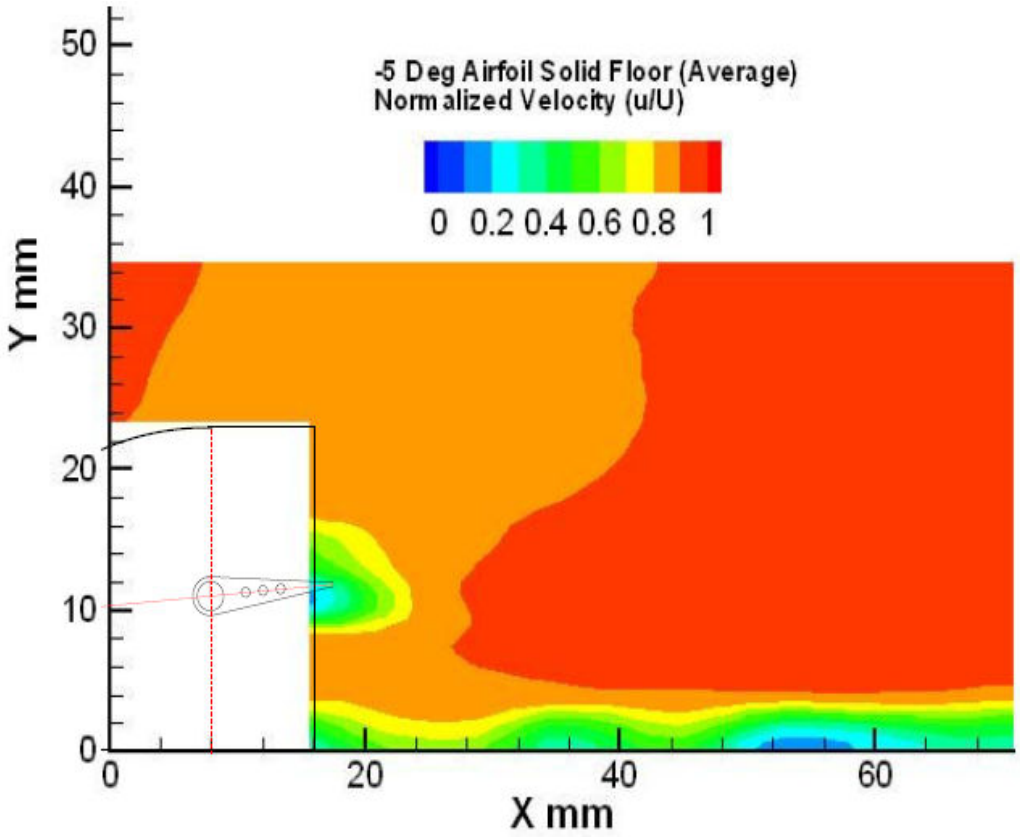

Figure 74. Test Configuration 2c: Airfoil -5^{o} Solid Floor Average Velocity Contour Plot

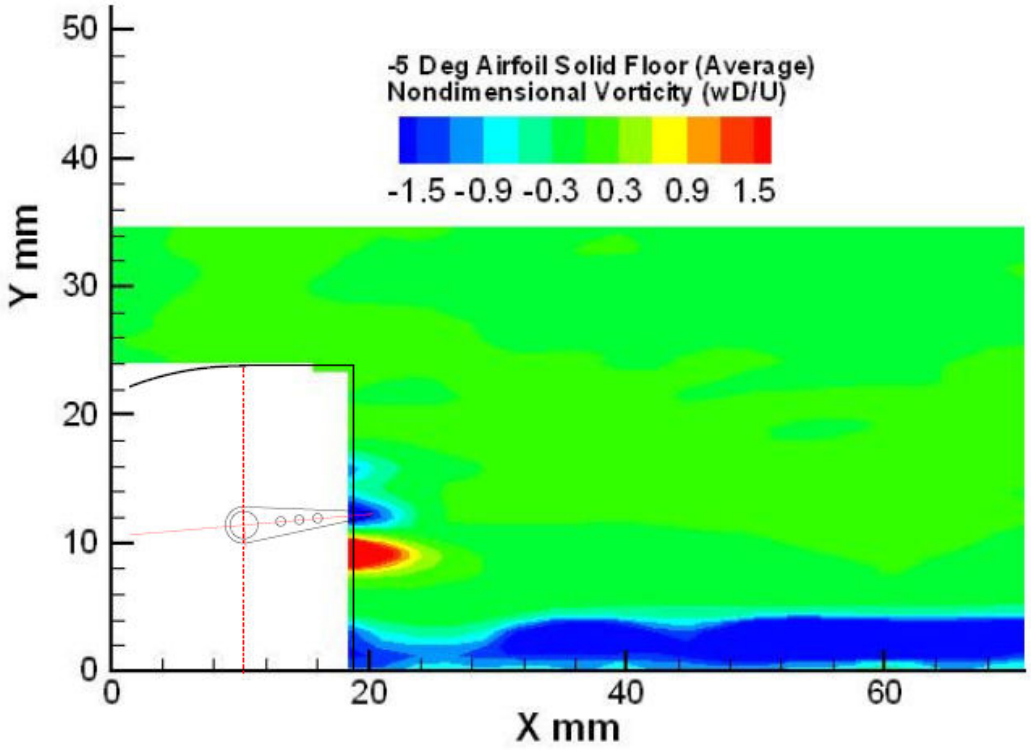

Figure 75. Test Configuration 2c: Airfoil -5^{o} Solid Floor Average Vorticity Contour Plot

Test Configurations 2d: Airfoil Signature -10^{o} Angle of Attack (Solid Floor Plate)

The acoustic spectrum data associated with the -10 degree angle of attack airfoil with solid floor configuration is included within Figure 76. Over the frequency range of 0 to 5000 Hz, the broadband noise was measured to be 106 dB. This is a 2 dB increase from the clean tunnel acoustic spectrum. It is also the same result as for the 0 and -5 degree airfoil configuration. Within the narrow frequency range of 0 to 500 Hz, the broadband noise reached approximately 125 dB. This is one dB less from the 0 and -5 degree airfoil configurations. As was predicted, no particular acoustic phenomena such as resonant tones were measured for this configuration.

Figure 77 includes a Schlieren photograph of the -10 degree angle of attack airfoil signature with solid floor configuration while Figure 78 depicts the analysis of its flow structure. As was the case with the 0 and -5 degree angle of attack airfoils, -10 degree airfoil also exhibited a detached bow wave at its rounded leading edge. Two oblique shocks can be viewed from the upper

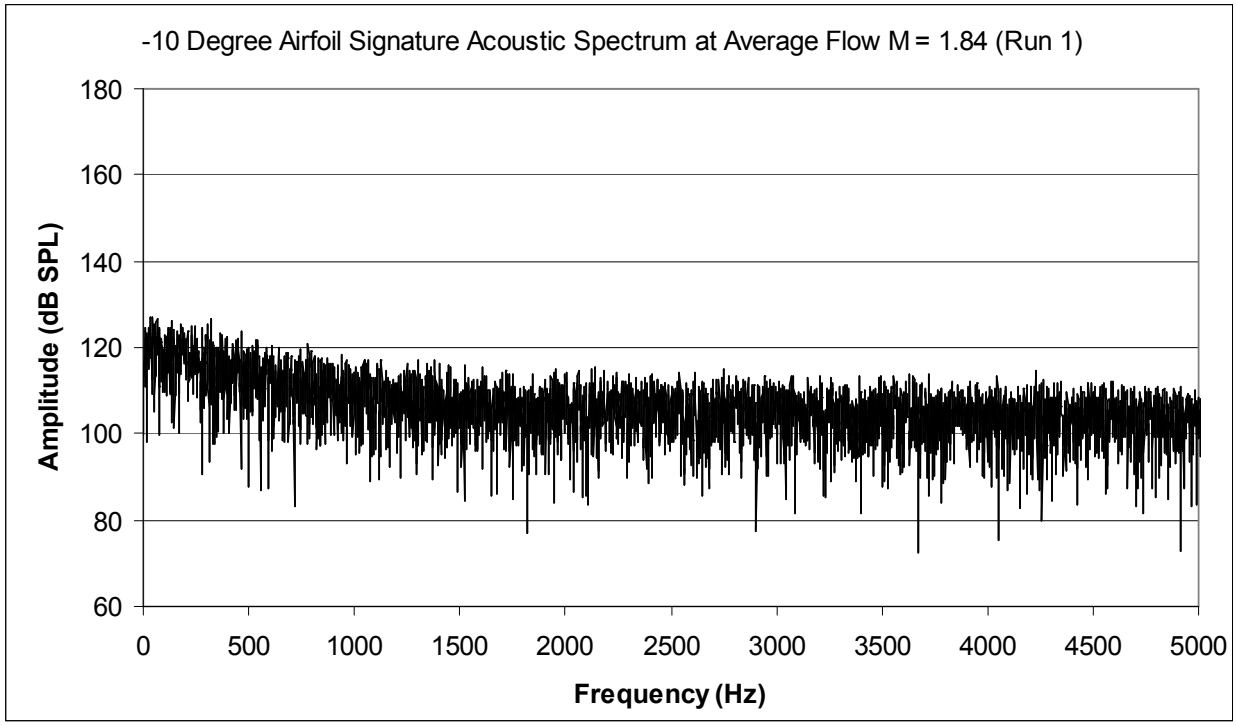

Figure 76. Configuration 2d: Airfoil -10^{o} Angle of Attack Solid Floor – Acoustic Spectrum

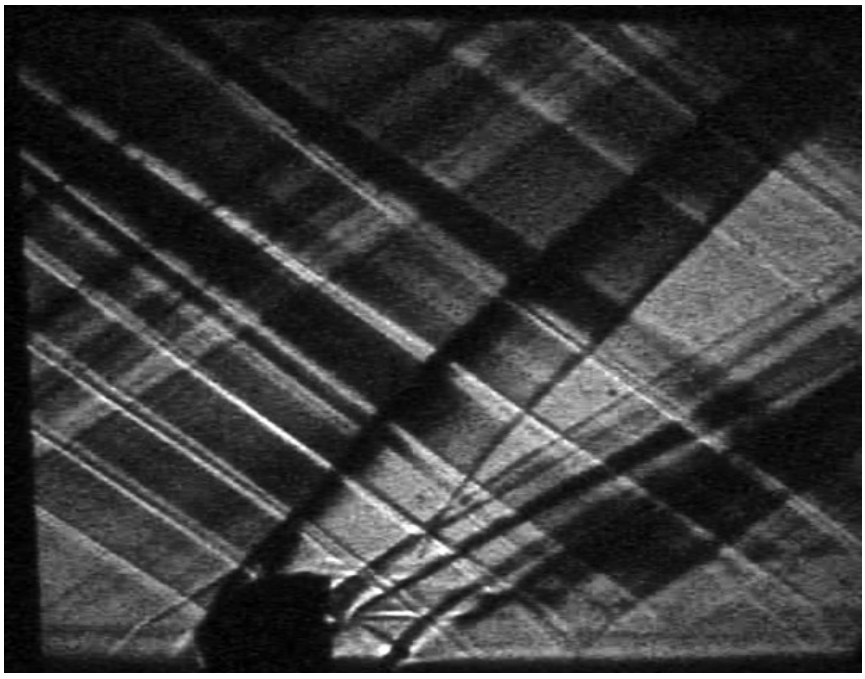

Figure 77. Configuration 2d: Airfoil -10^{o} Solid Floor – Schlieren Photograph

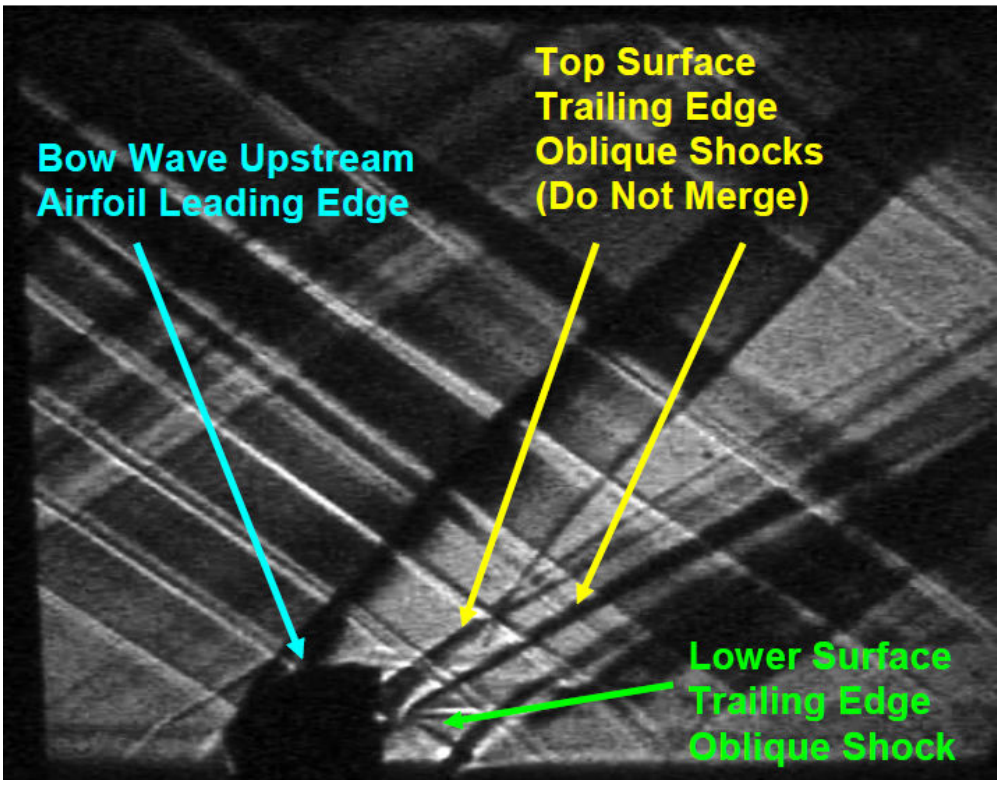

Figure 78. Configuration 2d: Airfoil -10^{o} Solid Floor – Schlieren Analysis

surface of the airfoil. Unlike the -5 degree airfoil case, both of these shocks did not merge into a single shock. It was interpreted that the shock upstream of the trailing edge was a result of boundary layer separation. The lower surface trailing edge shock appeared to be very similar to the 0 and -5 degree angle of attack airfoil cases. Because this configuration experienced a very well defined shock likely due to boundary layer separation, it was deemed that this configuration likely experienced a substantially greater amount of flow separation at the airfoil trailing edge in comparison to the -5 and 0 degree angle of attack configurations.

The averaged velocity contour plot for the -10 degree angle of attack airfoil with the solid floor configuration is presented within Figure 79. Like the -5 degree case, the plot showed a reduction of velocity in the region above the airfoil to approximately 80% of the freestream flow. This configuration showed the largest velocity deficit at its wake when compared with both the 0 and -5 degree angle of attack configurations. Like the other airfoil configurations, there were some

interactions between the flow field of the lower airfoil surface with the tunnel floor boundary layer. These interactions were likely caused by the airfoil lower surface trailing edge oblique shock impinging and reflecting on the tunnel floor.

Figure 80 includes the averaged vorticity contour plot for the -10 degree angle of attack airfoil with the solid floor. The plot included indications of flow separation as indicated by the vorticity on the top and bottom surfaces being in opposite directions and primarily localized on the airfoil surfaces. In this case, the top and bottom airfoil vorticity regions vorticity regions around the airfoil appeared to be larger than the 0 and -5 degree configurations. The figure also showed some very low intensity vorticity interactions occurred downstream of the airfoil which are denoted in light blue.

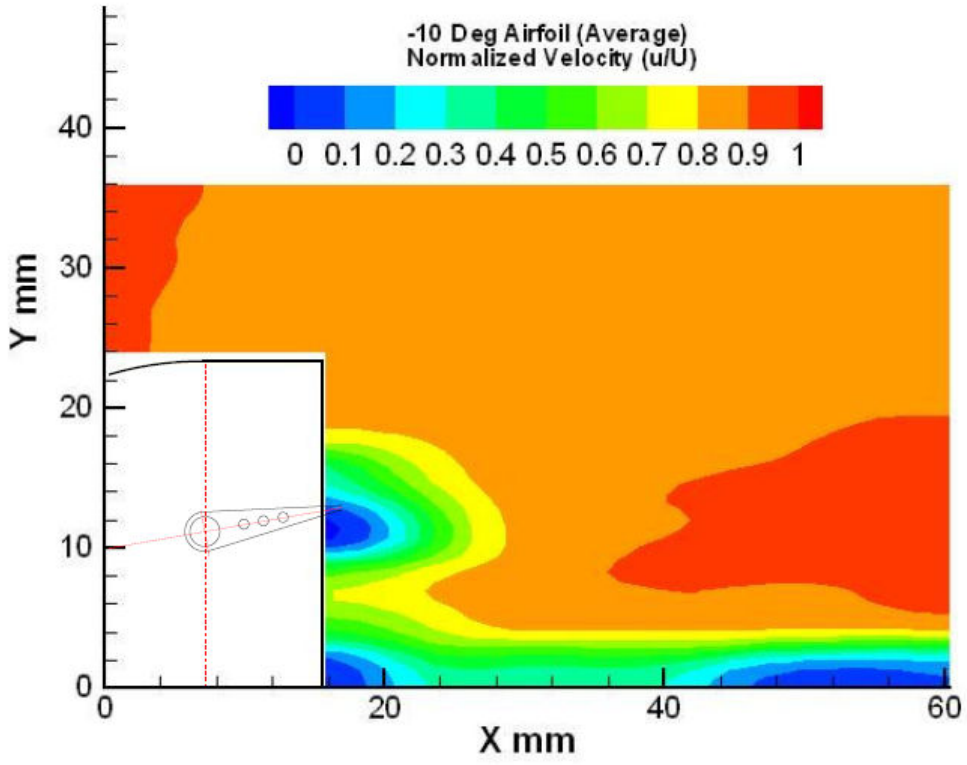

Figure 79. Test Configuration 2d: Airfoil -10^{o} Solid Floor Average Velocity Contour Plot

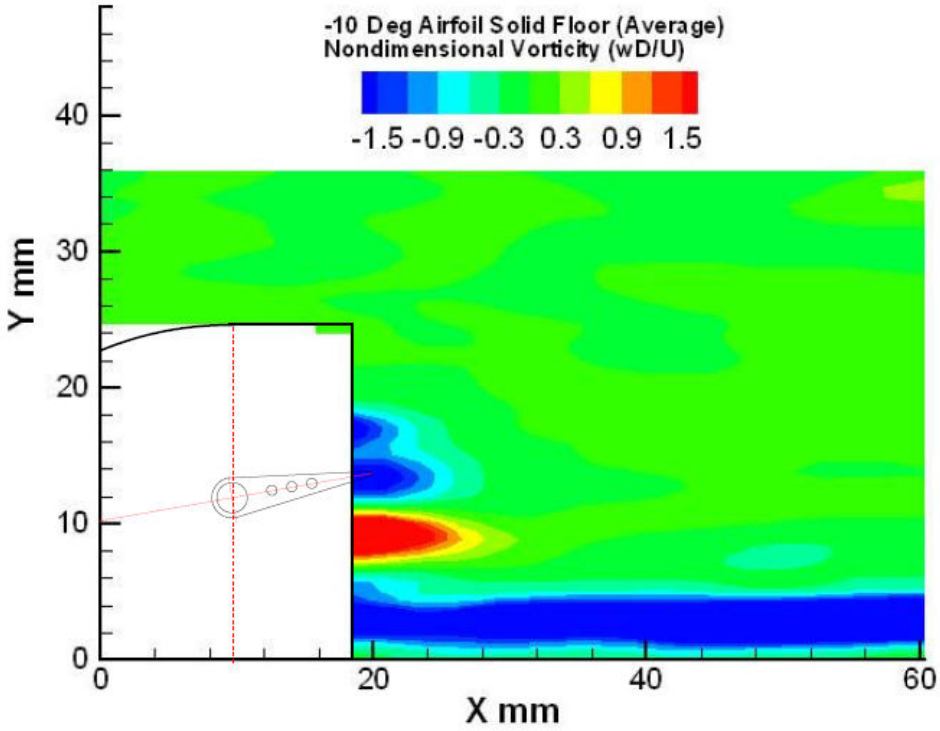

Figure 80. Test Configuration 2d: Airfoil -10^{o} Solid Floor Average Vorticity Contour Plot

Test Configuration 3: Baseline Cavity

The acoustic spectrum data associated with the baseline cavity configuration is included within Figure 81. The results of the test were summarized and compared with the predictions provided by the modified Rossiter Equation (3) as shown within Table 7. Over the frequency range of 0 to 5000 Hz, the broadband noise was measured to be 135 dB. This was substantial increase of 31 dB from the clean tunnel broad band noise of 104 dB. The observed resonant frequencies ranged from between 7 to 24% difference with the modified Rossiter Equation. This showed strong agreement overall between theoretical prediction with experimental results. The second Rossiter mode, m = 2, showed the highest amplitude peak of all the Rossiter modes. It was measured to be 164 dB.

Figure 82 includes a Schlieren photograph of the baseline cavity configuration while Figure 83 depicts the analysis of its flow structure. The thin vertical line on the image was the result of

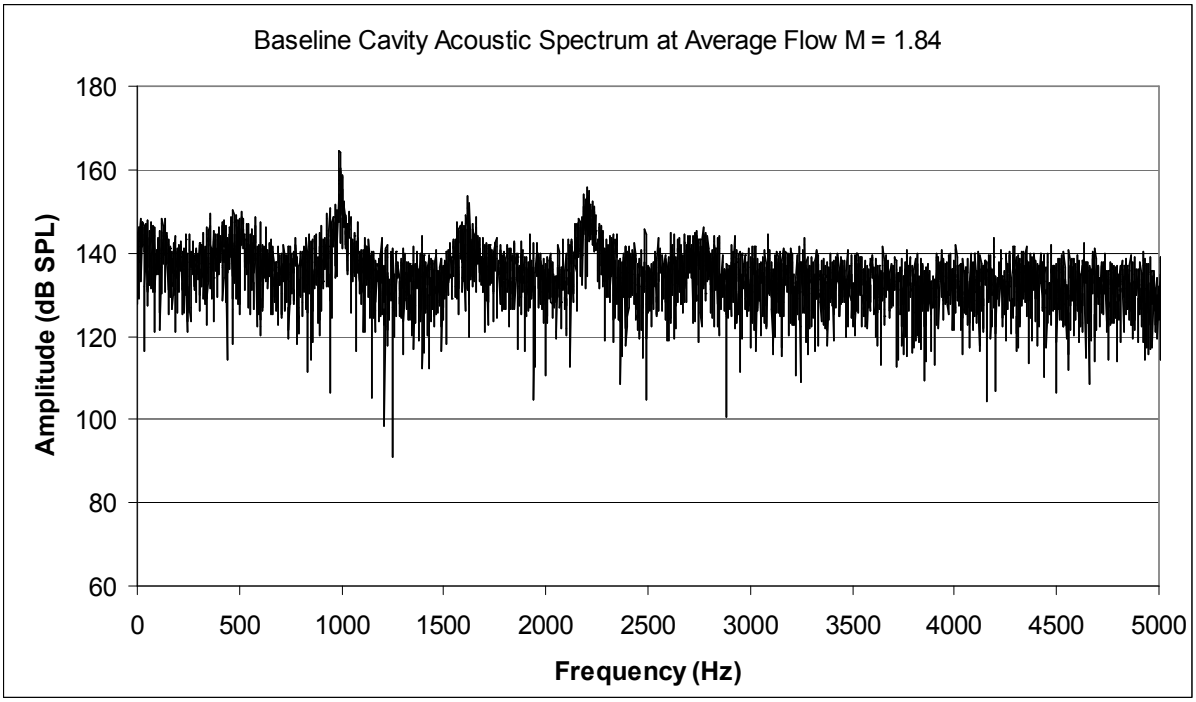

Figure 81. Test Configuration 3: Baseline Cavity – Acoustic Spectrum

Table 7: Baseline Cavity Results Compared with Modified Rossiter Equation

Rossiter Mode, m	Modified Rossiter Equation Predicted Resonant Tones $f = S\frac{U}{L}$	Experimentally Determined Resonant Tones f	Experimentally Determined Peak Amplitudes
-	Hz	Hz	db SPL
1	414	484	151.6
2	967	991	164.3
3	1519	1618	153.6
4	2071	2212	157.7

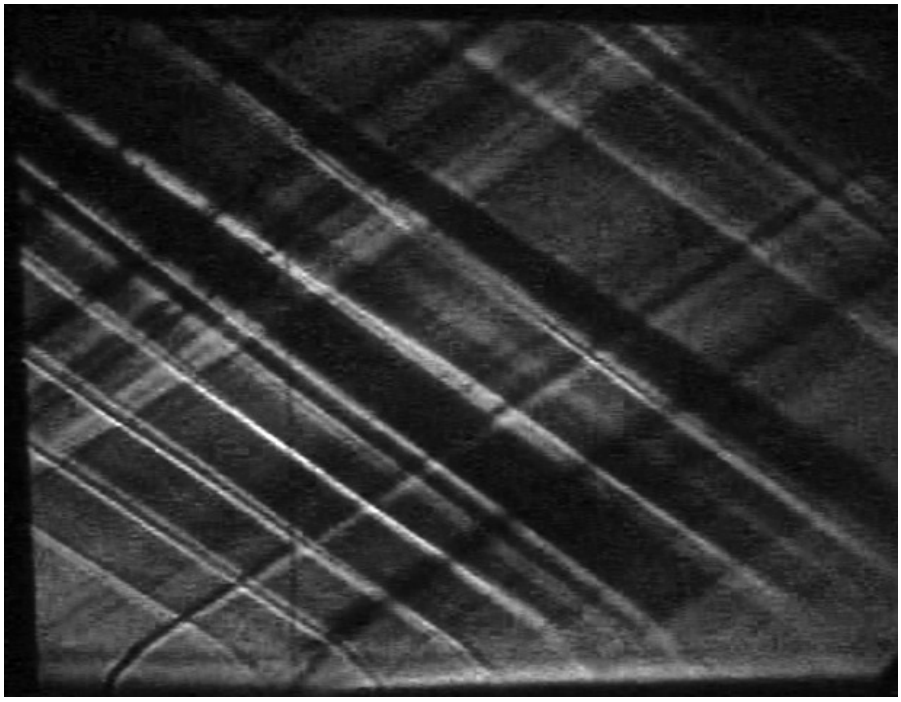

Figure 82. Test Configuration 3: Baseline Cavity – Schlieren Photograph

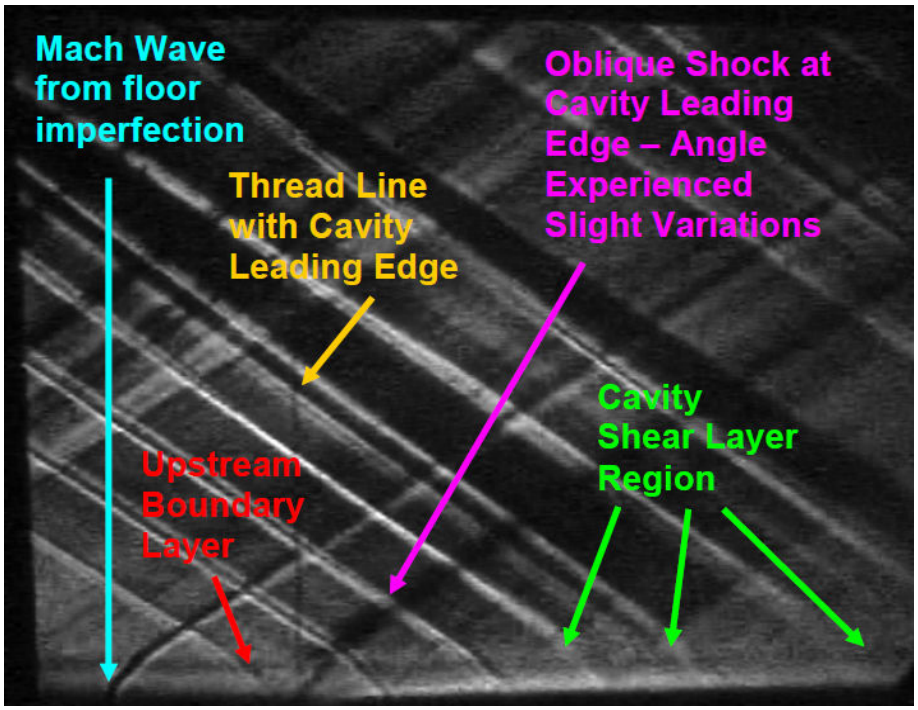

Figure 83. Test Configuration 3: Baseline Cavity – Schlieren Analysis

placing a thread on the glass window outside of the test section for the purpose of providing identification of the cavity leading edge. The test indicated the presence of an oblique shock at the cavity leading edge just as shown within the Figure 2 schematic for supersonic open cavity flow provided by Plentovich, Stalling & Tracy [3]. The Schlieren video footage also indicated that the cavity leading edge oblique shock angle always experienced small fluctuations with time. From the cavity model presented by Heller & Bliss [12], it was the motion of the cavity spanning shear layer that was attributed to the angle fluctuations of the leading edge oblique shock. The Schlieren analysis also showed faint indications that the cavity spanning shear layer experienced slight growth downstream.

The averaged velocity contour plot for the baseline cavity configuration is presented within Figure 84. The small arrow located at 2 mm along the x-axis represents the leading edge of the cavity. This image definitely illustrates the limited field of view available for the PIV testing for all of the cavity configurations. The contour plot includes roughly 40 mm of distance when the overall cavity is roughly 248 mm (11 inch) total length. The contour plot therefore only represents 16% of the total cavity length. A shortcoming of the PIV data included the very low velocities measured at roughly y = 0 mm. In reality, there should have been measurable velocity fluctuations within this region as the cavity spanning shear layer was not constrained by the no-slip boundary condition once it detached from floor at to the cavity leading edge.

The averaged vorticity contour plot for the baseline cavity configuration is presented within Figure 85. The dark blue contour region represented a region of dramatic vorticity gradient within the cavity spanning shear layer. The vorticity contour upward angle at the cavity leading edge showed strong agreement with the supersonic cavity flow schematics provided by Heller & Bliss [12]. It was this upward angle of the shear layer that was attributed to behaving like a ramp for the generation of an oblique shock at the cavity leading edge. The angle of the cavity oblique shock fluctuated with time as a result of the leading edge shear layer angle varying with time. Although the field of view was very limited, there was still indication of a very gradual growth of the cavity spanning shear layer with upstream distance across the cavity.

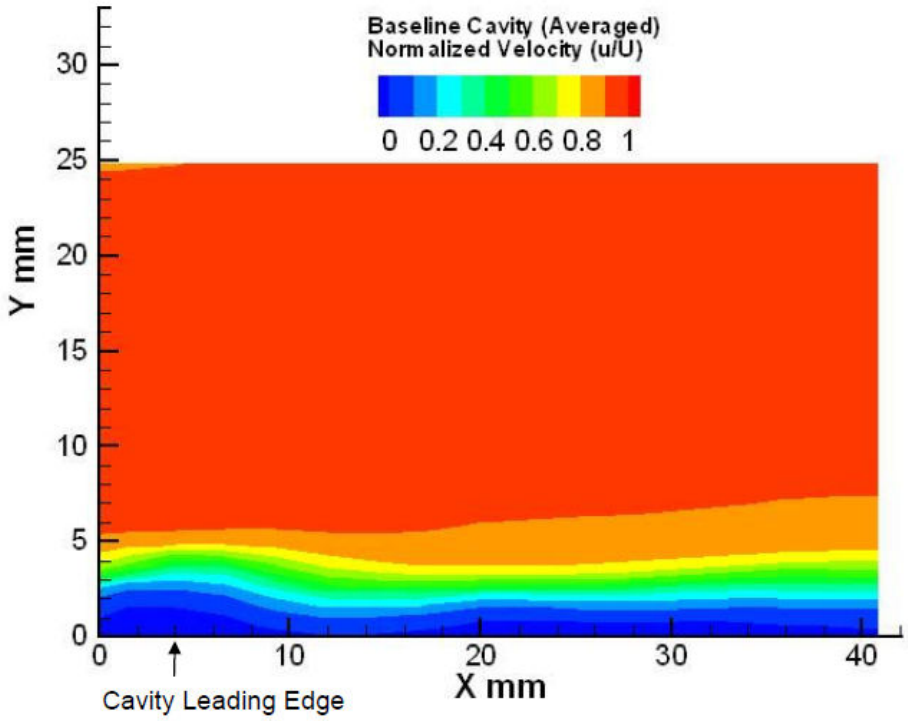

Figure 84. Test Configuration 3: Baseline Cavity Average Velocity Contour Plot

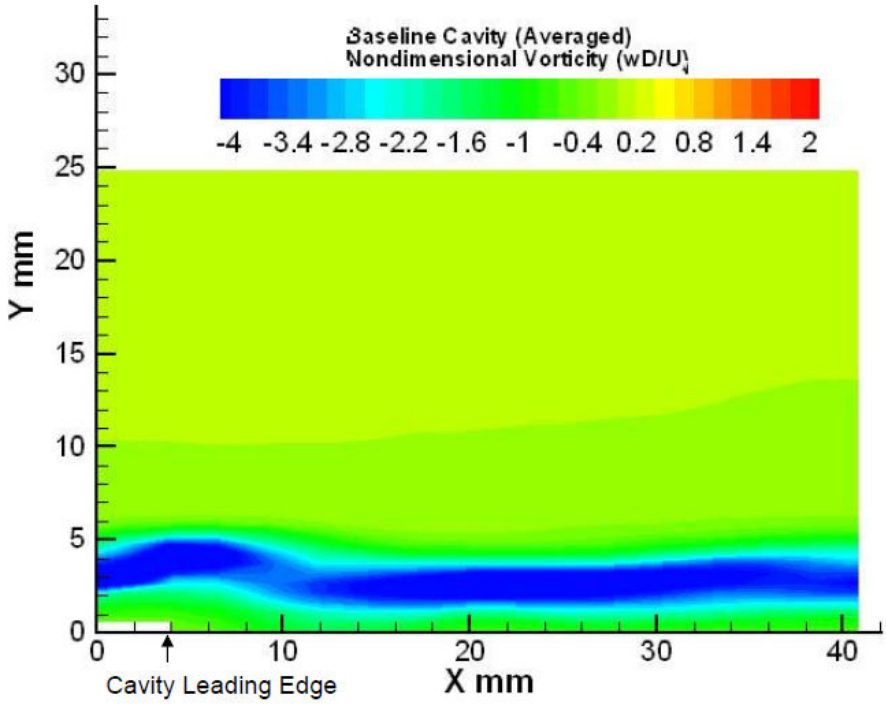

Figure 85. Test Configuration 3: Baseline Cavity Average Vorticity Contour Plot

Supplemental Test Configuration 3a: Side Plates Only with Cavity

The acoustic spectrum for the side plates with cavity is shown within Figure 86. The results were compared with the baseline cavity in Table 8. The were only negligible differences between the acoustic spectra of the two configurations. Over the frequency range of 0 to 5000 Hz, the broadband noise was 135 dB which was the same for the baseline cavity. Resonant frequencies were within 12% difference for the two configurations. The first and second mode peak amplitudes increased by roughly 0.5 dB while the third and forth mode peak amplitudes decreased by 3.9 and 0.9 dB respectively. These small variations may be attributed to the errors in the pressure measurements and for the spectrum calculations to plus or minus 2 dB.

Figure 87 includes a Schlieren photograph of the configuration while Figure 88 includes a flow field annotated version. A detached compression shock was formed upstream of the lower side plate leading edge. The compression shock showed a bow wave shape along the side plates and included a three dimensional component as exhibited by the shock wave impinging the glass window. A very faint horizontal line downstream of the side plates was attributed to a tip vortex. As shown with the baseline cavity, an oblique shock originating from the cavity leading edge was observed.

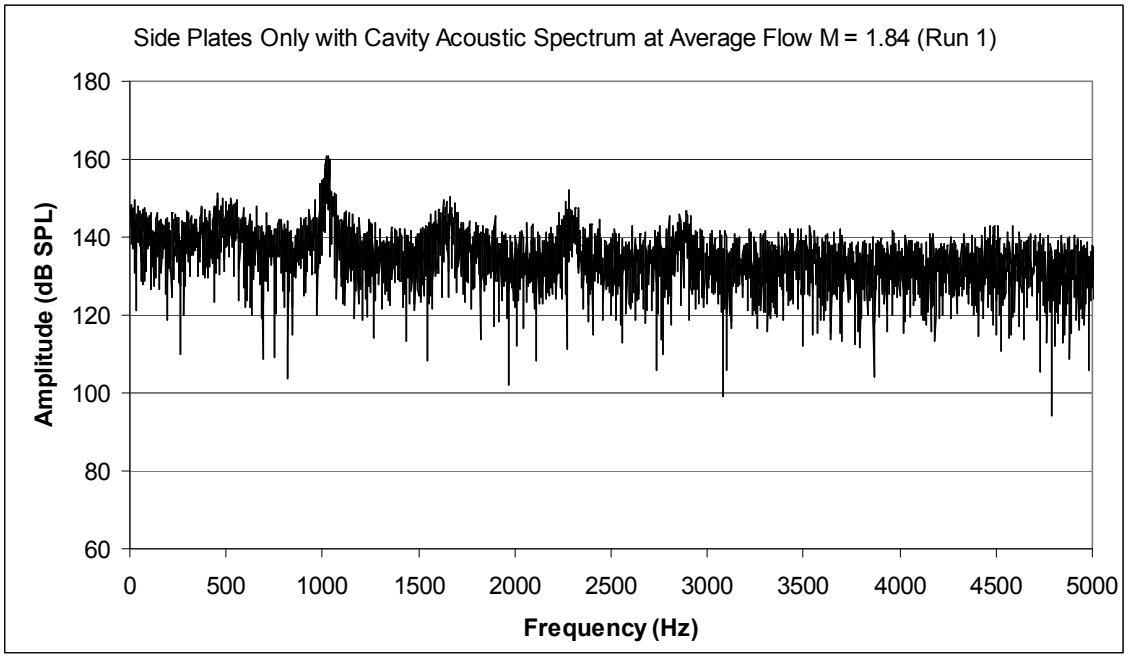

Figure 86. Configuration 3a: Side Plates Only with Cavity – Acoustic Spectrum

Table 8: Side Plates Only with Cavity Compared with Baseline Cavity Acoustic Spectrum

Mode m	Side Plates with Cavity Resonant Tone Frequencies *f*	Side Plates with Cavity Peak Amplitudes	Baseline Cavity Resonant Tone Frequencies *f*	Baseline Cavity Peak Amplitudes	Variation from Baseline Cavity Tone Frequencies *df*	Reduction from Baseline Cavity Peak Amplitudes
-	Hz	db SPL	Hz	db SPL	Hz	db SPL
1	463	152.2	414	151.6	49	-0.6
2	992	164.8	967	164.3	25	-0.5
3	1604	149.7	1519	153.6	85	3.9
4	2212	156.8	2071	157.7	141	0.9

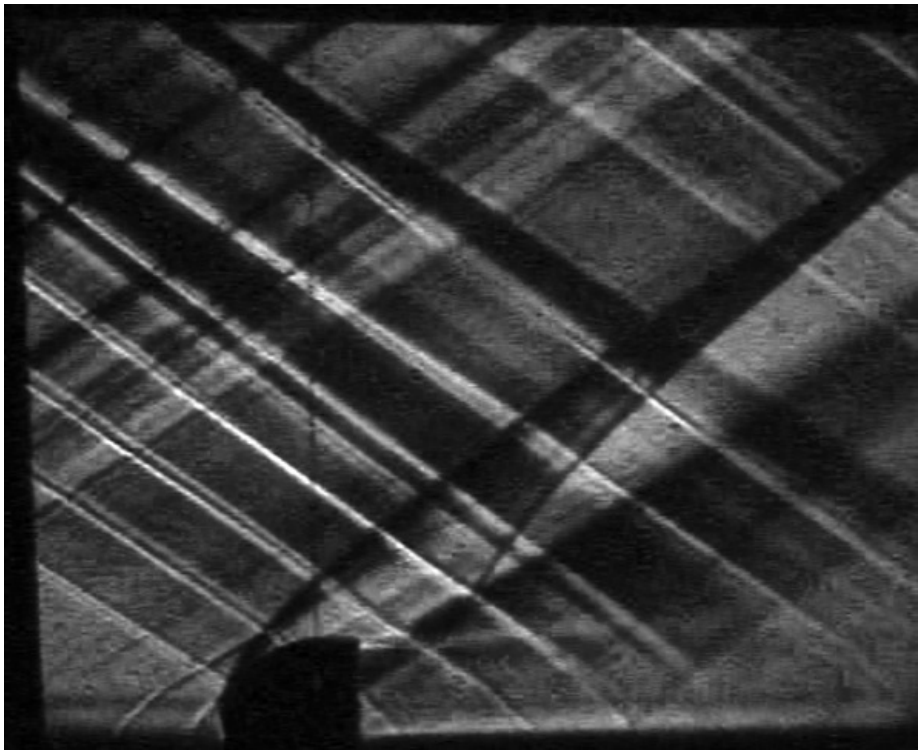

Figure 87. Test Configuration 3a: Side Plates Only with Cavity – Schlieren Photograph

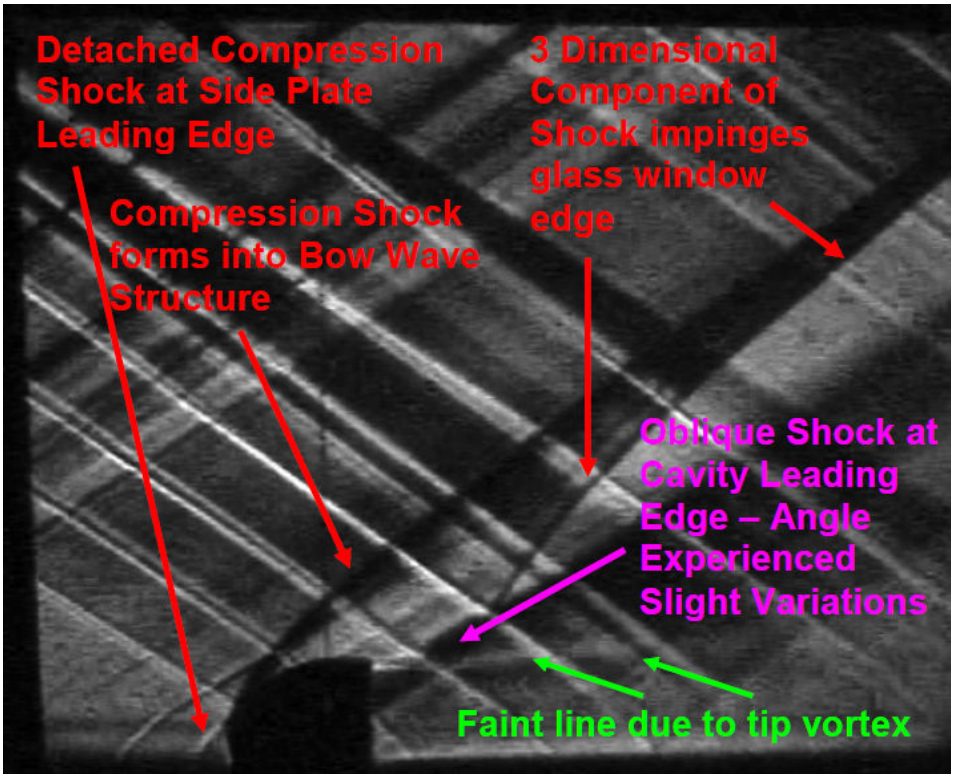

Figure 88. Test Configuration 3a: Side Plates Only with Cavity – Schlieren Analysis

Test Configuration 4a: Rod with Cavity

The acoustic spectrum associated with the rod with cavity configuration is included within Figure 89. The results of the test were summarized and compared with the baseline cavity in Table 9. Of all the tested configurations, the rod in crossflow technique provided the most substantial suppression of resonant tones. Over the frequency range of 0 to 5000 Hz, the broadband noise was 127 dB. This was a reduction of 8 dB from the baseline cavity broadband noise of 135 dB. The observed first and second mode resonant tone frequencies of 435 Hz and 946 Hz were within 5% of those for the baseline cavity. The third and forth mode resonant tone frequencies of 1314 Hz and 1776 Hz were within 13% of those for the baseline cavity. The second mode peak amplitude was 142 dB. This was a significant reduction of 22 dB from the baseline cavity 2nd mode peak amplitude of 164 dB.

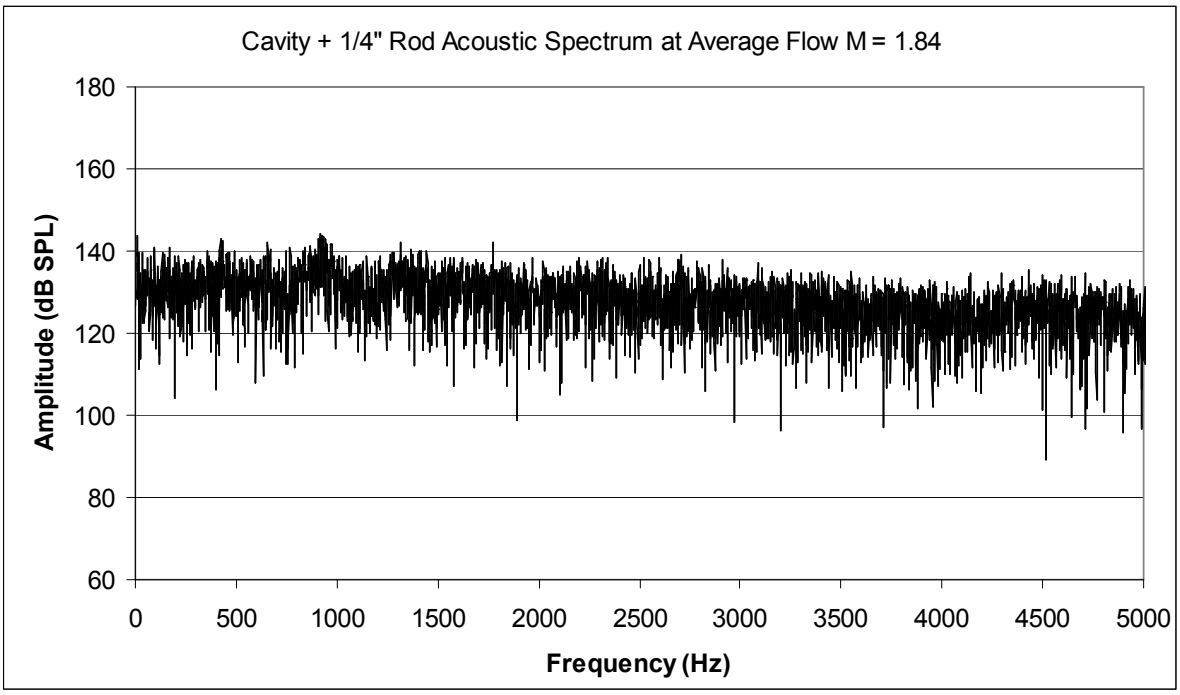

Figure 89. Configuration 4a: Rod with Cavity – Acoustic Spectrum

Table 9: Rod with Cavity Compared with Baseline Cavity Acoustic Spectrum

Mode , m	Side Plates with Cavity Resonant Tone Frequencies *f*	Side Plates with Cavity Peak Amplitudes	Baseline Cavity Resonant Tone Frequencies *f*	Baseline Cavity Peak Amplitudes	Variation from Baseline Cavity Tone Frequencies *df*	Reduction from Baseline Cavity Peak Amplitudes
-	Hz	db SPL	Hz	db SPL	Hz	db SPL
1	435	142.4	414	151.6	21	9.2
2	946	142.2	967	164.3	-21	22.1
3	1314	142.0	1519	153.6	-205	11.6
4	1776	142.2	2071	157.7	-295	15.5

Figure 90 includes a Schlieren photograph of the rod with cavity configuration. Figure 91 includes a flow field annotated version of the Schlieren photograph. The images appeared very similar to the rod with solid floor configurations described earlier within Figures 59 and 61. Both the rod with solid floor and rod with cavity configurations included bow waves upstream of the rod leading edge along with boundary layer separation shocks and wake shocks. Of particular interest was that the rod wake shock and the cavity leading edge shock appeared to become a single entity. From the photograph, it appeared that only the rod in crossflow wake shock was present with no actual indication of a cavity leading edge shock. However, the Schlieren video footage showed that the wake shock experienced easily observable angle fluctuations with time that were of greater frequency than the angle fluctuations observed for only the baseline cavity configuration leading edge oblique shock. Because the high frequency shock angle fluctuations for the rod with cavity configuration appeared qualitatively much higher from the frequency of the baseline cavity leading edge shock angle fluctuations, there may actually be some evidence of high frequency forcing being a contributing factor for the suppression of cavity tones during this test.

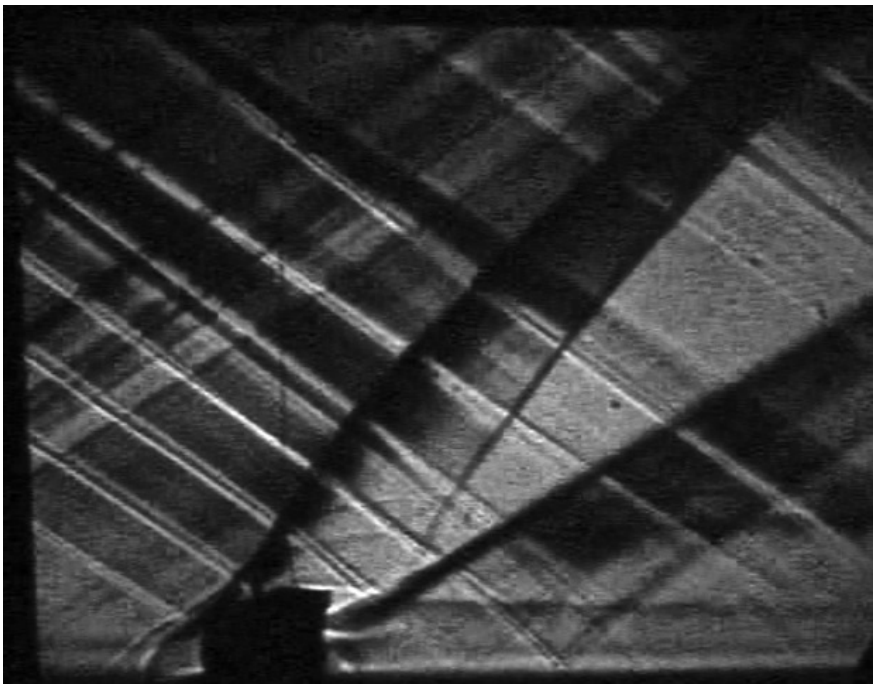

Figure 90. Test Configuration 4a: Rod with Cavity – Schlieren Photograph

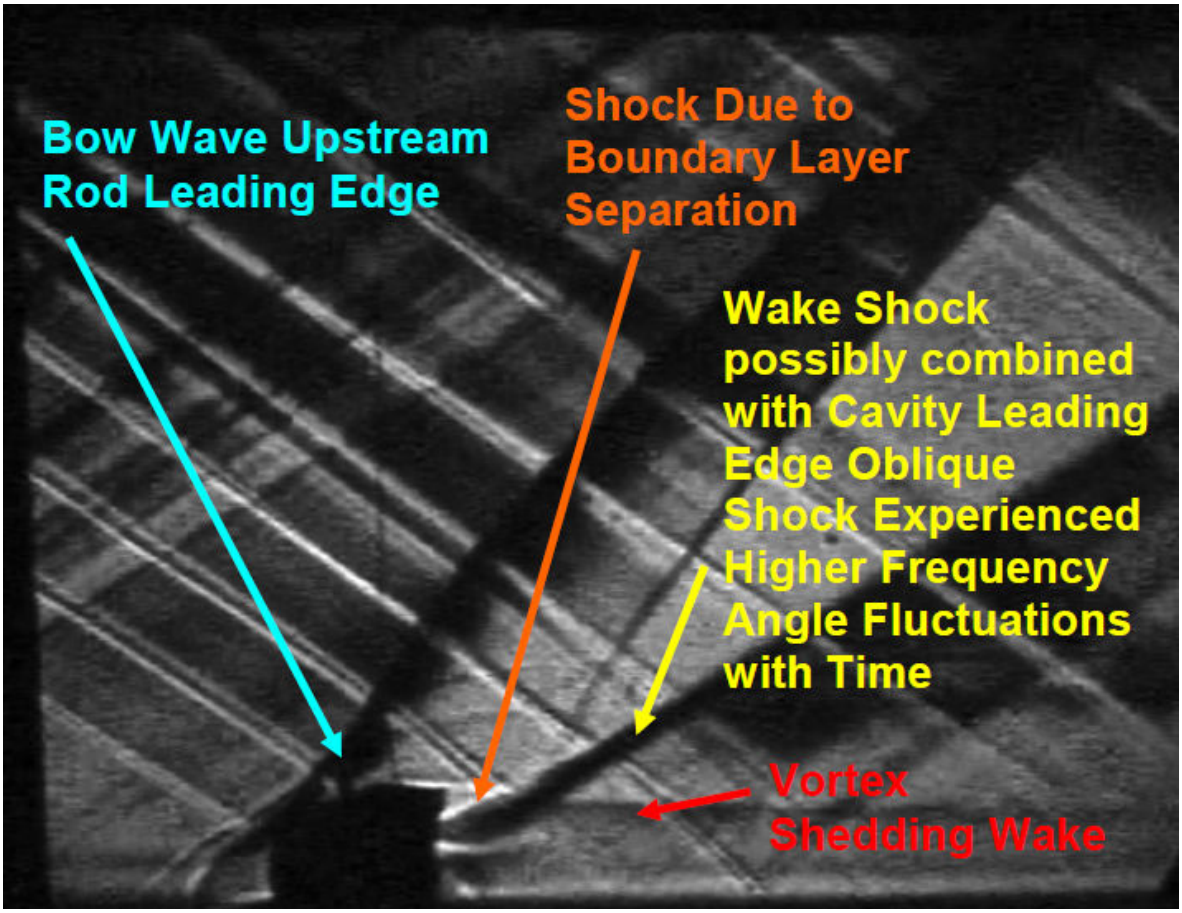

Figure 91. Test Configuration 4a: Rod with Cavity – Schlieren Analysis

PIV was applied to the rod with cavity configuration to see how the rod influenced the cavity spanning shear layer. Figure 92 includes a normalized velocity plot averaged over 50 frames of PIV data. The plot shows a reduction of velocity immediately over the cavity region. Of interest, the cavity flow research completed by Loewen [5] in 2008 provided results illustrating how the rod in crossflow technique provided a lofting effect on the shear layer to reduce trailing edge interactions within the cavity. The results of the present study could not provide detection of a lofting effect because of the limited field of view available for PIV over the cavity length.

Figure 93 includes the averaged vorticity contour plot for the rod with cavity. Unlike the Figure 85 averaged vorticity plot for the baseline cavity, there was no well defined (dark blue line) region of vorticity spanning the viewable cavity length. This observation could provide support that the rod in crossflow technique may actually diffuse the vorticity of the cavity spanning shear layer causing it to break down faster as it reaches the cavity trailing edge. Unfortunately, this can still not be verified without direct PIV testing of the cavity trailing edge flow field.

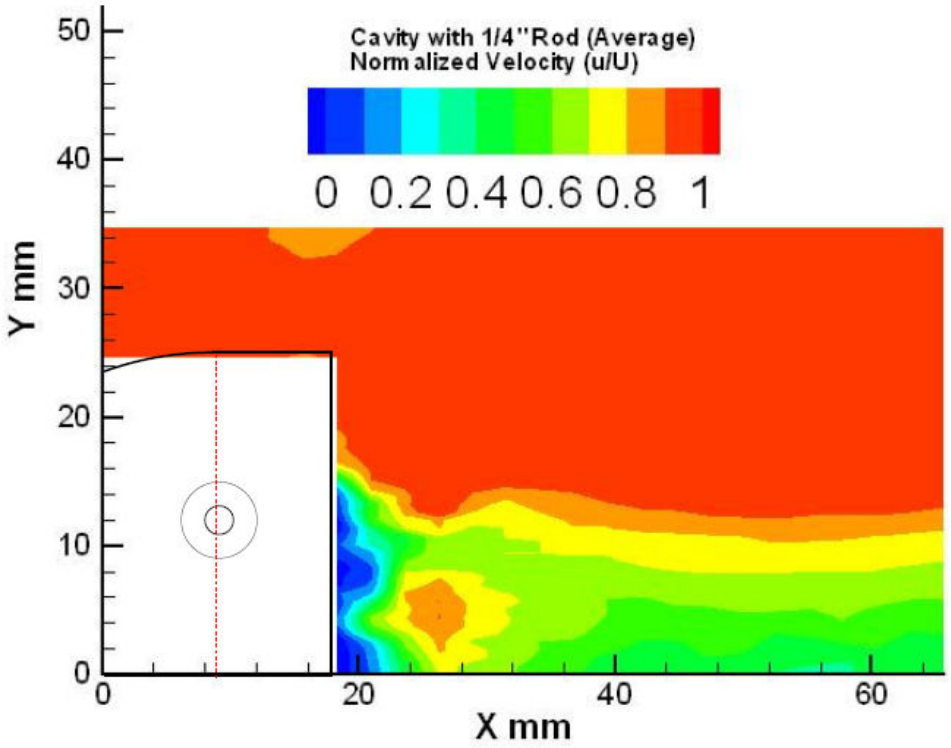

Figure 92. Test Configuration 4a: Rod with Cavity Average Velocity Contour Plot

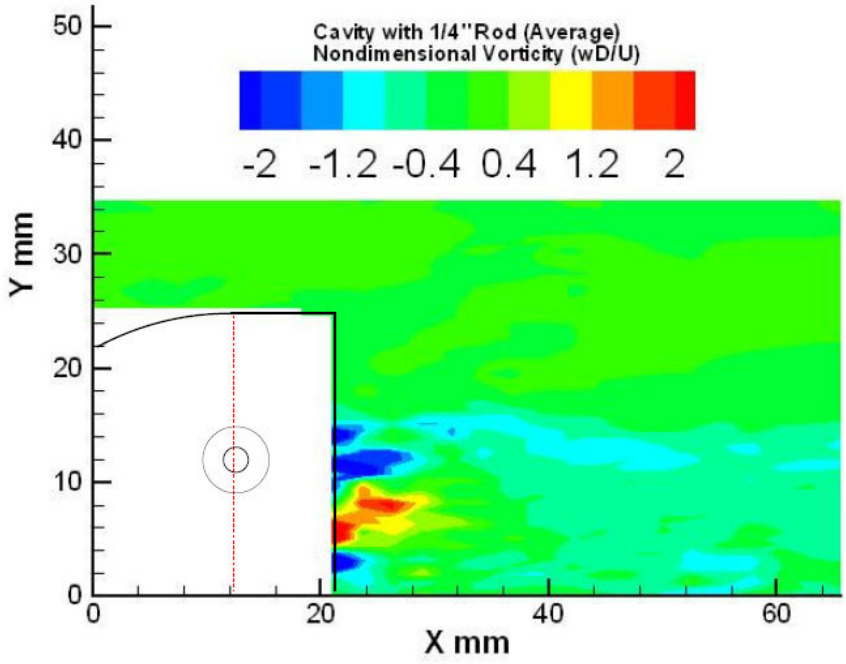

Figure 93. Test Configuration 4a: Rod with Cavity Average Vorticity Contour Plot

Figure 94 includes two instantaneous snapshots of velocity and vorticity contour plots. The images were included purely to show the time dependent nature of the rod with cavity configuration. The instantaneous velocity contour plot images did not vary significantly from the averaged velocity contour plot since all images showed roughly the same velocity decreases behind the rod. However, the instantaneous velocity images did indicate small fluctuations within the rod wakes which may have been a result of vortex shedding. The instantaneous vorticity results indicated well defined regions of vorticity downstream of the rod amongst regions or virtually no vorticity. Like the average vorticity plot, there was no continuous (dark blue line) region of vorticity going across the viewable cavity length (such as was the case for the baseline cavity near y = 0 mm). This showed agreement for both the instantaneous and average vorticity plots to support that the rod may actually have diffused the cavity spanning shear layer. Overall, the rod with cavity PIV results show that there is still a requirement to test the cavity trailing edge interactions to better understand the mechanism behind the technique's ability to suppress tones. However, the instantaneous results did provide results to support that vortex shedding had occurred.

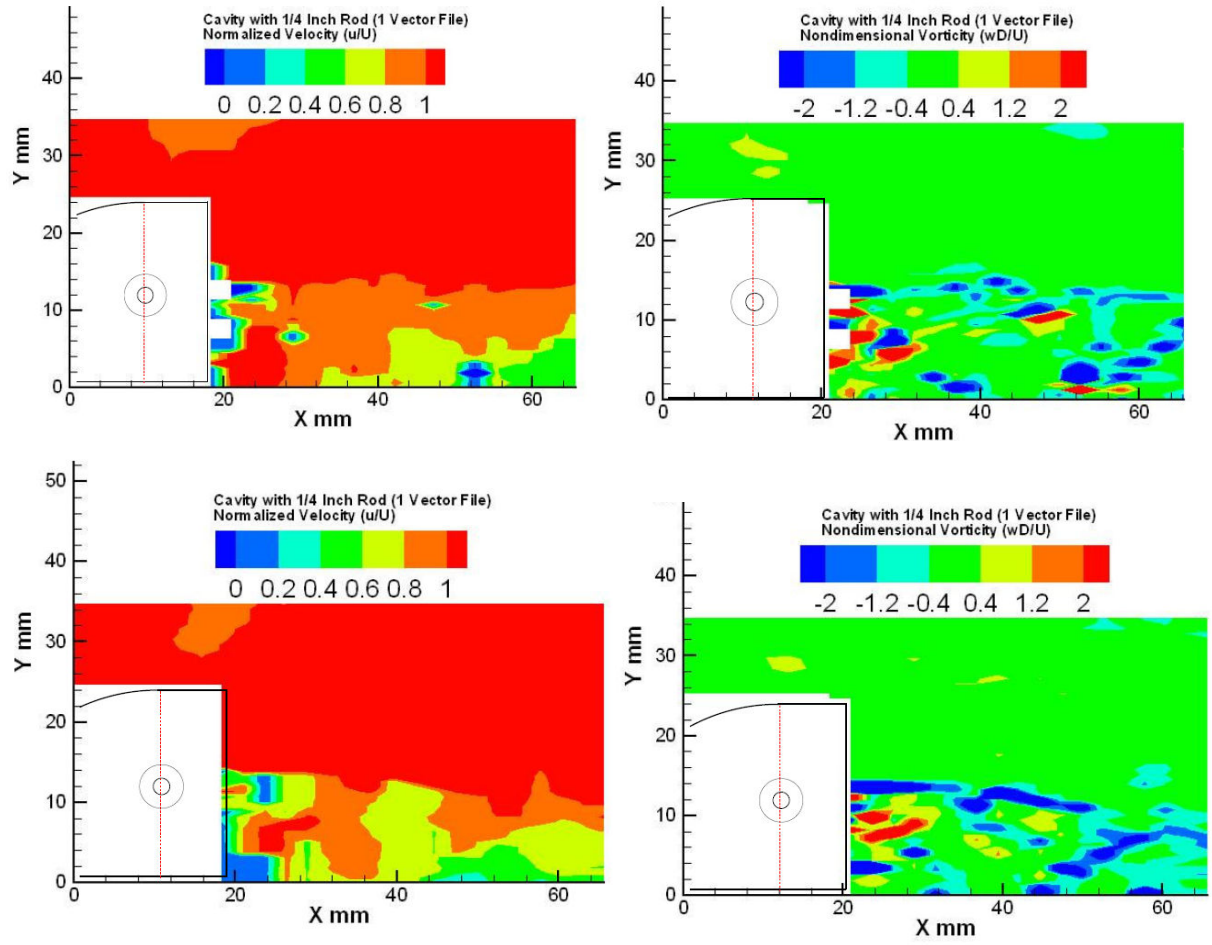

Figure 94. Test Configuration 4a: Rod with Cavity Instantaneous Contour Plots of Velocity (left) and Vorticity (right)

Test Configuration 4b: Airfoil 0^{o} Angle of Attack with Cavity

The acoustic spectrum for the 0 degree airfoil with cavity is included within Figure 95. The results of the test were compared with the baseline cavity in Table 10. Over the frequency range of 0 to 5000 Hz, the broadband noise was 134 dB. This was a reduction of only 1 dB from the baseline cavity broadband noise of 135 dB and may be attributed to experimental error. The observed first three mode resonant tone frequencies of 455 Hz, 942 Hz and 1562 Hz were within 10% of those for the baseline cavity. The forth mode resonant tone frequency could not be deduced from the spectrum data. The second mode peak amplitude was reduced by 4.0 dB but remained very well defined. The largest peak amplitude reduction was 6.5 dB for third mode.

Figure 96 includes a Schlieren photograph of the 0 degree angle of attack airfoil with the cavity while Figure 97 depicts the analysis of its flow structure. The airfoil exhibited a detached bow wave upstream of its rounded leading edge similar to the airfoil with solid floor configurations. The trailing edge of the airfoil included oblique shocks on both the top and bottom surfaces which both appeared to interact and deflect the angle of the cavity leading edge oblique shock.

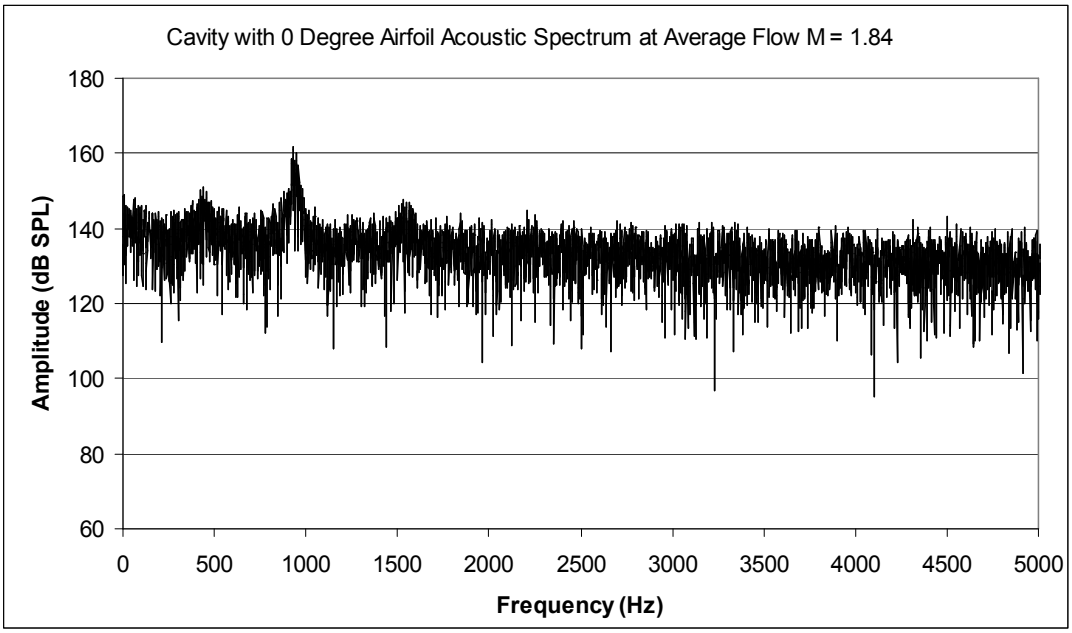

Figure 95. Configuration 4b: Airfoil 0^{o} with Cavity – Acoustic Spectrum

Table 10: Airfoil 0^o with Cavity Compared with Baseline Cavity Acoustic Spectrum

Mode , m	Side Plates with Cavity Resonant Tone Frequencies *f*	Side Plates with Cavity Peak Amplitudes	Baseline Cavity Resonant Tone Frequencies *f*	Baseline Cavity Peak Amplitudes	Variation from Baseline Cavity Tone Frequencies *df*	Reduction from Baseline Cavity Peak Amplitudes
-	Hz	db SPL	Hz	db SPL	Hz	db SPL
1	455	149.7	414	151.6	41	1.9
2	942	160.3	967	164.3	-25	4.0
3	1562	147.1	1519	153.6	-6.5	6.5
4	n/a	n/a	2071	157.7	n/a	n/a

Figure 96. Test Configuration 4b: Airfoil 0^o with Cavity – Schlieren Photograph

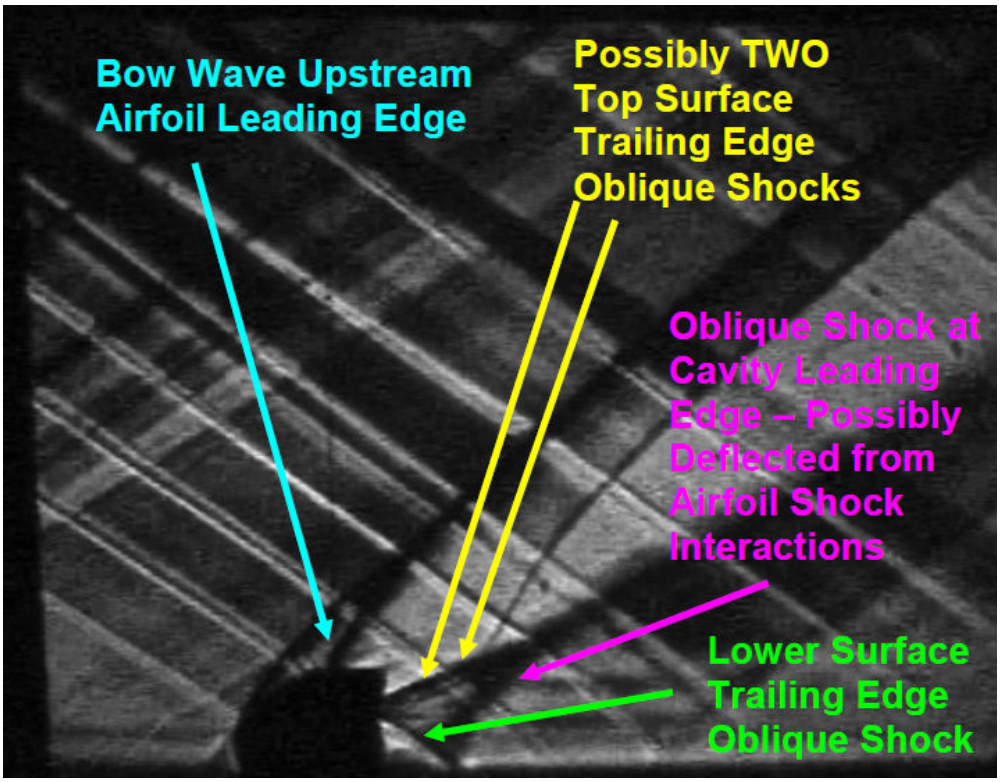

Figure 97. Test Configuration 4b: Airfoil 0^o with Cavity – Schlieren Analysis

The averaged velocity contour plot for the 0 degree angle of attack airfoil with the cavity is presented within Figure 98. Of interest, the INSIGHT PIV software was unable to correlate vectors in a region downstream of the airfoil and for a region to the lower right of the side plates. This poor correlation was not realized until after the test program was completed. The regions without vector correlation may have resulted from poor seeding uniformity within the direct wake of the airfoil. Another contributing factor may have been laser light access issues within the region directly under the trailing edge of the airfoil. The result of the zero correlation regions were two large white spaces on Figure 98. Of interest, the bottom right hand side region of the plot indicated a lower speed flow region over the cavity.

Figure 99 includes the averaged vorticity contour plot for the 0 degree angle of attack airfoil with the cavity configuration. Like Figure 98, this plot was impacted by poor vector correlation

which caused regions to have no data available to present. The flow field does however show reversed vorticity between the upper and lower airfoil surface wakes. This was a strong indication that flow separation occurred for the airfoil for even the 0 degree angle of attack case. The vorticity contours near y = 0 provide interesting information relevant to the shock interactions illustrated within the Schlieren imagery of Figures 95 and 96. The poor vector correlation appeared to have occurred upstream and downstream of the shock that originated from the airfoil lower surface trailing edge which was directed within the cavity region. In addition, the plot indicates a well defined (dark blue line) region of vorticity spanning the viewable cavity length downstream of where the oblique shock would have occurred. The results of the vorticity plot along with the Schlieren data could provide support to that the cavity spanning shear layer was likely offset from the lower airfoil oblique shock rather than significantly diffused.

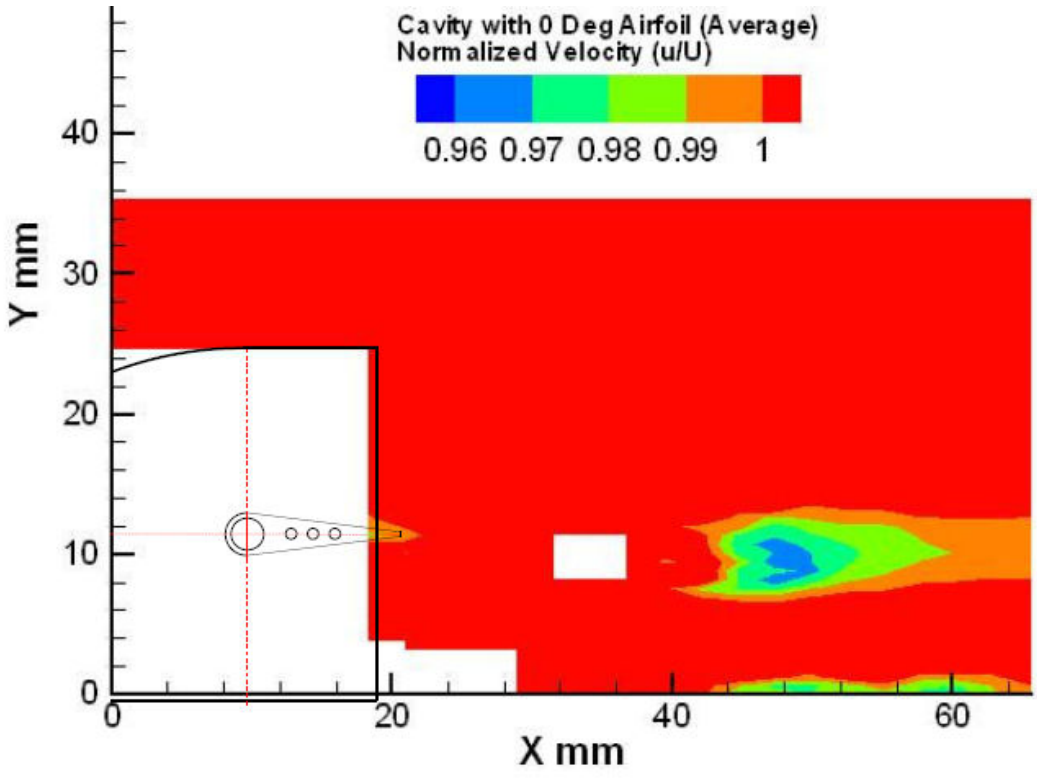

Figure 98. Test Configuration 4b: Airfoil 0° with Cavity Average Velocity Contour Plot

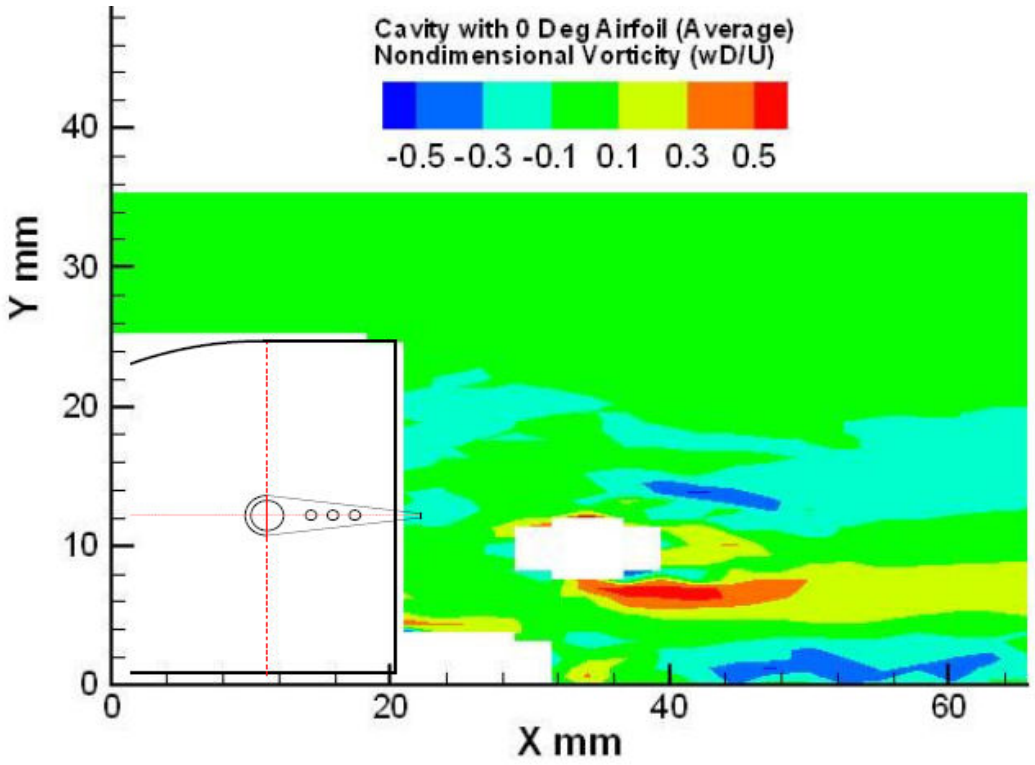

Figure 99. Test Configuration 4b: Airfoil 0^{o} with Cavity Average Vorticity Contour Plot

Test Configuration 4c: Airfoil -5^{o} Angle of Attack with Cavity

The acoustic spectrum for the -5 degree airfoil with cavity configuration is included within Figure 100. The results of the test were summarized and compared with the baseline cavity in Table 11. Over the frequency range of 0 to 5000 Hz, the broadband noise was 131 dB. This was a reduction of 4 dB from the baseline cavity broadband noise of 135 dB. The observed first, second and third mode resonant tone frequencies of 482 Hz, 931 Hz and 1512 Hz were within 17% of those for the baseline cavity. The 4th mode resonant tone frequency could not be deduced from the spectrum data. The 2nd mode peak amplitude was reduced by 5.8 dB but remained very well defined. The most significant peak amplitude reduction was 6.0 dB for 3rd Mode.

Figure 101 includes a Schlieren photograph of the -5 degree angle of attack airfoil with the cavity configuration while Figure 102 depicts the analysis of its flow structure. As was the case with the 0 degree angle of attack airfoil, -5 degree airfoil also exhibited a detached bow wave at

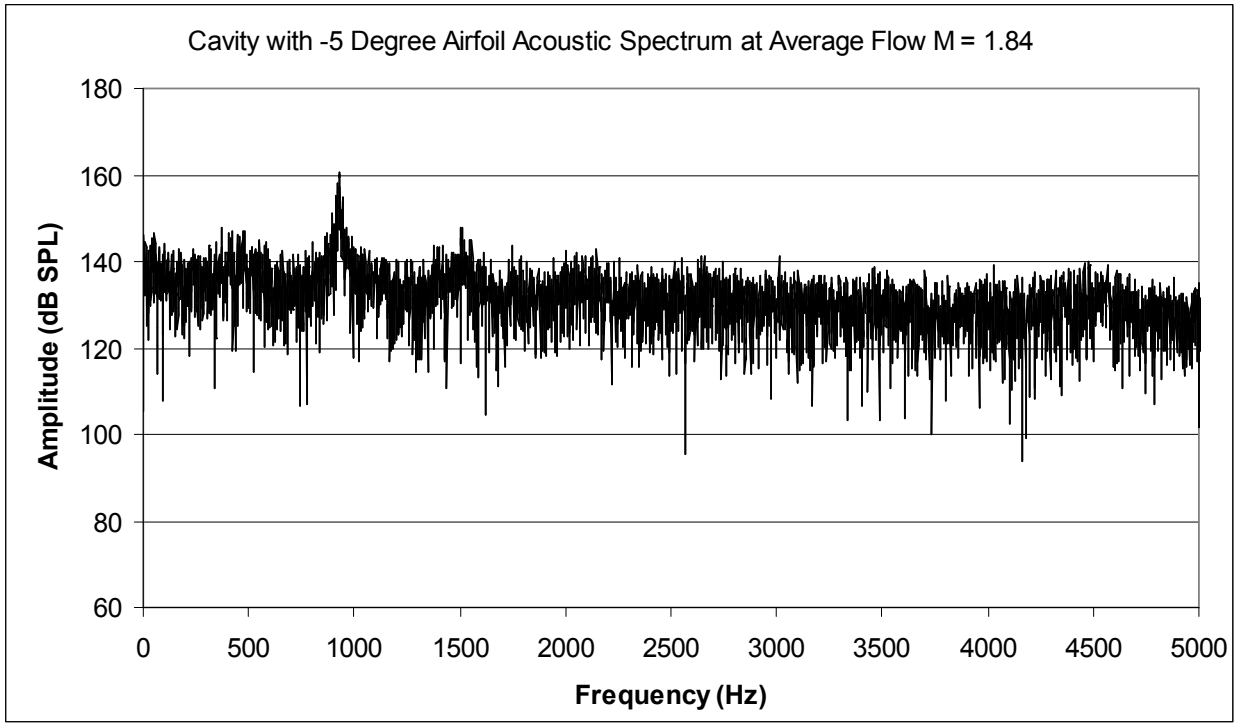

Figure 100. Configuration 4b: Airfoil -5^o with Cavity – Acoustic Spectrum

Table 11: Airfoil -5^o with Cavity Compared with Baseline Cavity Acoustic Spectrum

Mode , m	Side Plates with Cavity Resonant Tone Frequencies *f*	Side Plates with Cavity Peak Amplitudes	Baseline Cavity Resonant Tone Frequencies *f*	Baseline Cavity Peak Amplitudes	Variation from Baseline Cavity Tone Frequencies *df*	Reduction from Baseline Cavity Peak Amplitudes
-	Hz	db SPL	Hz	db SPL	Hz	db SPL
1	482	147.2	414	151.6	68	4.4
2	931	158.5	967	164.3	-36	5.8
3	1512	147.6	1519	153.6	-7	6.0
4	n/a	n/a	2071	157.7	n/a	n/a

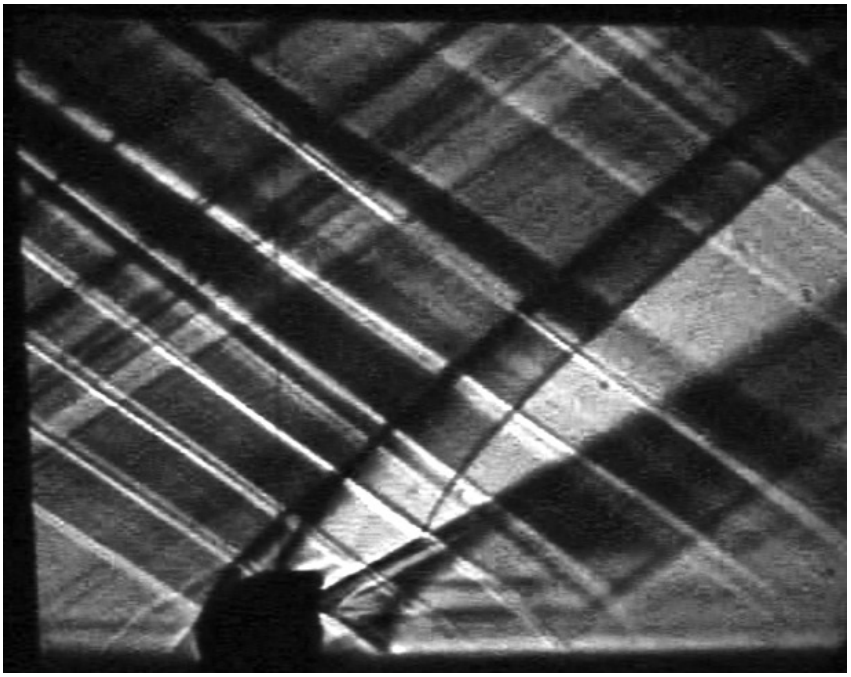

Figure 101. Test Configuration 4b: Airfoil -5^{o} with Cavity – Schlieren Photograph

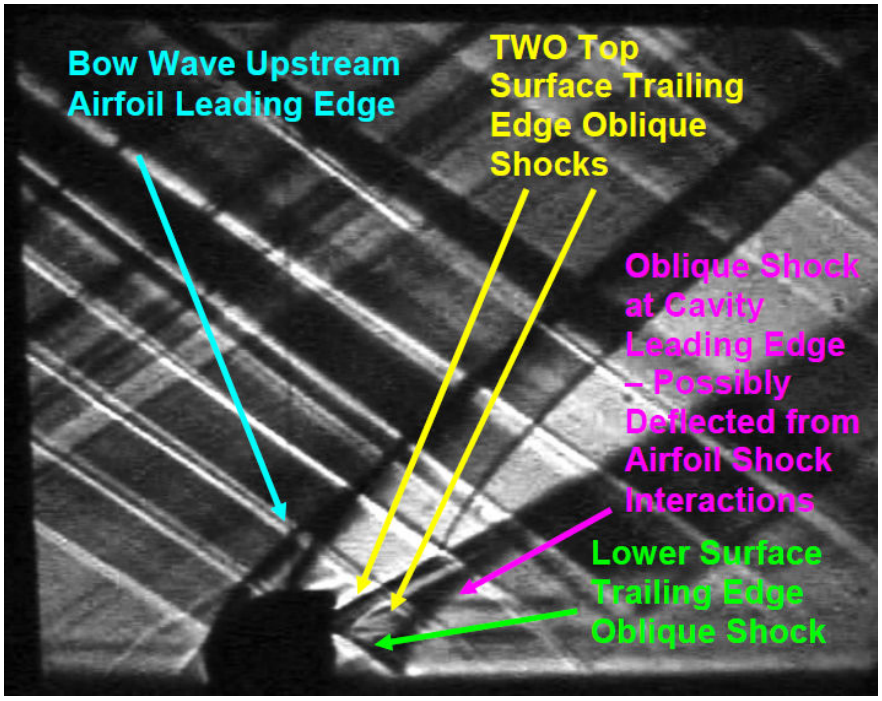

Figure 102. Test Configuration 4b: Airfoil -5^{o} with Cavity – Schlieren Analysis

its rounded leading edge. Two oblique shocks can be viewed from the airfoil upper surface. It was interpreted that the oblique shock upstream of the trailing edge was a result of flow separation. Both of the top surface oblique shocks appeared to merge downstream of the airfoil. The shocks from the trailing edge of the airfoil upper and lower surfaces appeared to have contributed to the deflection of the cavity leading edge oblique shock.

Figure 103 shows the averaged velocity contour plot for the -5 degree angle of attack airfoil with the cavity. The overall vector correlation of the PIV data was superior to the 0 degree angle of attack test. However, there was a small region of poor correlation to the lower right of the side plates as shown by the white region depicted within Figure 103. The bottom right hand side region of the plot also indicated a lower speed flow region over the cavity.

Figure 104 includes the averaged vorticity contour plot for the -5 degree angle of attack airfoil with the cavity. Similar to the 0 degree case, this test indicated flow separation from the trailing edge vorticity structure. The bottom right hand side region of the plot did show indications of a cavity shear layer region by the faint blue line present. However, the shear layer appeared to be less defined for this case when compared with the 0 degree angle of attack configuration.

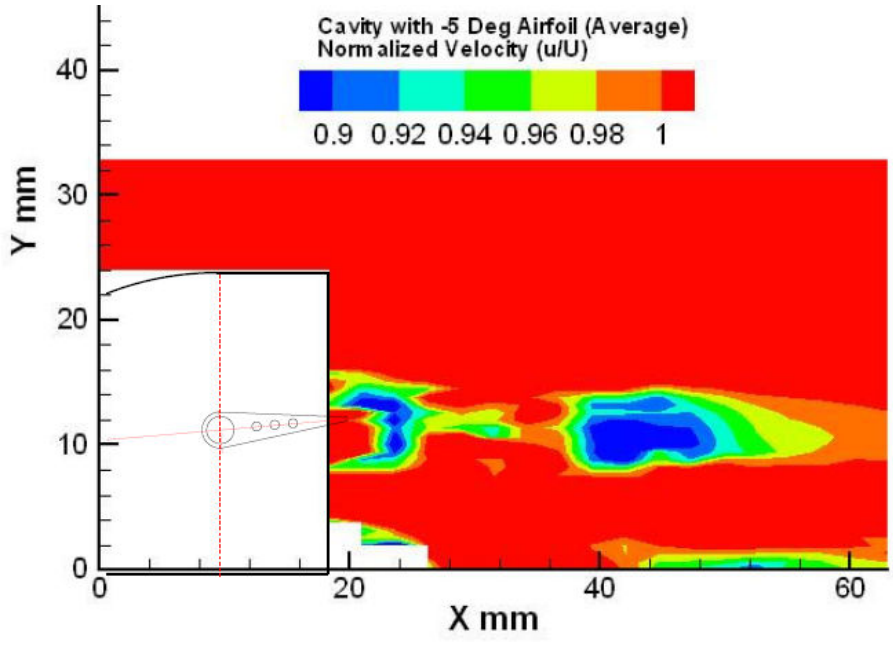

Figure 103. Test Configuration 4b: Airfoil -5^{o} Average Velocity Contour Plot

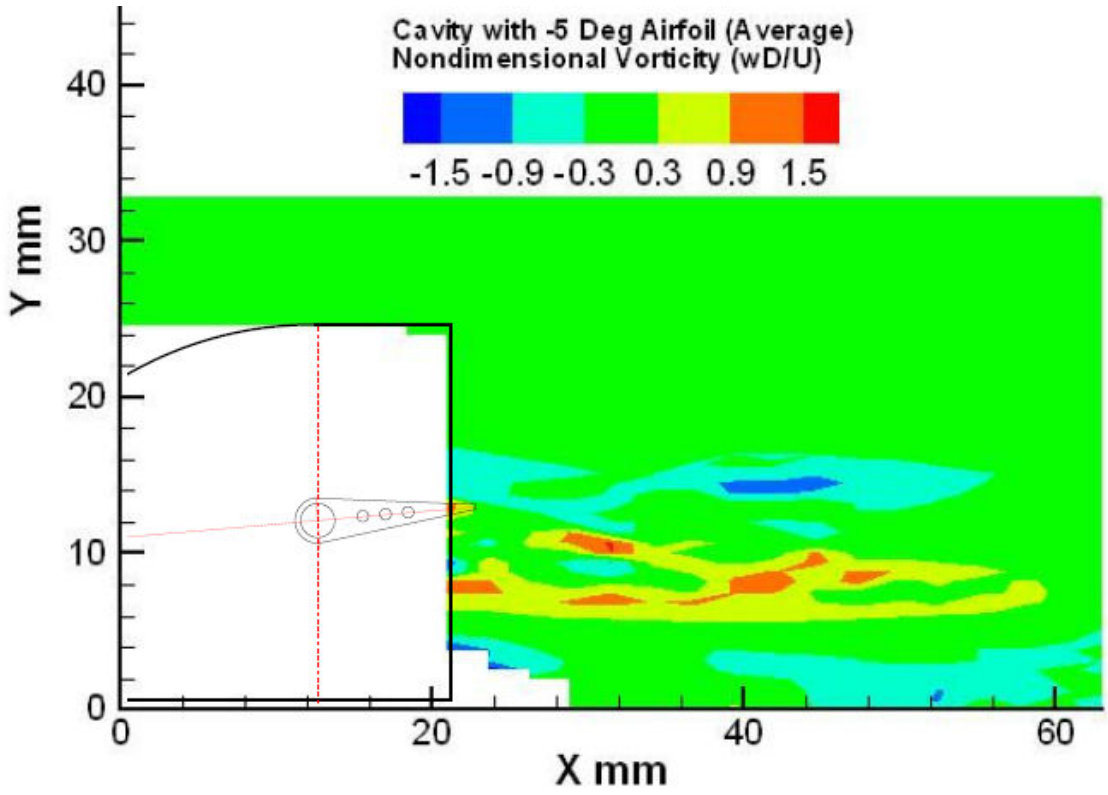

Figure 104. Test Configuration 4b: Airfoil -5^{o} Average Vorticity Contour Plot

Test Configuration 4d: Airfoil -10^{o} Angle of Attack with Cavity

The acoustic spectrum for the -10 degree airfoil with cavity configuration is included within Figure 105. The results of the test were summarized and compared with the baseline cavity in Table 12. Over the frequency range of 0 to 5000 Hz, the broadband noise was 130 dB. This was a reduction of 5 dB from the baseline cavity broadband noise of 135 dB. The observed first, second and third mode resonant tone frequencies of 473 Hz, 918 Hz and 1482 Hz were within 14% of those for the baseline cavity. The forth mode resonant tone frequency could not be deduced from the spectrum data. The second mode peak amplitude was reduced by 5.7 dB but remained very well defined. The most significant peak amplitude reduction was 9.1 dB for third mode.

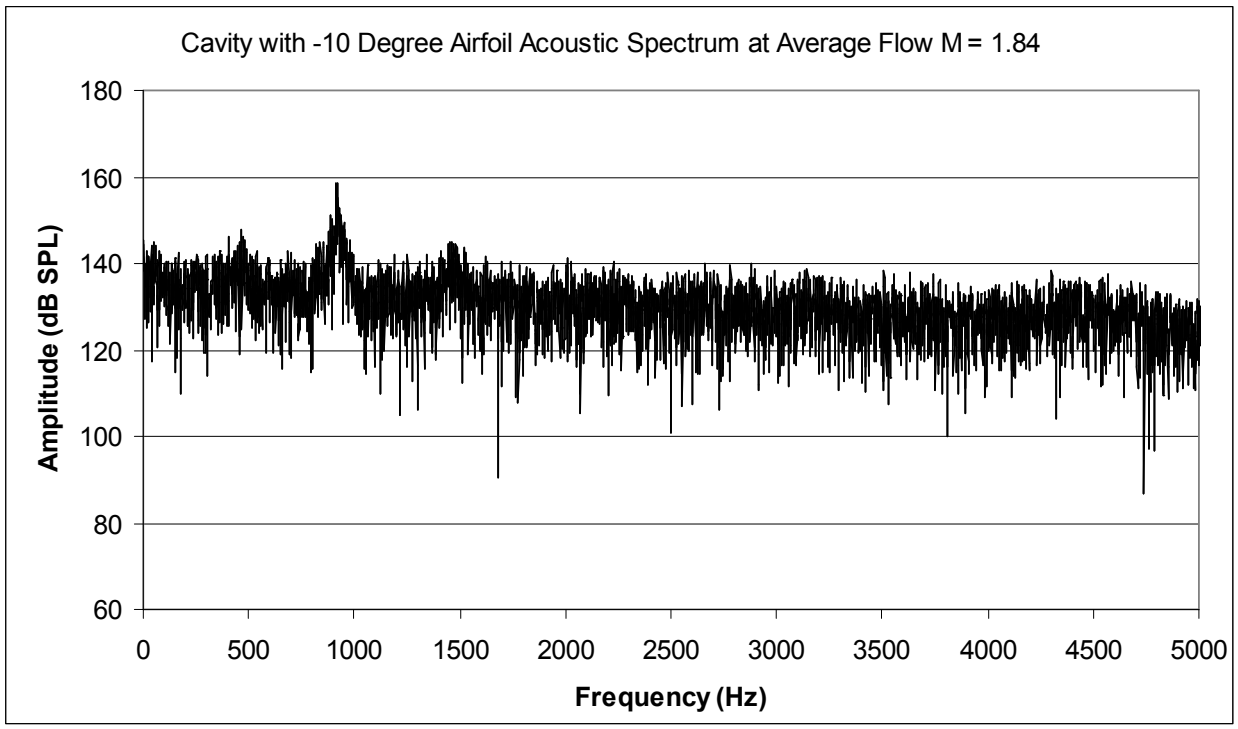

Figure 105. Configuration 4b: Airfoil -10^{o} with Cavity – Acoustic Spectrum

Table 12: Airfoil -10^{o} with Cavity Compared with Baseline Cavity Acoustic Spectrum

Mode , m	Side Plates with Cavity Resonant Tone Frequencies *f*	Side Plates with Cavity Peak Amplitudes	Baseline Cavity Resonant Tone Frequencies *f*	Baseline Cavity Peak Amplitudes	Variation from Baseline Cavity Tone Frequencies *df*	Reduction from Baseline Cavity Peak Amplitudes
-	Hz	db SPL	Hz	db SPL	Hz	db SPL
1	473	146.1	414	151.6	59	5.5
2	918	158.6	967	164.3	49	5.7
3	1482	144.5	1519	153.6	37	9.1
4	n/a	n/a	2071	157.7	n/a	n/a

Figure 106 includes a Schlieren photograph of the -10 degree angle of attack airfoil with the cavity configuration while Figure 107 depicts the analysis of the flow structure. As was the case with the 0 and -5 degree angle of attack airfoils, -10 degree airfoil also exhibited a detached bow wave at its rounded leading edge. Within this image, two oblique shocks can be viewed from the upper surface of the airfoil. It was interpreted that the oblique shock upstream of the trailing edge was a result of flow separation. The top surface oblique shocks did not merge into a single shock for this configuration. The shocks from the airfoil lower surface and top surface trailing edge appear to have both interacted and deflected the angle of the cavity leading edge oblique shock.

The averaged velocity contour plot for the -10 degree angle of attack airfoil with the cavity is shown within Figure 108. It must be noted that the color scale was reset for this image only for the purpose of showing better contrast with the normalized velocity. Alternatively it could be stated that although the airfoil has a very large wake structure, the majority of the flow remains at roughly above 90% of the freestream velocity. Similar to the other airfoil configurations, the bottom right hand side region of the plot also indicated a lower speed flow region over the cavity.

Figure 108 includes the averaged vorticity contour plot for the -10 degree angle of attack airfoil with the cavity. Similar to the 0 and -5 degree angle of attack cases, this configuration also indicated flow separation based on the vorticity structure at the airfoil trailing edge. However, it appears that the flow separation is of larger magnitude for this test. The bottom right hand side region of the plot did show strong indications of a cavity shear layer region by the well defined dark blue line present. It was anticipated that the dark blue line was divided across the field of view shown within the figure only because of the airfoil trailing edge oblique shock being directed into the cavity.

Figure 110 include a chart that summarizes the sound pressure levels of the peak amplitudes and broad band noise averages for the various cavity configurations. The chart clearly shows that the rod provided the best acoustic suppression followed by the -10 degree airfoil.

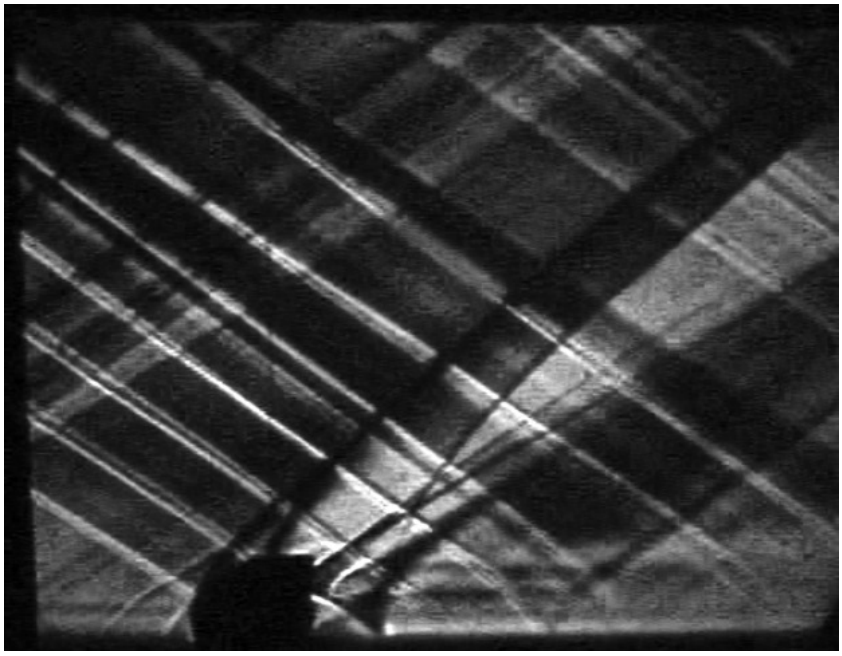

Figure 106. Test Configuration 4b: Airfoil -10^{o} with Cavity – Schlieren Photograph

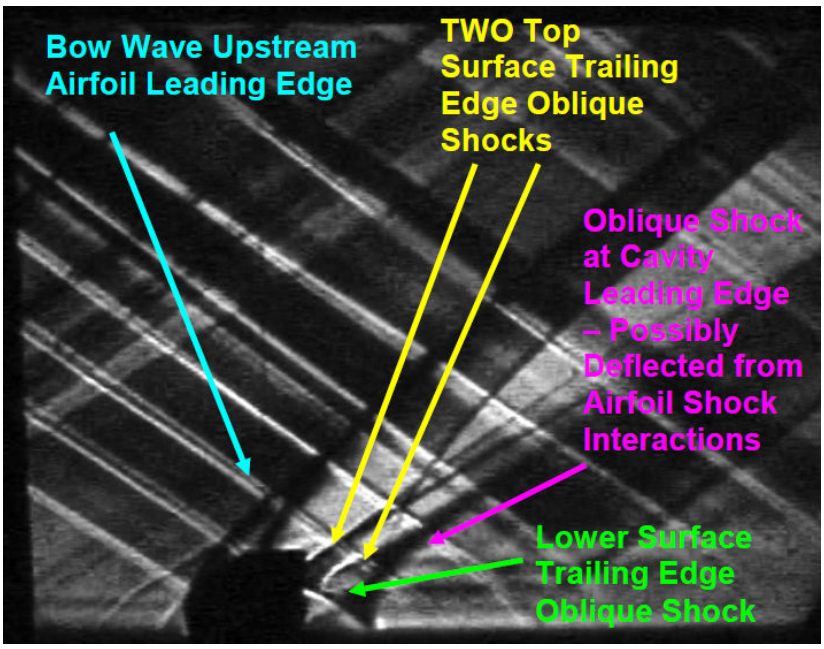

Figure 107. Test Configuration 4b: Airfoil -10^{o} with Cavity – Schlieren Analysis

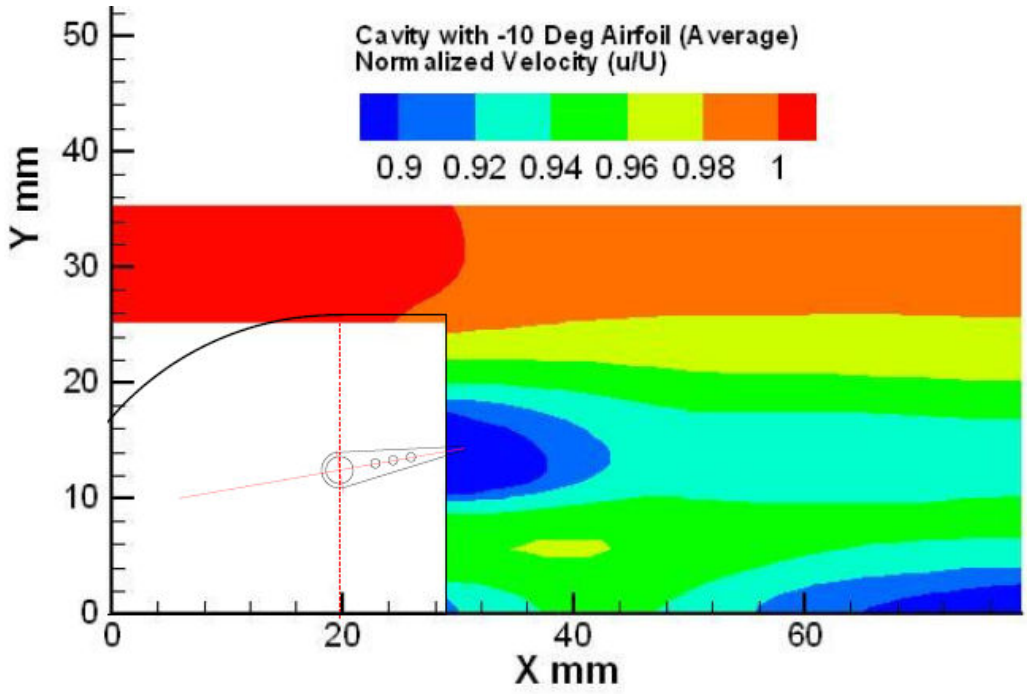

Figure 108. Test Configuration 4b: Airfoil -10^{o} Average Velocity Contour Plot

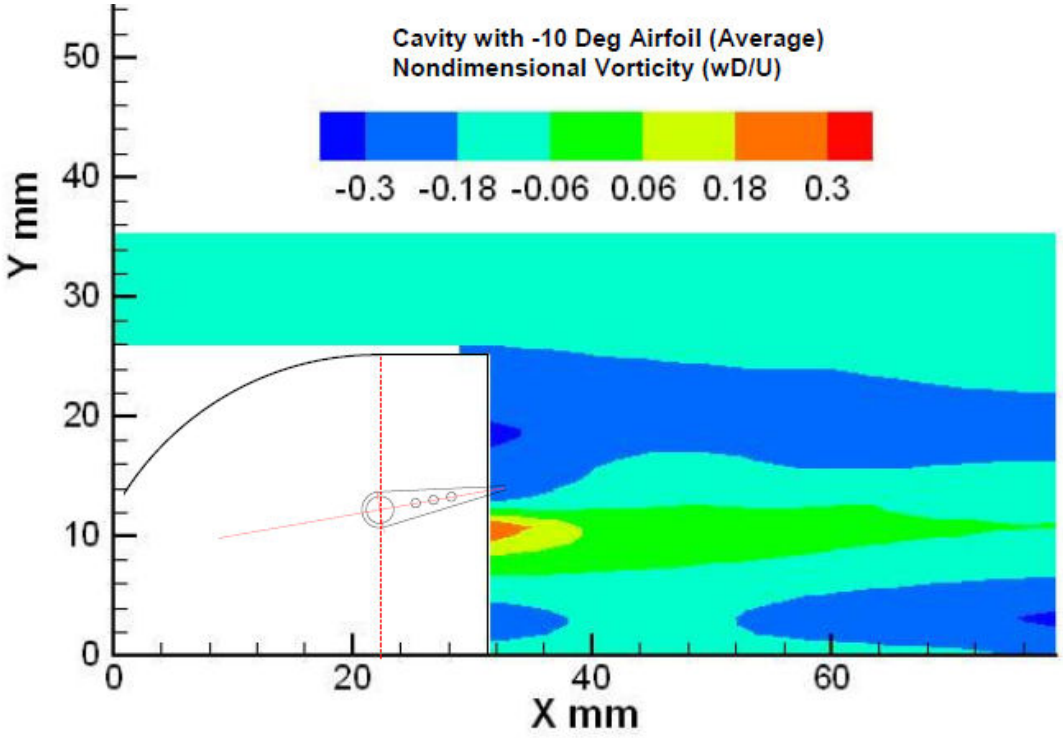

Figure 109. Test Configuration 4b: Airfoil -10^{o} Average Vorticity Contour Plot

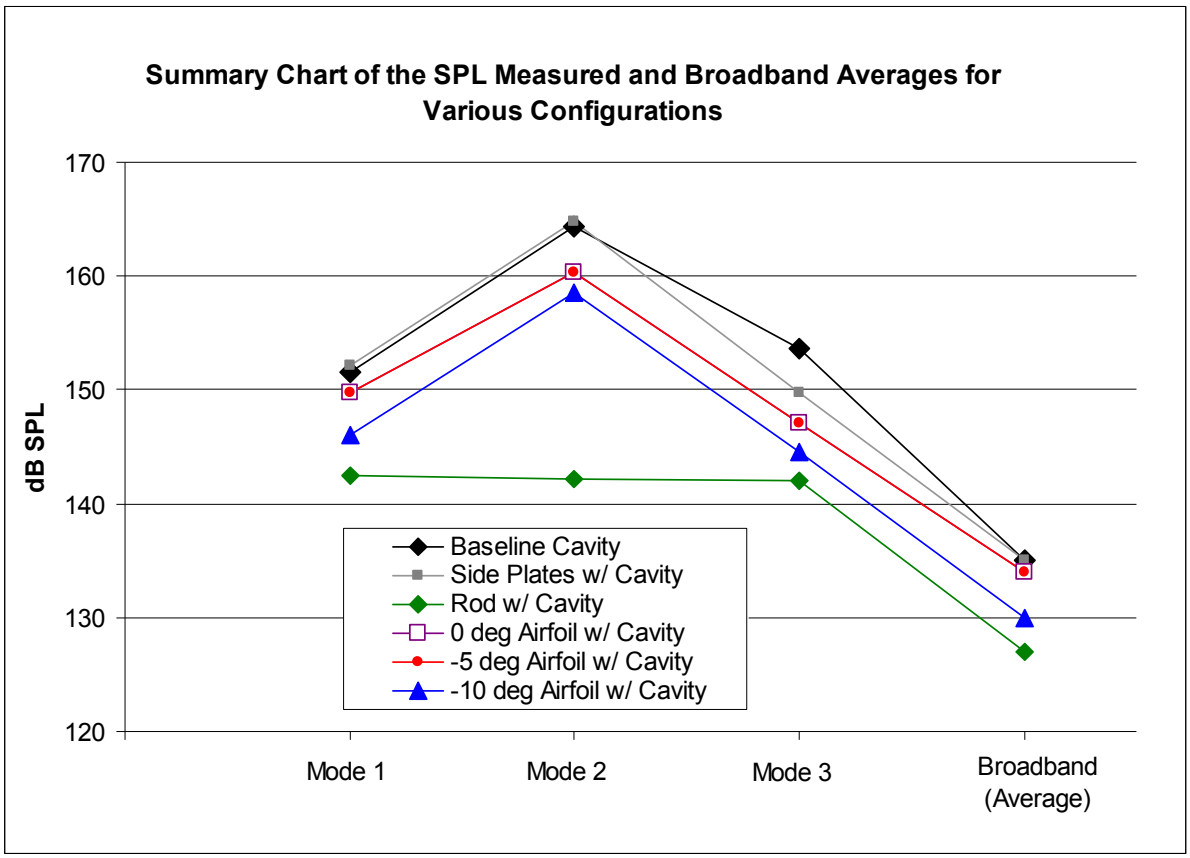

Figure 110. Summary of Sound Pressure Levels for the Peak Amplitudes and Broadband Noise Averages for the Various Cavity Configurations

Chapter 5

CONCLUSIONS AND RECOMMENDATIONS

Conclusions

The effects of an airfoil at different angles of attack and a circular cylindrical rod within the edge of the boundary layer flow at the leading edge of a cavity as a device for controlling the large pressure fluctuations (resonance tones) in the cavity were investigated. The airfoil results were compared with the rod in crossflow method positioned at the same leading edge location. The cavity used for testing corresponded to a length to depth ratio, L/D of 11.0/2.25 with a length to width ratio, L/W of 11.0/3.00 at a freestream Mach 1.84 flow. The study included measurements of dynamic pressure transducer output at 40 kHz and Frequency Spectra calculations, Schlieren flow visualization techniques for shock wave structures with velocity and vorticity fields obtained from PIV measurements. Analysis of the investigation results led to the following conclusions:

1. All airfoil configurations experienced flow separation to varying degrees. The negative 10 degree angle of attack configuration experienced the greatest amount of flow separation.

2. All airfoil configurations provided varying degrees of cavity (resonant) tone suppression. Of the airfoil configurations tested, the negative 10 degree configuration airfoil provided the best noise suppression with a 5 dB SPL reduction in broadband noise and a 9 dB reduction in peak amplitude for the 3rd resonant mode.

3. Although all the airfoil configurations provided various levels of noise suppression, none of the configurations performed to the level of the rod in crossflow technique which provided a 8 dB SPL reduction in broadband noise and a 22 dB reduction in peak amplitude for the 2nd resonant mode.

4. No indications of flow lofting effects could be studied with any of the configurations tested. Lofting effect testing would have required flow field visualization of the cavity trailing edge region.

5. No measurement of the rod vortex shedding frequency could be detected. Because PIV results showed strong indication of vortex shedding, the lack of vortex shedding frequency data was attributed to the dynamic pressure transducer being located a distance of 44 rod diameters downstream of the rod location.

6. All airfoil test configurations showed evidence of deflections to the cavity leading edge oblique shock wave. The mechanisms of the deflection were the airfoil trailing edge shocks interacting with the cavity leading edge shock.

7. The rod in crossflow technique showed evidence of diffusing the cavity spanning shear layer within the field of view tested.

.

Recommendations

Future cavity flow testing should include the use of an additional dynamic pressure transducer placed close downstream of any leading edge flow control devices.

Further cavity flow research with airfoils at Mach 1.84 should include the testing of a diamond shaped airfoil and possibly a contoured airfoil with camber to avoid flow separation.

Future testing should be completed at a variety of positions within the boundary layer upstream of the cavity leading edge for the purpose of determining an optimum position.

List of References

List of References

1. Chen, C.H., "Study of Subsonic and Transonic Flow Separation – With and Without Upstream Disturbances," Ph. D. Dissertation, University of Tennessee, Knoxville, TN, 1975.

2. Tam, C.K.W., and Block, P.J.W., "On the Tones and Pressure Oscillations Induced by Flow Over Rectangular Cavities," Journal of Fluid Mechanics, Vol. 89, Part 2, 1978, pp. 373 – 399.

3. Plentovich, E.B., Stallings, R.L., and Tracy, M.B., "Experimental Cavity Pressure Measurements at Subsonic and Supersonic Speeds," NASA Technical Paper 3358, 1993.

4. Cattafesta III, L.N., Williams, D.R., Rowley, C.W., and Farrukh, S.A., "Review of Active Control of Flow-Induced Cavity Resonance," 33rd AIAA Fluid Dynamics Conference and Exhibit, AIAA 2003-3567, 2003

5. Loewen, R.D., "Analysis of Cavity Flow and the Effects of a Rod in Crossflow," M.Sc Thesis, University of Tennessee, Knoxville, TN, Dec. 2008.

6. Tracy, B.T., and Plentovich, E.B., "Cavity Unsteady-Pressure Measurements at Subsonic and Transonic Speeds," NASA Technical Paper 3669, Dec.1997.

7. Radhakrishnan, S., "An Experimental and Numerical Study of Open Cavity Flows," Ph. D Dissertation, University of Tennessee, Knoxville, TN, May 2002.

8. Karamcheti, K., "Acoustic Radiation from Two-Dimensional Rectangular Cutouts in Aerodynamic Surfaces," NACA TN 3487, Aug. 1955.

9. Roshko, A., "Some Measurements of Flow in a Rectangular Cutout," NACA TN 3488, Aug. 1955.

10. Rossiter, J.E., "Wind Tunnel Experiments on the Flow over Rectangular Cavities at Subsonic and Transonic Speeds," Aeronautical Research Council R. & M. No. 3438, Oct. 1964.

11. Heller, H.H., Holmes, D.G., and Covert, E.E., "Flow Induced Pressure Oscillations in Shallow Cavities," Journal of Sound and Vibrations 18(4) , Apr. 1971, pp. 545 –553.

12. Heller, H.H. and Bliss, D.B., "The Physical Mechanism of Flow-Induced Pressure Fluctuations in Cavities and Concepts for their Suppression," AIAA Paper 75 – 491, AIAA 2nd Aero-Acoustics Conference, Hampton, VA., Mar. 24 – 26, 1975.

13. Clarke, R.L., "Evaluation of F-111 Weapon Bay Aero-Acoustic and Weapon Separation Improvement Techniques," AFFDL-TR-79-3003, Feb. 1979.

14. Benson, T., "Shape Effects on Drag," NASA Glenn Research Center, http://www.grc.nasa.gov/WWW/K-12/airplane/shaped.html

15. Vakili, A.D., and Gauthier, C., "Control of Cavity Flow by Upstream Mass Injection," AIAA Journal of Aircraft, Vol.31, No.4, Jan. – Feb. 1994.

16. Wiltse, J.M., and Glezer, A., "Direct Excitation of Small-Scale Motions in the Free Shear Layer." Physics of Fluids, Vol. 10, No. 8, 2026 – 2036, 1998

17. Stanek, M.J., Raman, G., Ross, J.A., Odedra, J., Peto, J., Alvi, F. and Kibens, V., "High Frequency Acoustic Suppression – The Role of Mass Flow, The Notion of Superposition, and the Role of Inviscid Instability – A New Model (Part II)." 8th AIAA/CAES Aeroacoustics Conference & Exhibit, AIAA 2002-2404, Jun. 17-19, 2002.

18. Stanek, M. J., Ross, J. A., Odera, J. and Peto, J., "High Frequency Acoustic Suppression – The Mystery of the Rod-in-Crossflow Revealed," AIAA Paper 2003-0007, 2003.

19. Franke, M.E., Carr, D.L. "Effect of Geometry on Open Cavity Flow – Induced Pressure Oscillations," 2nd AIAA Aero-Acoustics Conference, AIAA 75-492, Mar. 24-26, 1975

20. Meganathan, A.J., "An Experimental Study of Low Speed Open Cavity Flows," M.Sc Thesis, University of Tennessee, Knoxville, TN, Dec. 2000.

21. Smith, B.R., Welterlen, T.J., Maines, B.H., Shaw, L.L., Stanek, M.J., Grove, J.E., "Weapons Bay Acoustic Suppression from Rod Spoilers," 40th AIAA Aerospace Sciences Meeting & Exhibit, AIAA 2002-0662, Jan. 2002.

22. White, F.M., *Viscous Fluid Flow*, 2nd ed., McGraw-Hill, New York, 1991, pp. 10-11.

23. Van Dyke, M., *An Album of Fluid Motion*, Parabolic Press, Stanford, California, 1982, pp. 164.

Appendices

Appendix A – MATLAB Code

```
% ------------------ Input Parameters ------------------------------------

fs = 40000;                         % Sampling frequency (40 000 Hz)
T = 1/fs;                           % Time between samples
L = 40000;                          % Length of signal (40 000 data points)
t = (0:L-1)*T;                      % Time vector

% ------------------- Reading Raw Data File ------------------------------

x = data(:,3);                      % Reads 3rd Column of raw data file
                                    % which represents pressure in Pascals

% ------------------- FFT Algorithm --------------------------------------

% written in accordance with Mathworks website instructions available at:
% http://www.mathworks.com/access/helpdesk/help/techdoc/ref/fft.html

%nfft = 2^nextpow2(L);               % Next power of 2 from length of y
%nfft = 4000000;
nfft = 256*4;
Y = fft(x,nfft)/L;                  % Matlab FFT command
f = fs/2*linspace(0,1,nfft/2+1);    % Frequency vector used for later plots
Pressure_FFT_Data = 2*abs(Y(1:nfft/2+1));



% 1.--------------- FFT Plot of Acoustic Sound Level in Frequency Domain -

SPL = 20*log10(Pressure_FFT_Data/(2*10^-5)); % decibel (dB) Scaling
subplot(2,1,1)
plot(f,SPL)
title('  FFT Plot of Acoustic Spectrum in Frequency
Domain','fontsize',16,'fontweight','b')
xlabel('Frequency (Hz)','fontsize',16,'fontweight','b')
ylabel('Amplitude (dB SPL)','fontsize',16,'fontweight','b')
xmin = 0;                           % Min frequency shown on FFT plot
xmax = 20000;                       % Max frequency shown on FFT plot
ymin = 60;                          % Min amplitude shown on FFT plot
ymax = 180;                         % Max amplitude shown on FFT plot
axis([xmin xmax ymin ymax]);
set(gca,'FontSize',20)

% 2.- PSD Plot (output Pa^2/Hz) in Frequency Domain using Matlab Function -

% written in accordance with Mathworks website instructions available at:
%
http://www.mathworks.com/access/helpdesk/help/toolbox/signal/periodogram.shtm
l

% LOG-LOG AXIS

window = [];
[Pxx,f] = periodogram(x,window,nfft,fs);
```

```
subplot(2,1,2)
loglog(f,Pxx);    % creates a plot using logarithmic scale for the y-axis
title('  PSD Plot versus Frequency (log-log
axis)','fontsize',16,'fontweight','b');
xlabel('Frequency (Hz)','fontsize',16,'fontweight','b');
ylabel('Power (Pa^2/Hz)','fontsize',16,'fontweight','b');
xmin = 10^2;       % Min frequency shown on PSD plot
xmax = 2*10^4;     % Max frequency shown on PSD plot
ymin = 10^0;       % Min Pa^2/Hz shown on PSD plot
ymax = 10^8;       % Max Pa^2/Hz shown on PSD plot
axis([xmin xmax ymin ymax]);
set(gca,'FontSize',20)
```

Appendix B – Drawings

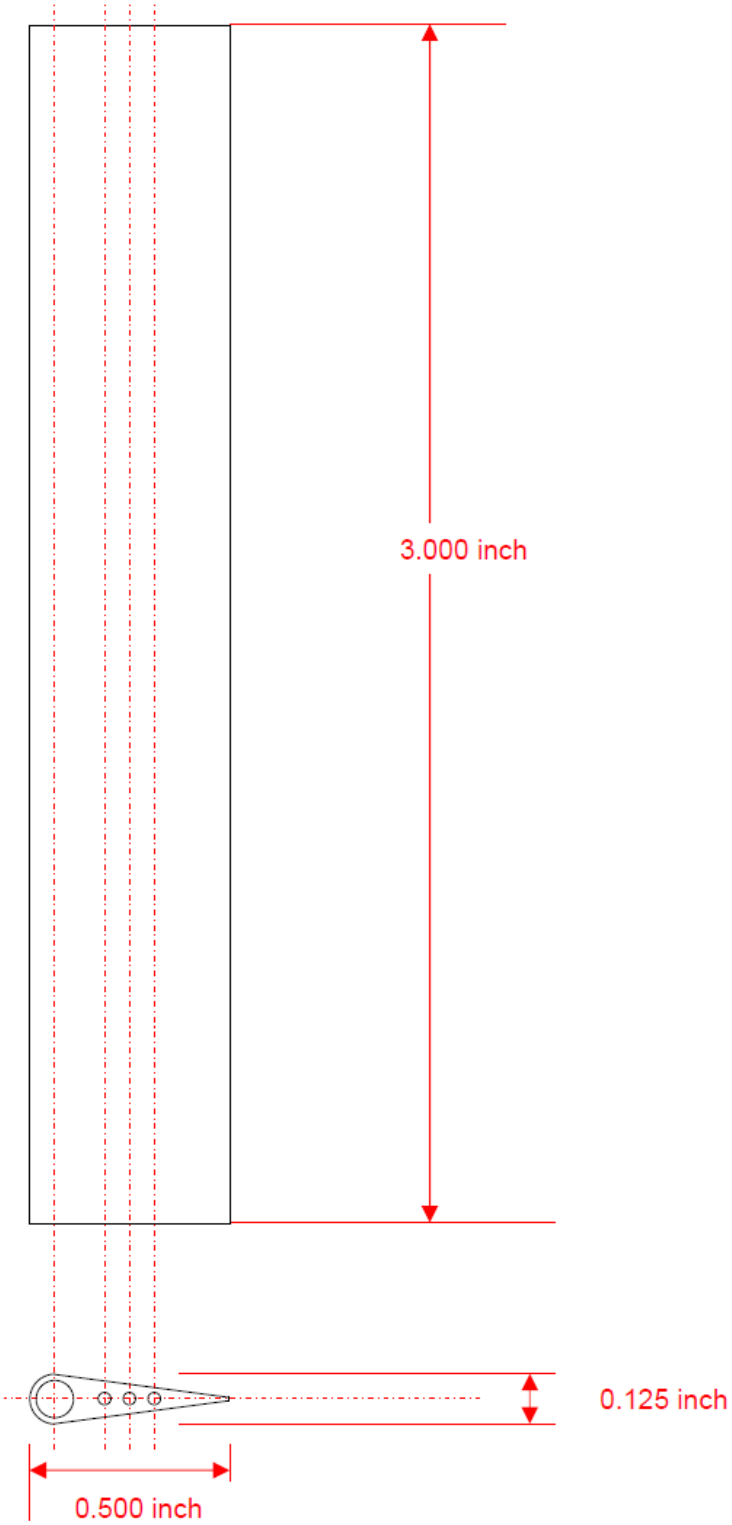

Figure A.1. Airfoil Drawing 1

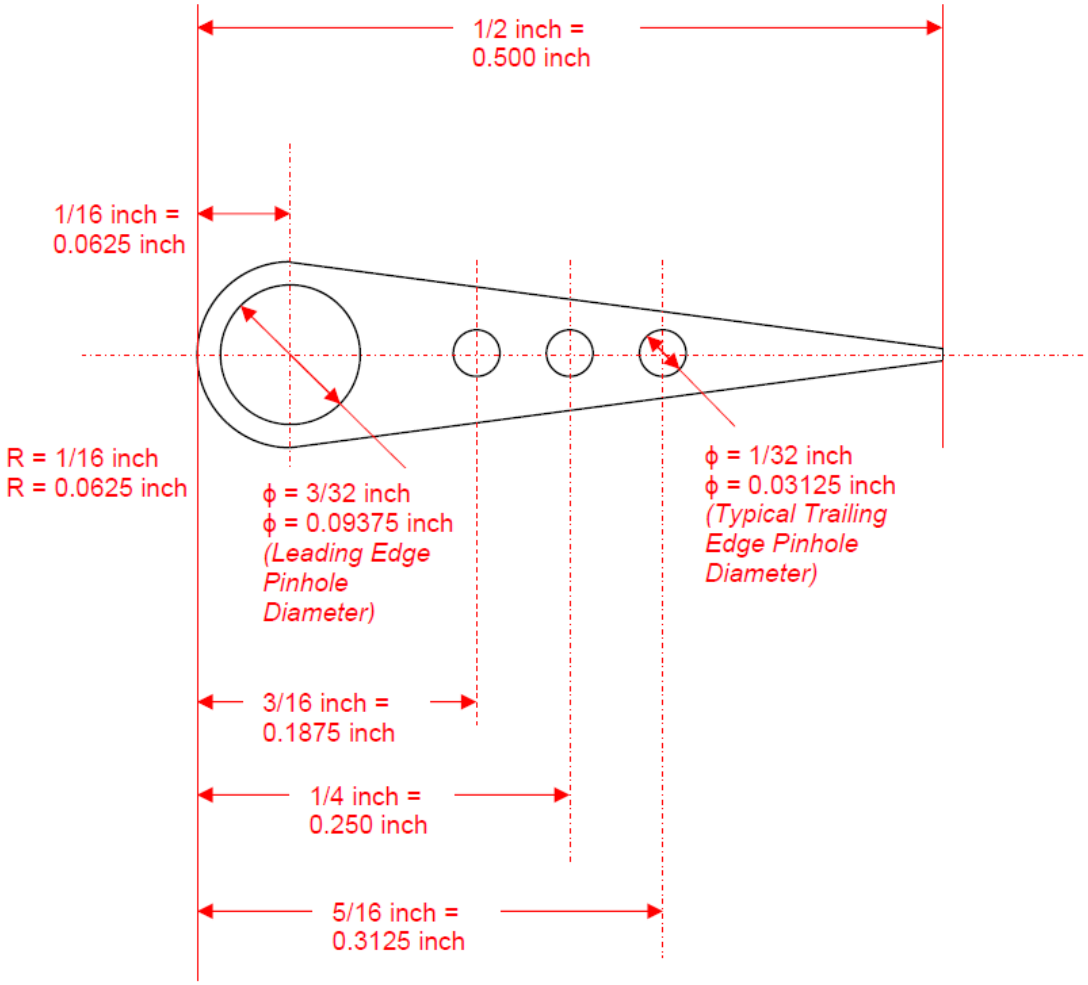

Figure A.2. Airfoil Drawing 2 (Pin Hole Locations)

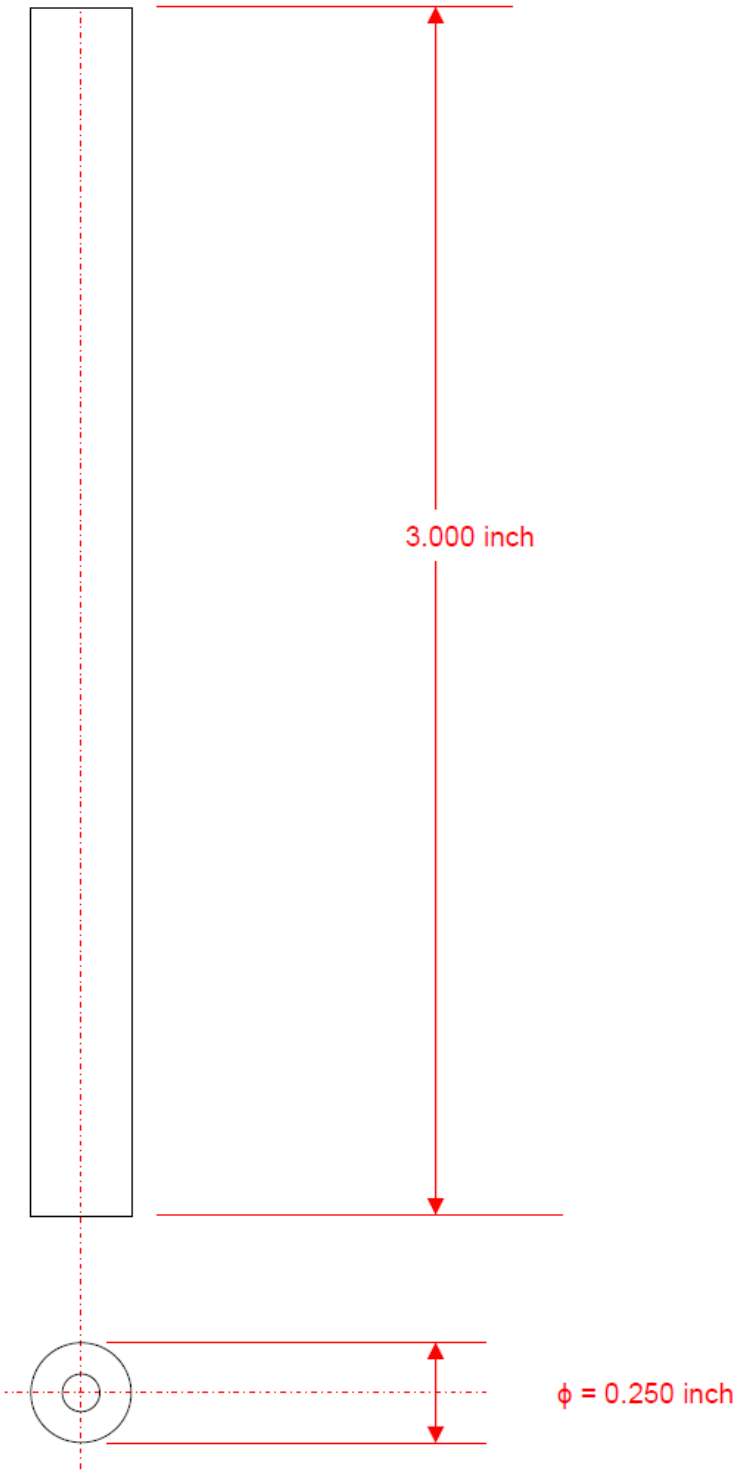

Figure A.3. Quarter Inch Rod Drawing 1

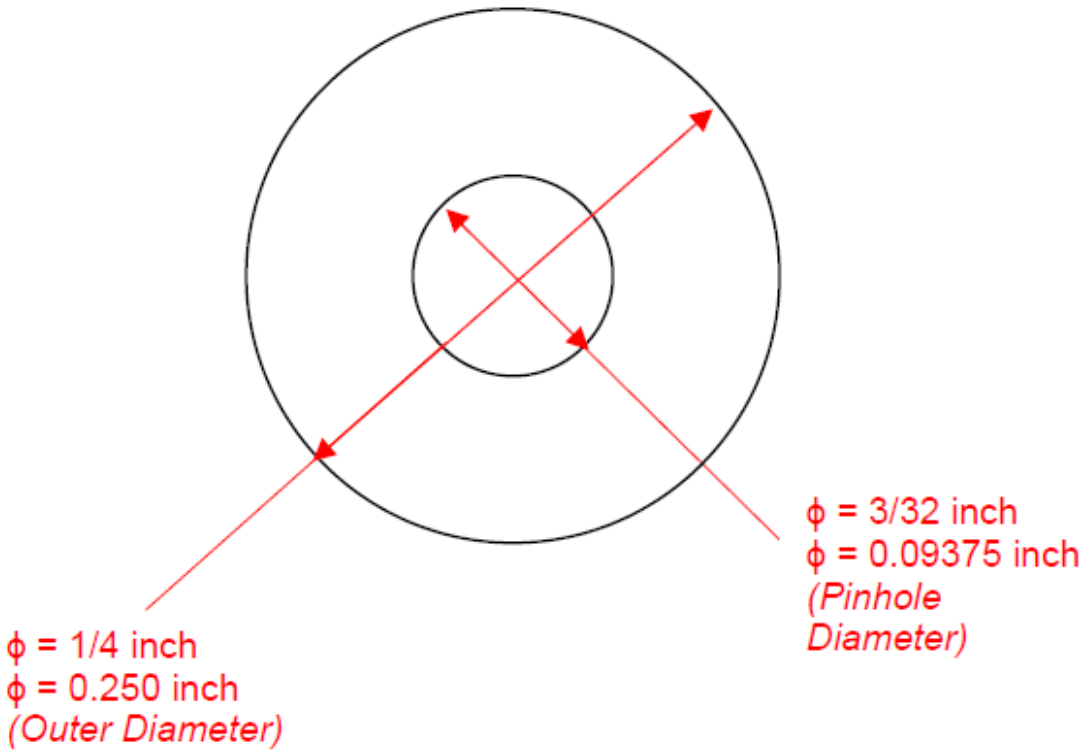

Figure A.4. Quarter Inch Rod Drawing 2

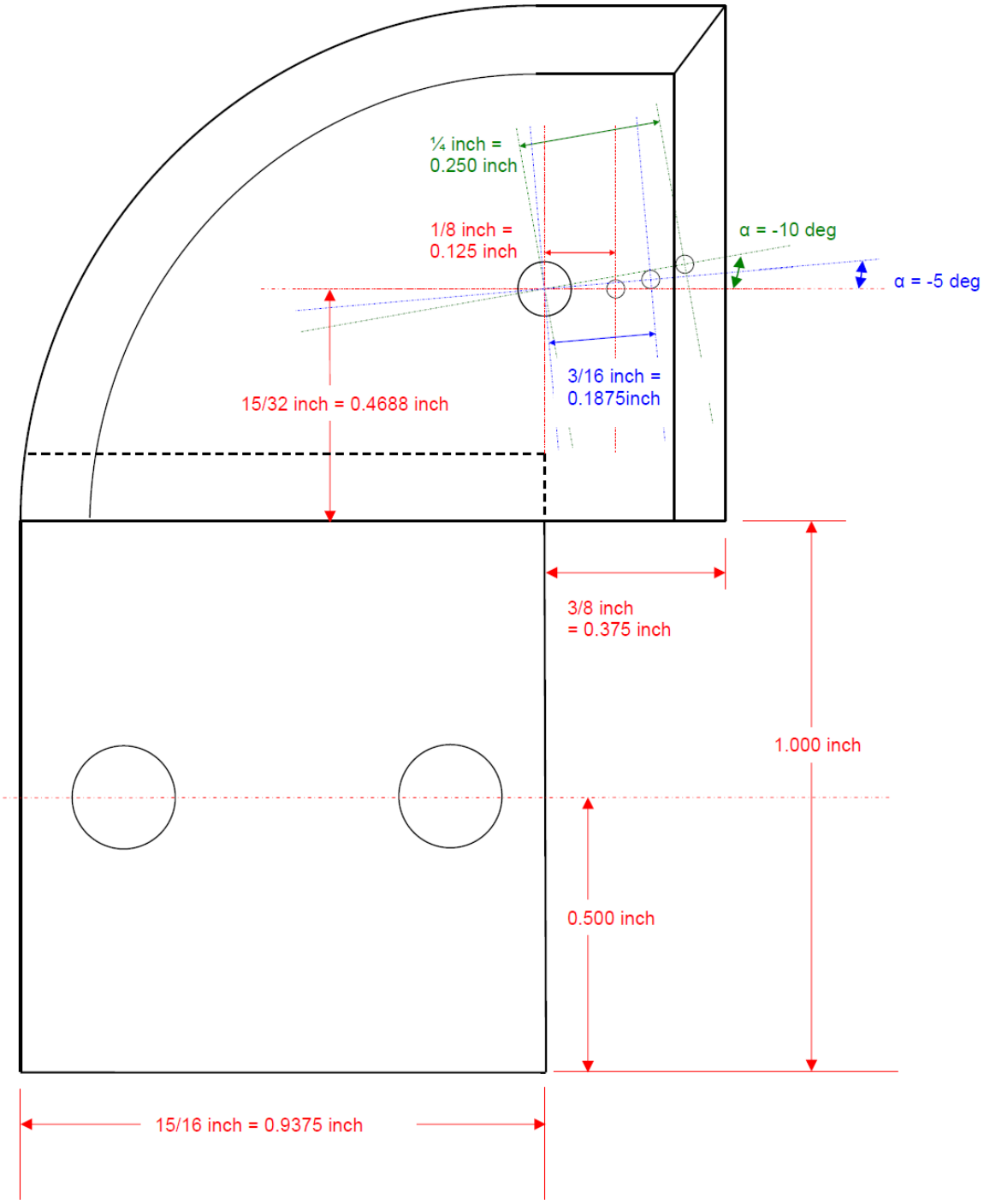

Figure A.5. Side Plate Drawing 1

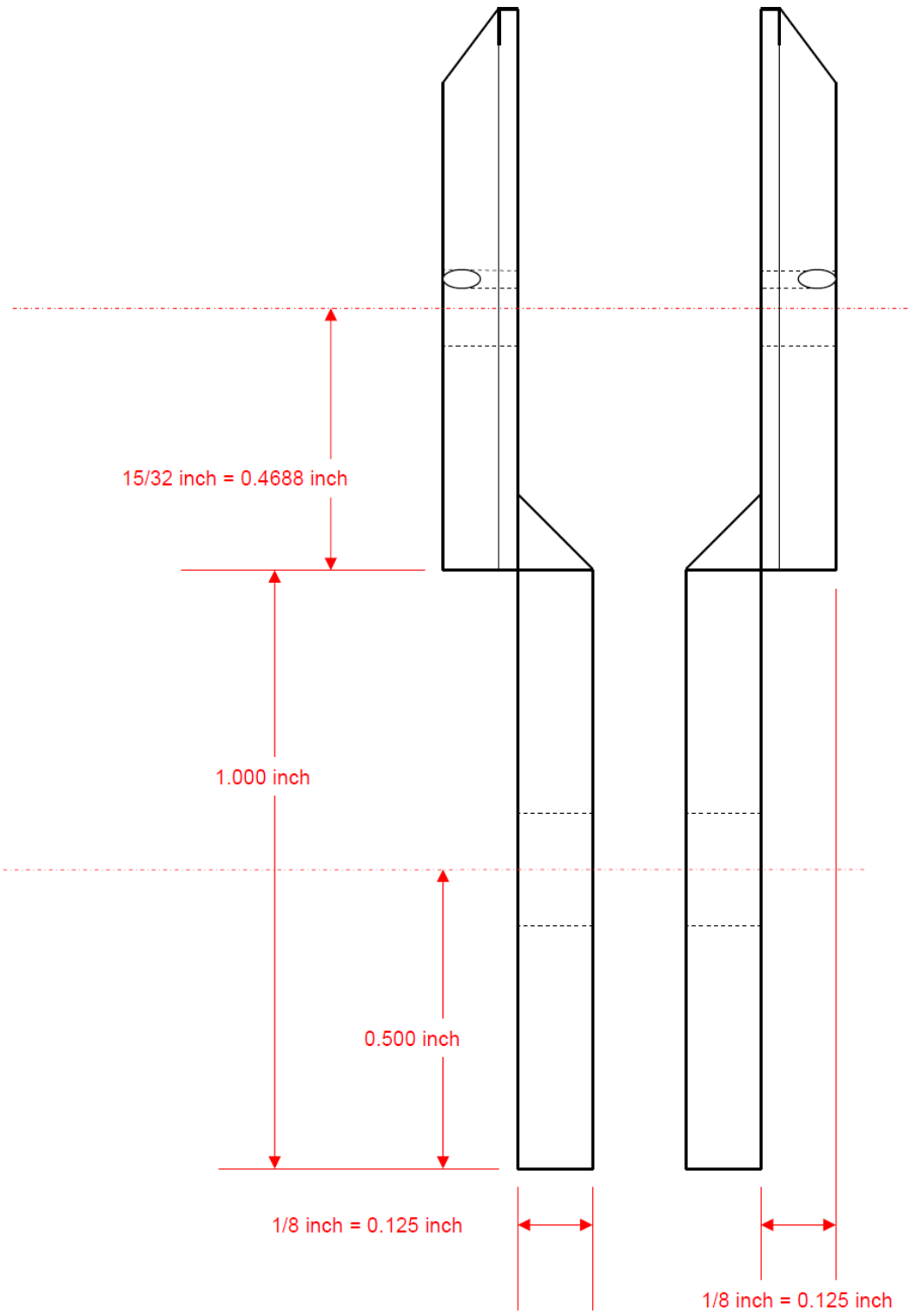

Figure A.6. Side Plate Drawing 2

Vita

William Leland “Lee” Lionel Fowler was born in St. Albert, Alberta, Canada on April 15th, 1978. In September 1997, Lee enrolled to study engineering at the University of Alberta and graduated with a Bachelor of Science Degree in Mechanical Engineering in June 2001.

Following various positions of temporary employment, Lee joined the Canadian Forces on January 17th, 2002 under the Direct Entry Officer Enrolment Plan for the Aerospace Engineering Officer (AERE) occupation. Following the completion of phase training at a variety of locations across Canada, he was posted to Cold Lake, Alberta on May 20th, 2004. From May 2004 to July 2006, Lee held the position of Operations Maintenance Officer for the Aerospace Engineering Test Establishment (AETE). His role included management of a maintenance organization supporting operations with the CF-18 Hornet, the CH146 Griffon (based on the Bell 412 helicopter), the CT114 Tutor and the CT133 T-Bird (the Silver Star). From July 2006 to July 2008, Lee was an Engineering Project Officer within the Fighter Operational Test and Evaluation Flight (FOTEF) of 410 Tactical Fighter Operational Training Squadron. Within this position, Lee was the project engineer for the operational evaluation of the second phase of the CF-18 modernization program known as Engineering Change Proposal (ECP) R2.

In August 2008, Lee was enrolled at the University of Tennessee Space Institute after selection by the Canadian Forces for a sponsored postgraduate training program. During this time, he pursued the requirements for a Master of Science Degree in Aerospace Engineering. Upon completion of his studies, Lee was posted to Ottawa, Ontario, Canada to work within the Flight Sciences section of the Directorate of Technical Airworthiness and Engineering Support (DTAES).